

Electronic Thesis and Dissertation Repository

7-9-2012 12:00 AM

X-ray Absorption Fine Structure and X-ray Excited Optical Luminescence Studies of One-dimensional Nanomaterials

Lijia Liu, *The University of Western Ontario*

Supervisor: Tsun-Kong Sham, *The University of Western Ontario*

A thesis submitted in partial fulfillment of the requirements for the Doctor of Philosophy degree in Chemistry

© Lijia Liu 2012

Follow this and additional works at: <https://ir.lib.uwo.ca/etd>

 Part of the [Physical Chemistry Commons](#)

Recommended Citation

Liu, Lijia, "X-ray Absorption Fine Structure and X-ray Excited Optical Luminescence Studies of One-dimensional Nanomaterials" (2012). *Electronic Thesis and Dissertation Repository*. 618.
<https://ir.lib.uwo.ca/etd/618>

This Dissertation/Thesis is brought to you for free and open access by Scholarship@Western. It has been accepted for inclusion in Electronic Thesis and Dissertation Repository by an authorized administrator of Scholarship@Western. For more information, please contact wlsadmin@uwo.ca.

X-RAY ABSORPTION FINE STRUCTURE AND X-RAY EXCITED OPTICAL
LUMINESCENCE STUDIES OF ONE-DIMENSIONAL NANOMATERIALS

(Spine title: XAFS and XEOL Studies of 1D Nanomaterials)

(Thesis format: Integrated Article)

by

Lijia Liu

Graduate Program in Chemistry

A thesis submitted in partial fulfillment
of the requirements for the degree of
Doctor of Philosophy

The School of Graduate and Postdoctoral Studies
The University of Western Ontario
London, Ontario, Canada

© Lijia Liu 2012

THE UNIVERSITY OF WESTERN ONTARIO
School of Graduate and Postdoctoral Studies

CERTIFICATE OF EXAMINATION

Supervisor

Examiners

Dr. Tsun-Kong Sham

Dr. Ron Martin

Supervisory Committee

Dr. Lars Konermann

Dr. Giovanni Fanchini

Dr. Jinghua Guo

The thesis by

Lijia Liu

entitled:

**X-ray Absorption Fine Structure and X-ray Excited Optical
Luminescence Studies of One-dimensional Nanomaterials**

is accepted in partial fulfillment of the
requirements for the degree of
Doctor of Philosophy

Date

Chair of the Thesis Examination Board

Abstract

One dimensional nanomaterials have attracted extensive attention in recent years due to their superior electrical, optical, mechanical and chemical properties compared to their bulk counterparts. In this thesis, electronic structure and optical properties of three types of nanomaterials are investigated using synchrotron based X-ray absorption spectroscopy: X-ray absorption fine structure (XAFS) and X-ray excited optical luminescence (XEOL).

Si nanowire arrays are synthesized using electroless chemical etching, and coated with platinum and gold nanoparticles. The interaction between metal nanoparticles and the nanowire substrate is investigated using X-ray absorption near-edge structure (XANES). The luminescence properties of thermally oxidized Si nanostructures, such as Si nanowires, porous Si nanowires, and porous Si are comparatively studied. Using XEOL in combination with XANES, luminescence from defect centers in SiO₂ and from Si/SiO₂ interface can be distinguished. Electronic structure and luminescence of silicon carbide micro- and nanostructures of different crystal structures (polytypes) are investigated. Although hexagonal and cubic SiC have similar electronic structures locally, they exhibit different luminescence properties. It is found that all SiC samples have a same defect emission regardless of crystal size and structure. Additional luminescence bands are observed when oxide is present. Cubic SiC has two luminescence bands, originated from SiC and surface native SiO₂, respectively. SiC nanowires also exhibit quantum confined band gap luminescence. As for boron nitride nanotubes, the presence of oxygen atoms in BN lattice alters the luminescence significantly by introducing a new defect center. The presence of oxygen impurities results in an intense signal revealed by XANES which is associated with

B-O bonding, but no noticeable difference is seen in XANES at N site.

Keywords

X-ray absorption near-edge structure, X-ray excited optical luminescence, silicon nanowires, thermal oxidation, porous silicon, platinum-gold nanoparticle alloys, silicon carbide nanowires, silicon carbide polytypes, boron nitride nanotubes, oxygen impurities, metal-assisted chemical etching

Co-Authorship Statement

This thesis contains materials from previously published manuscripts. Dr. Tsun-Kong Sham is co-authored on all published papers and he played a major role in editing and revising the content presented in this thesis.

In Chapter 5, silicon carbide nanowires were prepared by L. Zhang and Dr. Y. Zhang from Shanghai Jiao Tong University. Preliminary characterizations of the SiC nanowires (SEM, TEM and XRD) were done by them as well. Electronic structure calculation using WIEN2k program was performed by Dr. Y. M. Yiu. Boron nitride nanotubes samples were synthesized by Dr. W. Han from Brookhaven National Laboratory, together with Dr. C. Zhi and Dr. Y. Bando from National Institute for Materials Science (NIMS), Japan.

Technical support with synchrotron spectroscopy measurements at Canadian Light Source (CLS) were provided by the following people: Yongfeng Hu (now at SXRMB beamline, CLS), Chris Ryan, and Lucia Zuin for measurements performed at the VLS-PGM beamline; Robert Blyth, Tom Regier and David Chevier for experiments performed at the SGM beamline. Technical support at Advanced Photon Source (APS) PNC-XSD beamline 20-BM was provided by Robert A. Gordon.

Scanning electron microscopy graphs presented in Chapter 3 and Appendix A were taken with assistance from Todd Simpson at Nanofabrication Laboratory, University of Western Ontario. Transmission electron microscopy graphs presented in Chapter 3 and Appendix A were taken with assistance from Richard Gardiner at Biotron, University of Western Ontario. X-ray photoelectron spectroscopy measurements in Chapter 3 were performed by Mark Biesinger.

To my family

Acknowledgments

First of all, I would like to thank my supervisor, Dr. Tsun-Kong Sham, for his guidance and support during the five years of my graduate study. It has been a precious and valuable time working with a supervisor like you. Your insightful ideas, kindness and enthusiasm about science always encourage me. I am thankful for the opportunities you provided to meet people doing synchrotron research from all around the world, and to learn and gain experience on various synchrotron techniques. I really appreciate your support.

Next I would like to thank my present group members: Dr. Yun-Mui Yiu, Dr. Zhiqiang Wang, Mr. Matthew Ward, Ms. Olga Lobacheva, Mr. Dongniu Wang, Mr. Xiaoxuan Guo, Mr. Fuyang Zhao and Mr. Ankang Zhao for their helpful discussion and constructive feedback on the ongoing research. I would also like to thank the former group members: Dr. J. Y. Peter Ko, Dr. Michael Murphy, Dr. Jigang Zhou and Mr. Nick Grawburg. When I first started my graduate study, synchrotron spectroscopy was a new concept to me. Your kind help on how to do measurements at the beamline and the data interpretation is priceless to me.

Technical support provided by the following people is greatly appreciated: beamline scientists Dr. Yongfeng Hu, Dr. Lucia Zuin, Mr. Chris Ryan, Dr. Robert Blyth, Mr. Tom Regier and Mr. David Chevier from Canadian Light Source; Dr. Robert A. Gordon from Advanced Photon Source; Mr. Todd Simpson from Nanofabrication Laboratory; Dr. Richard Gardiner from Biotron; Dr. Mark Biesinger from Surface Science Western.

I also want to thank our collaborators, Dr. Yafei Zhang's group in Shanghai Jiao-Tong University and Dr. Weiqiang Han from Brookhaven National Laboratory for their support on sample preparations.

The five-year graduate study in Western is the first time I have spent in a foreign country. I would like to thank the support and encouragement from my parents in China. I would also like to give my thanks to Xiangrong Zhang and her family, Zhaohui Dong, Jing Chao, and John McLeod. I am lucky to have you as my friends during these years, and my life would not be the same without you.

Research at University of Western Ontario is funded by the Natural Science and Engineering Research Council of Canada (NSERC), Canadian Research Chair (CRC) for T. K. Sham, Canada Foundation for Innovation (CFI) and the Ontario Innovation Trust (OIT). I acknowledge the support from Ontario Graduate Scholarship. Surface Science Western (SSW), Nanofabrication Laboratory (Nanofab) and Biotron are funded by UWO. Canadian Light Source (CLS) is supported by NSERC, National Research Council (NRC), Canadian Institutes of Health Research (CIHR) and University of Saskatchewan. PNC/XSD facilities at the Advanced Photon Source (APS) are supported by the US Department of Energy-Basic Energy Sciences, a Major Resources Support grant from NSERC, the University of Washington, the Canadian Light Source and the Advanced Photon Source.

Table of Contents

CERTIFICATE OF EXAMINATION	ii
Abstract	iii
Co-Authorship Statement.....	v
Acknowledgments.....	vii
Table of Contents	ix
List of Tables	xiii
List of Figures	xiv
List of Abbreviations	xxi
Chapter 1	1
1 Introduction	1
1.1 Nanostructures.....	1
1.1.1 General Background	1
1.1.2 Nanomaterial Synthesis	4
1.2 X-ray Absorption and Related Spectroscopy.....	6
1.2.1 X-ray Absorption Fine Structure	6
1.2.2 De-excitation Processes Following the X-ray Absorption.....	13
1.2.3 Recombination Process: X-ray Excited Optical Luminescence	14
1.3 Synchrotron Radiation Overview.....	16
1.4 Outline of Thesis	23
1.5 References	24
Chapter 2.....	28
2 Synchrotron Instrumentation and XAFS Calculation	28
2.1 Synchrotron Facilities	28

2.1.1	Canadian Light Source (CLS).....	28
2.1.2	Advanced Photon Source (APS).....	29
2.2	Beamlines.....	30
2.2.1	Variable Line Spacing Plane Grating Monochromator (VLS-PGM) Beamline–CLS 11ID-2.....	30
2.2.2	High Resolution Spherical Grating Monochromator (SGM) Beamline–CLS 11ID-1.....	31
2.2.3	X-ray Science Division Partnered with the Pacific Northwest Consortium (PNC-XSD) Sector 20.....	32
2.3	Detection Modes	33
2.4	XAFS Calculation	37
2.5	References	38
Chapter 3	41
3	XANES and XPS Studies of Metal Nanoparticles Deposited SiNW	41
3.1	Introduction.....	41
3.2	Experimental	43
3.2.1	Synthesis	43
3.2.2	Characterization	44
3.3	Results and Discussion.....	46
3.3.1	XANES of Metal Deposited SiNW	46
3.3.2	XPS of Metal Deposited SiNW	53
3.4	Conclusion	57
3.5	References	57
Chapter 4	60
4	The Effect of Thermal Oxidation On the Luminescence Properties of Nanostructured Silicon	60
4.1	Introduction.....	60

4.2 Experimental	62
4.3 Results and Discussion.....	63
4.3.1 XANES of Nanostructured Si Before and After Oxidation.....	63
4.3.2 Luminescence From Oxidized SiNW and PS.....	65
4.4 Conclusion	80
4.5 References	80
Chapter 5.....	84
5 Electronic Structure and Optical Property Studies of SiC Nanostructures and Polytypes	84
5.1 Introduction	84
5.2 Experimental and Calculation Procedure.....	86
5.3 Results and Discussions	89
5.3.1 Electronic Structures and SiC.....	89
5.3.2 Optical Properties of SiC	98
5.4 Conclusion	108
5.5 References	109
Chapter 6.....	113
6 XANES and XEOL Studies of Boron Nitride Nanotubes	113
6.1 Introduction	113
6.2 Experimental	115
6.3 Results and Discussion	116
6.3.1 Electronic Structure of BN.....	116
6.3.2 Luminescence From BN	122
6.4 Conclusion	135
6.5 References.....	136
Chapter 7.....	140

7 Summary and Future Work.....	140
7.1 Conclusions.....	140
7.2 Future Work.....	142
7.3 References.....	144
Appendix A.....	145
Appendix A Silver-assisted Electroless Chemical Etching of SiNW: Synthesis and Etching Mechanism.....	145
A.1 Introduction.....	145
A.2 Experimental.....	147
A.3 Results and Discussion	148
A.3.1 Effecting Factor 1: Etchant Concentration	149
A.3.2 Effecting Factor 2: Etching Duration.....	153
A.3.3 Effecting Factor 3: Doping Level	154
A.3.4 Etching Mechanism	155
A.4 Conclusion.....	159
A.5 References.....	160
Appendix B Copyright release from John Wiley and Sons	162
Appendix C Copyright release from ACS Publications	168
Appendix D Copyright release from ACS publications	169
Curriculum Vitae	170

List of Tables

Table 4-1: Denotation of SiNW and porous Si.....	62
Table A-1: Physical parameters of Si wafers used in the experiment.	148

List of Figures

Figure 1-1 Schematic illustrations of density of states comparison (a) among bulk, nano and atom, and (b) among bulk and nanomaterials with specific dimensionality. CB: conduction band, VB: valence band.	2
Figure 1-2 Log-log plot of the mass absorption coefficient of platinum as a function of X-ray photon energy.....	7
Figure 1-3 Schematic illustration of the outgoing photoelectron wave produced by (a) a free atom and (b) a diatomic system upon X-ray absorption and the corresponding XANES spectrum.[29]	9
Figure 1-4 Schematic view of multiple scattering processes of several scattering pathways, where $n=2, 3$, and 4 in χ_n indicates the number of atoms involved in a scattering pathway. .	11
Figure 1-5 Schematic diagram of the de-excitation processes upon core electron excitation. (a) photo-absorption resulting a photoelectron and a core hole, (b) Auger process, (c) X-ray fluorescence. Solid circles: electrons, open circles: holes.	14
Figure 1-6 Schematic diagram of the electron-hole pair generation and recombination. (a) core electron excitation, (b) electron and hole thermalization, (c) examples of radiative recombination via (i) direct recombination, (ii) phonon-assisted indirect recombination, (iii) presence of traps	15
Figure 1-7 Schematic layout of a synchrotron radiation facility.	18

Figure 1-8 (a) schematic layout and (b) comparison of the spectral distribution of bending magnet, wiggler and undulator. γ is the opening angle, and N is the number of magnets.	20
Figure 1-9 Schematic illustration of the plane grating monochromator at (a) zero order position, and (b) rotated position.	20
Figure 1-10 (a) Bragg diffraction. (b) Schematic layout of a double-crystal monochromator	22
Figure 2-1 Schematic layout of the CLS beamlines as of Feb, 28, 2012[2]	28
Figure 2-2 Schematic layout of the APS beamlines[4].....	29
Figure 2-3 Layout of VLS-PGM beamline.[5] FM, fixed mask; M1, plane mirror; M2, toroidal mirror; M3, spherical mirror; M4, plane mirror; M5 and M6, toroidal refocusing mirrors.....	31
Figure 2-4 Layout of the SGM beamline.[7]	32
Figure 2-5 Schematic layout of the 20-BM beamline.[8]	33
Figure 2-6 Illustration of XAFS detection modes: (a) transmission, (b) fluorescence and electron yield, (c) optical yield.	34
Figure 2-7 Universal curve for electron inelastic mean free path as a function of the kinetic energy.....	35
Figure 3-1 Selected SEM and TEM images of Pt and Au deposited SiNW. (a) SEM of Pt-SiNW, (b) SEM of Au-SiNW, (c) TEM of Pt-SiNW	45

Figure 3-2 XANES of Pt-SiNW and Au-SiNW at (a) the Pt L ₃ -edge, (b) the Pt L ₂ -edge, and (c) the Au L ₃ -edge. The spectra are normalized to unit edge jump. The insets show the magnified white line region.	47
Figure 3-3 XANES of Pt-Au-SiNW obtained at the Pt L ₃ - and L ₂ -edge in comparison with Pt foil. The difference curves are done by subtracting XANES of L ₂ from L ₃ for Pt foil and Pt-Au-SiNW, respectively.	50
Figure 3-4 Au L ₃ -edge XANES of Pt-Au-SiNW in comparison with Au foil.	51
Figure 3-5 Si K-edge XANES of SiNW before and after metal deposition. (a) TEY, (b) FY.	52
Figure 3-6 XPS spectra of Pt and Au deposited SiNW. (a) Pt 4f XPS of Pt-SiNW, Pt-Au-SiNW and bulk Pt, (b) peak fittings of Pt-Au-SiNW at Pt 4f, (c) Au 4f XPS of Au-SiNW, Pt-Au-SiNW and bulk Au, (d) peak fittings of Pt-Au-SiNW at Au 4f.....	54
Figure 3-7 Si 2p XPS spectra of Pt-SiNW, Au-SiNW and Pt-Au-SiNW.....	56
Figure 4-1 Si K-edge XANES of SiNW and PS samples before and after oxidation in (a) TEY and (b) FY.	64
Figure 4-2 XEOL of SiNW and PS with excitation energy at 1900 eV.	65
Figure 4-3 PLY of SiNW-p-800 across the Si L _{3,2} -edge. (a) 2D XANES-XEOL plot and individual XEOL obtained under 120 eV excitation. (b) PLY-XANES at zero order and selected wavelengths (vertical cuts from Fig. 4-3(a)) in comparison with TEY and FY as well as the TEY of as-prepared SiNW-p.	68

Figure 4-4 (a) Si K-edge PLY-XANES of SiNW-p-800, (b) selected XEOL of SiNW-p-800 with excitation energies below to above the Si K-edge.....	71
Figure 4-5 (a) O K-edge PLY-XANES of SiNW-p-800, (b) selected XEOL of SiNW-p-800 with excitation energies below to above O K-edge.	76
Figure 4-6 Si K-edge PLY-XANES of (a) PS-800 and (b) SiO ₂ nw, O K-edge PLY-XANES of (c) PS-800 and (d) SiO ₂ nw.	77
Figure 5-1 Morphology of 3C-cs in (a) SEM and (b) TEM, (c) XRD pattern of 3C-cs.....	87
Figure 5-2 Sketch of SiC crystal structures drawn using the VESTA program[24] (a) 6H-SiC and (b) 3C-SiC. Si atoms in black, C atoms in grey	88
Figure 5-3 Si K-edge XANES of 6H-mc, 6H-pd and 3C-pd. Solid lines: TEY, open circles: FY.	91
Figure 5-4 Calculated Si K-edge XANES and DOS plots in comparison with experimental XANES. (a) 6H-SiC, 6H-mc TEY is used as experimental spectrum; (b) 3C-SiC, 3C-pd TEY is used as experimental spectrum.....	92
Figure 5-5 (a) Si K-edge XANES of 3C-cs and 3C-nw in TEY and FY. The TEY spectra of 3C-pd and SiO ₂ are shown for comparison. (b) Linear combination fit results of 3C-cs TEY.	93
Figure 5-6 C K-edge XANES of 6H-mc, 6H-pd and 3C-pd. Solid lines: TEY, open circles: FY	95

Figure 5-7 Partial DOS plots of C site and calculated C K-edge XANES in comparison with experimental XANES. (a) 6H-SiC, (b) 3C-SiC.....	96
Figure 5-8 C K-edge XANES of 3C-cs and 3C-nw in TEY (solid lines) and FY (open circles). The 3C-pd FY spectrum is shown as reference.	98
Figure 5-9 Normalized XEOL of 6H-mc and 6H-pd with excitation photon energy above the Si K- and C K-edge, respectively.	100
Figure 5-10 Si K-edge PLY and FY of 6H-mc and 6H-pd.....	101
Figure 5-11 Normalized XEOL of 3C-pd, 3C-cs and 3C-nw with Gaussian fittings under excitation energy at (a) 1860 eV and (b) 290 eV.....	103
Figure 5-12 Wavelength selected PLY of 3C-pd, in which the intensity of fitted emission peaks (by peak areas) is plotted against the excitation energy, and the TEY of 3C-pd is shown as reference. XEOL with fitted peaks is shown in inset.....	105
Figure 5-13 Region selected PLY of (a) 3C-cs and (b) 3C-nw. The insets show the XEOL spectra with fitted peaks.....	106
Figure 6-1 TEM image of an individual nat-BNNT.....	116
Figure 6-2 XANES of hex-BN, nat-BNNT, 10-BNNT and B ₂ O ₃ . Solid lines: TEY, open circles: FY. The spectra are normalized to unit edge jump, and the intensity of B ₂ O ₃ TEY is decreased by half to fit in the scale.....	117
Figure 6-3 Two structure models of B ₂ O ₃ . Oxygen atoms are in blue, and boron atoms are in red.	118

Figure 6-4 XANES of hex-BN, nat-BNNT and 10-BNNT at the N K-edge. Solid lines: TEY, open circles: FY.	120
Figure 6-5 (a) FY-XANES of hex-BN with arrows indicating the energies at which XEOL spectra in (b) are obtained. (b) XEOL spectra of hex-BN at selected energies from below to above the B K-edge after normalization to I_0 . (c) XEOL spectra of hex-BN after normalization to the most intense emission peak and being shifted vertically for clarity.	123
Figure 6-6 PLY (zero order)-XANES of hex-BN at (a) the B K-edge and (b) the N K-edge.	125
Figure 6-7 (a) XEOL spectra of nat-BNNT with selected excitation energies as indicated by arrows in (b). (b) PLY-XANES of nat-BNNT at the B K-edge in comparison with TEY and FY.	126
Figure 6-8 XEOL after intensity normalized to the 3.89 eV emission and shifted vertically for clarity.	127
Figure 6-9 PLY-XANES of nat-BNNT at the (a) N K-edge and (b) O K-edge. The O K-edge TEY of B_2O_3 is shown as a reference.	128
Figure 6-10 (a) XEOL of 10-BNNT with selected excitation energies across the B K-edge. (b) Enlarged view of XEOL at the 2.0 eV-5.0 eV region after normalization to the 3.76 eV peak. (c) B K-edge PLY of 10-BNNT in comparison with TEY and FY-XANES.	131
Figure 6-11 PLY-XANES of 10-BNNT at (a) the N K-edge and (b) the O K-edge.	133
Figure 6-12 XEOL of hex-BN, nat-BNNT and 10-BNNT at excitation energy of 210 eV.	134

Figure A-1 Morphology of SiNW. Top row: n-type SiNW, bottom row: p-type SiNW. (a) and (d): SEM images in top view, (b) and (e): SEM images in side view, (c) and (f): TEM images of a single wire. 149

Figure A-2 SEM images of SiNWs made from varied AgNO_3 concentrations. (a) and (b) 0.0015 M, (c) and (d) 0.005 M, (e) and (f) 0.01 M, (g) and (h) 0.02 M. 151

Figure A-3 SEM images of SiNW made from varied H_2O_2 concentrations. (a) and (b) 0.3 M, (c) and (d) 0.4 M, (e) and (f) 0.5 M. 152

Figure A-4 The length of SiNW as a function of (a) AgNO_3 concentration and (b) H_2O_2 concentration. 153

Figure A-5 SEM images in top view of SiNW etched for (a) 1 min, (b) 5 min and (c) 120 min; and (d) plot of the length of SiNW as a function of etching time. 154

Figure A-6 Morphology of SiNW by etching of heavily doped Si wafer. (a) SEM image in top view, (b) SEM image in side view, and (c) TEM image of single wires. 155

Figure A-7 Schematic diagram of the SiNW formation. (a) Ag deposition, (b) electroless Ag-assisted etching 155

Figure A-8 SEM images of Si wafer after Ag deposition (a) Ag nanoparticles, (b) Ag dendrite 157

List of Abbreviations

0D	zero dimensional
1D	one dimensional
2D	two dimensional
ACF	activated carbon fiber
APS	Advanced Photon Source
APW	augmented plain waves
AuNP	gold nanoparticles
BE	binding energy
BM	bending magnet
BNNT	Boron nitride nanotubes
CCD	charge-coupled device
CL	cathodoluminescence
CLS	Canadian Light Source
CNT	carbon nanotubes
CVD	chemical vapor deposition
DCM	double-crystal monochromator
DFT	density functional theory
DOS	density of states
EXAFS	Extended X-ray absorption fine structure

FY	X-ray fluorescence yield
GGA	generalize gradient approximation
hex-BN	hexagonal boron nitride
IMFP	inelastic mean free path
IPFY	inverted partial fluorescence yield
IR	infrared
LINAC	linear accelerator
NBOHC	non-bridging oxygen hole center
ODC	oxygen deficient center
PL	photoluminescence
PLY	photoluminescence yield
PNC/XSD	X-ray Science Division partnered with the Pacific Northwest Consortium
PS	porous silicon
PtNP	platinum nanoparticles
PVD	physical vapor deposition
RF	radio frequency
SEM	scanning electron microscopy
SGM	spherical grating monochromator
SiNW	silicon nanowires

SSW	Surface Science Western
STXM	scanning transmission X-ray microscopy
TEM	transmission electron microscopy
TEY	total electron yield
UV	ultraviolet
UWO	University of Western Ontario
VLS- PGM	variable line spacing plane grating monochromator
XAFS	X-ray absorption fine structure
XANES	X-ray absorption near-edge structure
XEOL	X-ray excited optical luminescence
XPS	X-ray photoelectron spectroscopy
XRD	X-ray diffraction

Chapter 1

1 Introduction

Various studies have been carried out on the fundamental properties as well as device performance involving one-dimensional (1D) nanomaterials. In this thesis, three types of 1D nanomaterials: silicon nanowires, silicon carbide (SiC) nanowires and boron nitride (BN) nanotubes are examined using synchrotron radiation-based spectroscopy: X-ray absorption fine structure (XAFS) and X-ray excited optical luminescence (XEOL) for their electronic structure and luminescence properties. For Si nanowires, the objective is to synthesize nanowire arrays using electroless chemical etching, and to study their electronic structure and charge redistribution upon noble metal (Pt and Au, to be specific) nanoparticles deposition. The optical properties of nanostructured Si upon thermal oxidation were also investigated. For SiC, emphasis is put on (1) experimental and theoretical study on electronic structure among SiC of different crystal structures and different crystal sizes, and (2) luminescence from SiC nanowires in comparison with their bulk counterparts. Lastly, for BN, the objective is to study the luminescence properties of BN nanotubes upon B isotope substitution and the presence of oxide impurities.

1.1 Nanostructures

1.1.1 General Background

Nanomaterials refer to materials with at least one dimension between 1 nm (10^{-9} m) and 100 nm. Such materials exhibit unique electrical and optical properties that are not possessed by their bulk counterparts. Nanostructures can be classified by their dimensions in nanoscale: two dimensional (2D) nanostructures are materials of a few

nanometers in thickness, such as thin films; nanoparticles and quantum dots are nanosized in all directions, so they are referred to as zero dimensional (0D) nanostructures. 1D nanostructures have nanosized diameters while they differ in length. Such nanostructures appear in various morphologies, such as nanowires, nanotubes, nanobelts and nanorods.

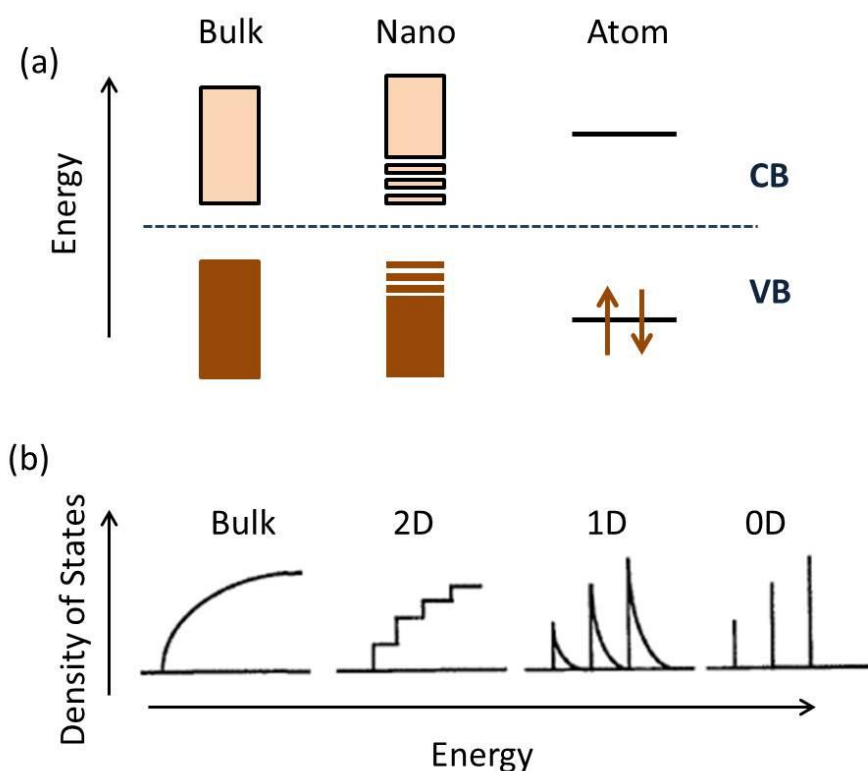


Figure 1-1 Schematic illustrations of density of states comparison (a) among bulk, nano and atom, and (b) among bulk and nanomaterials with specific dimensionality.

CB: conduction band, VB: valence band

The significance of nanostructure research is to study the aspect of size effect. On one hand, as the size of the materials is reduced, the energy levels become discrete, i.e. the structure is more atom-like, which is referred to as quantum confinement effect [1].

Figure 1-1 shows a schematic illustration of quantum confinement for electronic states of a semiconductor. When the size of the semiconducting particle is reduced to the nanoscale (smaller than the Bohr radius), a higher energy is required in order to promote electrons from the valence band to the conduction band, so-called “band gap widening”. Since the luminescence from semiconducting materials is usually associated with electronic transition between the valence and conduction band, controlling the size of the material also alters its optical properties. Luminescence from nanoparticles as a function of their sizes has been widely studied for light-emitting diode application. For example, by tuning the size of CdS nanoparticles, visible luminescence from red to deep purple can be produced [2,3]. In addition to near-band-gap radiative recombination, energy transfer to the optical channels involving defects, usually at longer wavelength (energy lower than the band gap), is also important and can be tailored [4,5]. Another significant observation is the visible luminescence from porous Si. Bulk Si is not light-emitting due to its indirect band gap, but upon quantum confinement, an indirect-to-direct band gap conversion takes place and porous Si emits orange-red luminescence [6,7]. In addition, development of nanostructured materials will contribute to the downsizing of the circuit dimension in electronic devices, and the high surface-to-volume atom ratio provides a large surface area for sensor, catalysis and drug delivery applications.

1D nanomaterials are of great importance since they provide good models to investigate the dependence of electronic, optical and mechanical properties on their morphologies and chemical compositions. Actually, 1D systems are the lowest dimensional structures that can provide efficient transport of electrons. The intensive interest in 1D nanomaterials was initiated by Iijima’s discovery of carbon nanotubes (CNT) in 1991[8].

Until now, CNT and related carbon-based nanostructures are still the spotlight of current research, especially in their applications as fuel cells, sensors, and batteries [9-11]. On the other hand, Si nanostructures are also of particular interest since Si is the most widely used and studied material in the semiconductor industry. Nanostructured silicon and the complicated interface between silicon and its oxide are found exhibiting quantum confinement effects, which opens the gate of many potential applications in electronic component, solar cells, and battery materials [12,13].

Apart from single element nanostructures, group IV and III-V nanostructured compounds have also attracted extensive interest due to their structural similarity to silicon and carbon. Although Si is not light-emitting, silicon carbide (SiC) has been used as a light emitting diode in early years due to its larger band gap [14,15]. Nanostructured SiC retains its superior physical stability as in its bulk form but of improved mechanical properties [16]. Boron nitride nanotubes (BNNT), as one of the III-V nanostructures, exhibit mechanical properties comparable to carbon nanotubes, but of much higher thermal stability [17-19]. In addition, BNNT is an insulator with a large band-gap compared to metallic and semiconducting CNT, making it a potential light-emitting source [20]. In this thesis, nanostructured Si, SiC and BN are chosen as the focus to examine their electronic structure and optical properties.

1.1.2 Nanomaterial Synthesis

The growth of 1D nanostructure requires the arrangement of atoms in a controlled manner: e.g. composition, size, growth direction and crystallinity. Various techniques have been developed to synthesize nanomaterials of desired morphologies and chemical compositions. In general, the synthesis methods can be classified into two groups: one is

“bottom-up”, in which the nanomaterials are assembled from the atomic or molecular level; the other one is “top-down”, in which nanostructures are produced by selectively etching a bulk surface.

The bottom-up method usually involves the use of a high temperature furnace, so that the source materials are evaporated and deposited onto a substrate. Whether there are chemical reactions evolved, the synthesis can be further categorized into physical vapor deposition (PVD) and chemical vapor deposition (CVD). While PVD is widely used for the growth of thin films, CVD and modified CVD methods can be used to grow thin films as well as a variety of 1D nanostructures such as nanowires and nanotubes. In a CVD system, the source materials are referred to as precursors, since normally each precursor only contributes to a single element in the final product. The precursors are diluted by carrier gas and introduced into the reaction chamber, and under high temperature, they decompose and react with each other. The reactant species are then deposited on the substrate. Typically, temperature and gas flow rate are the critical factors for nanostructure growth since they affect the morphology and composition of the final product. Recent advances in instrumentation allow precise control of experimental conditions so that nanostructures can be grown with desired morphology and composition.

Top-down synthesis of nanostructures is achieved using lithography or surface etching. Chemical etching is one of the efficient top-down methods to produce nanostructures on large scales. Such synthesis is typically carried out in an electrochemical cell. Starting with a piece of wafer or metal foil, chemical reaction takes place locally, driven by an external voltage or the red-ox potential at the electrolyte-electrode interface, and the

surface of the wafer (or foil) is selectively etched. The etching method has been used to produce wafer-scaled porous Si, Si nanowires and transition metal oxide nanotubes (e.g. TiO₂, ZrO₂) [21-23]. Compared to bottom-up methods, chemical etching uses a much simpler set-up, and the experimental conditions can be controlled by adjusting the concentration of electrolyte and the external voltage. More importantly, the nanostructures produced in this manner are directly attached to the substrate in a well-organized array, so that they can be further used as a substrate for growing secondary nanostructures (heterostructures). In addition, following this strategy, doped nanostructures can be formed by choosing the bulk wafer of desired dopant type and concentration. These methods have been used to prepare the materials studied in this thesis.

1.2 X-ray Absorption and Related Spectroscopy

1.2.1 X-ray Absorption Fine Structure

When light interacts with matters, it can be totally or partially absorbed, and the amount of light transmitted can be related to the intensity of incident light by Beer's law:

$$I = I_0 e^{-\mu t} \quad (1.1)$$

where I_0 is the intensity of incident light, and I is the intensity of light transmitted, t is the thickness of the sample, and μ is so-called the absorption coefficient. X-ray absorption fine structure (XAFS) refers to the variation of μ as a function of X-ray energy (E) of an atom in a certain chemical environment [24]. When the incoming X-ray energy is equal to and higher than the binding energy of a core electron, a significantly increased amount of X-ray energy (number of photons) is absorbed due to the increase of absorption cross-

section. Experimentally a sharp rise of μ is observed, referred to as the absorption edge. Such features appear when the absorbed energy is sufficient to promote the core electron to an unoccupied bound state, quasi-bound state, and further to the continuum (photoelectric effect). Figure 1-2 shows the atomic absorption cross section of platinum as a function of X-ray energy (E) [25]. It can be seen that several absorption edges appear at energies which correspond to the core electrons at different levels being excited, labeled as L_1 , L_2 , L_3 , and K. K-edge refers to the excitation of the $1s$ core electrons, L_1 -edge is the energy at which the $2s$ core electrons are excited, and $L_{2,3}$ -edge is the excitation of the $2p_{1/2}$ and $2p_{3/2}$ electrons, etc. For atoms in a chemical environment, fine structures are observed when the outgoing electrons are interfering with the neighboring atoms (multiple or single scattering). XAFS hence describes the energy-dependency of μ above the absorption edge when the absorbing atom is in a chemical environment.

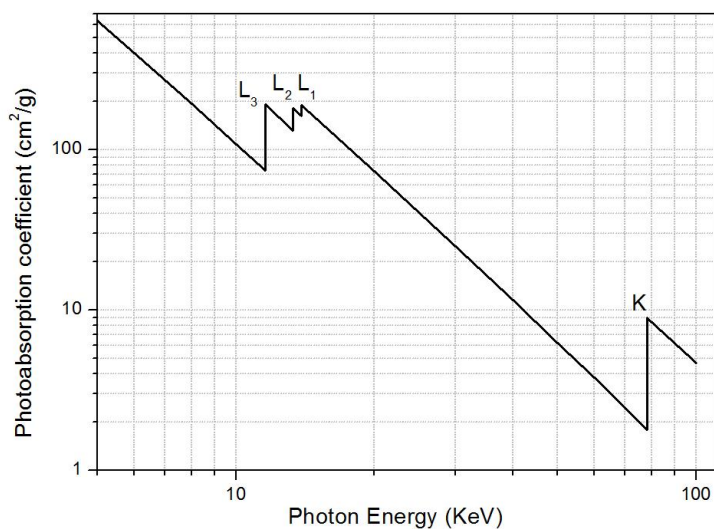


Figure 1-2 Log-log plot of the mass absorption coefficient of platinum as a function of X-ray photon energy.

XAFS is usually divided into two regimes, and they are interpreted differently, simply because the electron scattering behavior of atoms is dependent on the kinetic energy of the electrons. Within 20 eV below and 50 eV above the absorption edge is the near-edge region, referred to as “X-ray absorption near-edge structure” (XANES); from 50 eV to 1000 eV above the edge is the extended XAFS region (EXAFS). In XANES, the modulation of μ is mainly caused by electronic transition into bound, quasi-bound states and multiple scattering from the surrounding atoms (kinetic energy of the outgoing electron is low). It is highly sensitive to the local chemical environment, such as oxidation states, unoccupied electronic states, and local symmetry, so it can be used as “fingerprints” of the materials [26]. EXAFS on the other hand, is dominated by single scattering (the outgoing electron has high kinetic energy). Local structures such as bond length within first 2 or 3 atomic shells can be obtained by analyzing EXAFS data [27,28]. XAFS is powerful to study the local structures of materials not limited to crystalline samples but also non-crystalline, gas or liquid ones. In this thesis, research is mainly focused on the XANES region, details of which are given below.

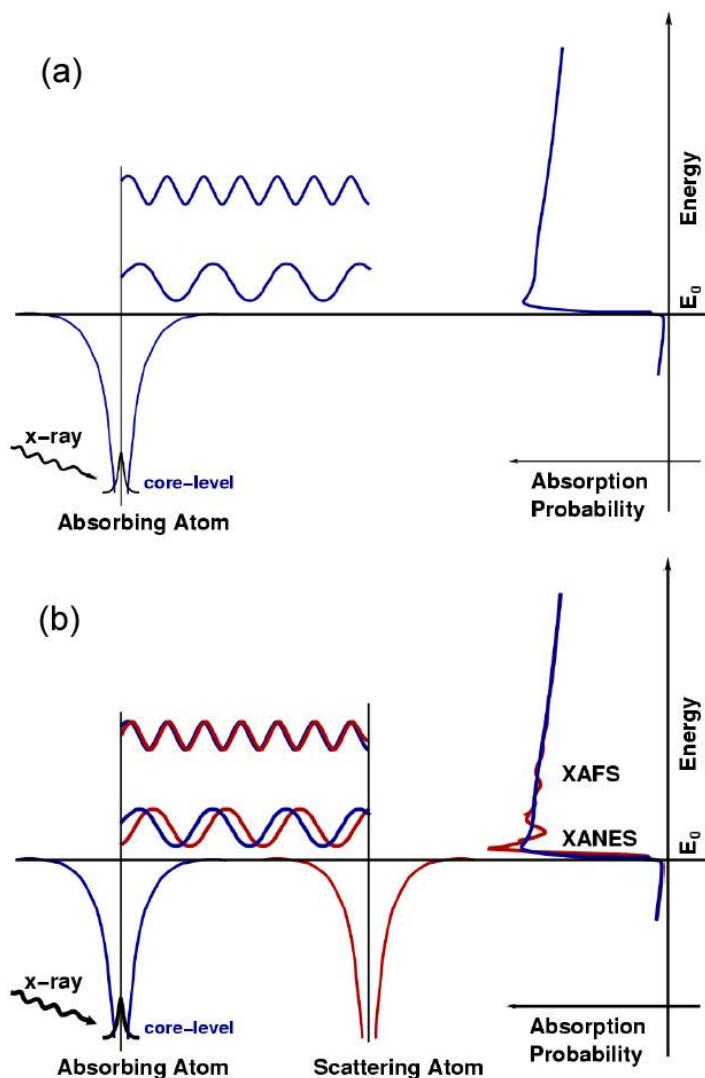


Figure 1-3 Schematic illustration of the outgoing photoelectron wave produced by (a) a free atom and (b) a diatomic system upon X-ray absorption and the corresponding XANES spectrum [29].

In XANES, when the incident X-ray energy is equal or slightly above the absorption threshold of the element of interest in the material, the core electron is promoted to previously unoccupied bound and quasi-bound states. Figure 1-3 shows a schematic diagram comparing the features of outgoing waves produced from a free atom and an

atom in a chemical environment (e.g. a diatomic system). In a free atom (Figure 1-3(a)), once the X-ray has the energy (E) higher than the binding energy of the core-level electron (E_0), photon-electron is created which travels as a wave with wave number proportional to $\sqrt{(E - E_0)}$. In the XANES spectrum, a monotonic decrease in μ is seen after the edge jump, since there are no neighboring atoms which can scatter the photoelectrons. In a diatomic system (Figure 1-3(b)), once the photoelectron is created by the absorbing atom, the outgoing photoelectron wave encounters its neighboring atom (scattering atom), and it scatters the initial wave. The constructive and destructive interference between the outgoing and backscattered waves creates modulations in the absorption coefficient, and oscillations are observed in XANES spectrum. In an atomic cluster, multiple scattering comes from all the neighboring atoms, resulting in several scattering pathways. The total absorption coefficient can be written as

$$\mu(E) = \mu_0[1 + \sum_{n \geq 2} \chi_n(E)] \quad (1.2)$$

where μ_0 is the absorption coefficient of a single atom (as the situation in Figure 1-3(a)), and $\chi_n(E)$ is the contribution arising from all scattering pathways involving $n-1$ neighboring atoms. Figure 1-4 shows a schematic view of the multiple scattering processes for n of different values. The amplitude and the spectral profile in XANES are thus affected by the structural factors of the materials, such as bond length, symmetry, and ligands.

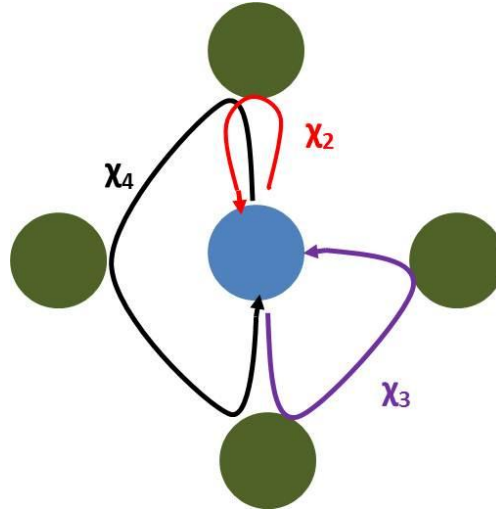


Figure 1-4 Schematic view of the multiple scattering processes of several scattering pathways, where $n=2, 3,$ and 4 in χ_n indicates the number of atoms involved in a scattering pathway.

In theory, the absorption coefficient μ can be described as the probability of a photon being absorbed producing an electron transition between the initial and final quantum states. The final electronic state is often considered using the one-electron approximation, in which X-ray absorption is described by a single-particle process. The single core-level electron in an N -electron system is excited into an unoccupied level, leaving fully relaxed $N-1$ electrons with a core hole. According to Fermi's gold rule, $\mu(E)$ is proportional to the transition matrix element which is described as follows:

$$\mu \propto |\langle \psi_f | H | \psi_i \rangle|^2 \delta(E_f - E_i - \hbar\omega) \quad (1.3)$$

$$H = \hat{\mathbf{p}} \cdot \mathbf{A}(\mathbf{r}) \quad (1.4)$$

where $|\psi_i\rangle$ and $|\psi_f\rangle$ are initial and final electronic states with eigenvalues of E_i and E_f , respectively, and H is the interaction Hamiltonian between the electromagnetic field

(vector potential $\mathbf{A}(\mathbf{r}) \cong \hat{\mathbf{e}}A_0e^{i\mathbf{k}\cdot\mathbf{r}}$) and the electron (momentum operator $\hat{\mathbf{p}}$). The δ function is for energy conservation and can be correlated to the density of states (ρ). In addition, the spatial dependence of the vector potential \mathbf{A} can be neglected (dipole approximation), i.e. $e^{i\mathbf{k}\cdot\mathbf{r}} \cong 1$. Under the one-electron dipole approximation, the expression of absorption coefficient $\mu(E)$ in Equation 1.3 can be re-written as

$$\mu(E) \propto |\langle \psi_f | \boldsymbol{\epsilon} \cdot \mathbf{r} | \psi_i \rangle|^2 \cdot \rho \quad (1.5)$$

The major contribution in the XANES spectra is the dipole transition, i.e. transitions of $1s$ to p , $2p$ to $s+d$, etc. The quadrupole component, though much weaker, may also play an important role, particularly in the K-edge XANES of transition metals. It was found that quadrupole transition (e.g. $1s$ to $3d$) causes weak oscillations before the main absorption edge appears (pre-edge features), which is highly sensitive to metal d electron-ligand hybridization [30,31].

XANES can also be described using the band structure theory. In the band structure approach described by Müller *et al.*, [32] the absorption coefficient of the core electron can be written as

$$\mu(E) = \frac{4\pi^2\alpha}{\Omega/v} F(E) \quad (1.6)$$

where α is the inverse fine-structure constant ($\alpha^{-1}=137.036$), Ω is the volume of the primitive cell and v is the number of contributing atoms in the primitive cell. $F(E)$ is the spectral distribution of oscillator strength, which contains contributions from an atomic term and a solid-state term. The overall magnitude and shape of the spectrum is determined by the atomic transition associated with the core-electron excitation, and the

fine structure is determined by the solid state term, which is proportional to the projected partial density of states of the band structure.

1.2.2 De-excitation Processes Following the X-ray Absorption

After a core electron is excited upon X-ray absorption, several de-excitation processes occur to fill the core-hole. The de-excitation can be either non-radiative, by ejecting Auger electrons, or radiative, by emission of X-ray fluorescence. Figure 1-4 shows a schematic diagram of the Auger and fluorescence decay processes. Once the incident photon has energy sufficient to excite a core electron into continuum, a core hole is created (Figure 1-5(a)). In the Auger process, an electron at shallower level fills the core hole, and the released energy is transferred to another electron to promote it into continuum (Figure 1-5(b)). Alternatively, the energy can be released by emission of a fluorescence photon (Figure 1-5(c)). Both the Auger yield and fluorescence yield are proportional to the absorption coefficient $\mu(E)$ of the element measured, since they are directly related to the probability of the presence of core-hole created by X-ray absorption. The two decay channels are competing processes; in other words, the fractions of Auger yield and fluorescence yield relative to the total decay add up to 1 [33]. For low Z elements, Auger decay is the dominated channel, while for heavy elements, fluorescence decay dominates [33].

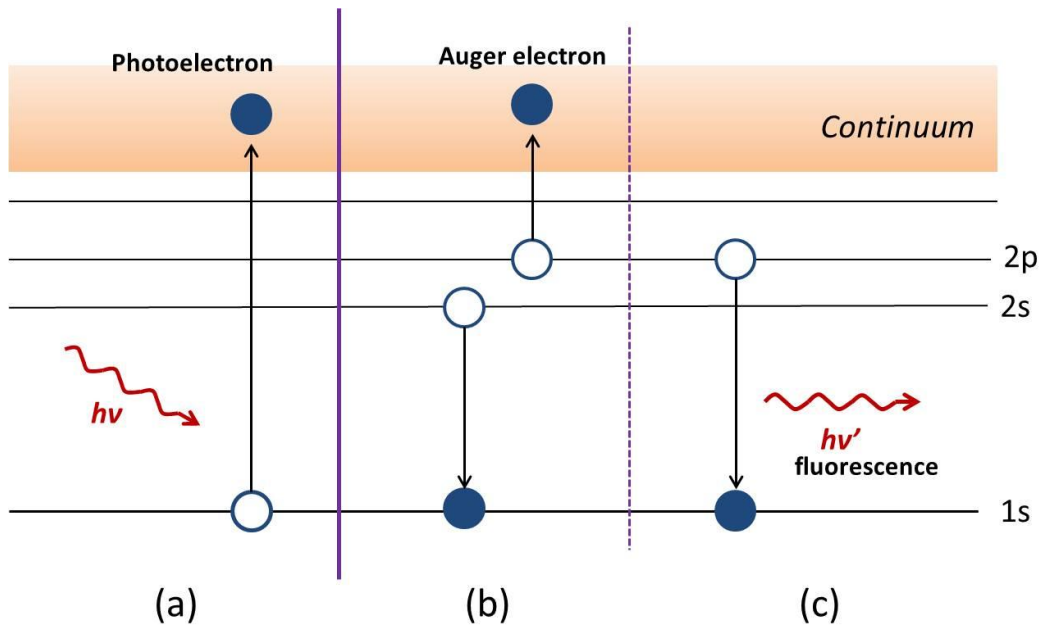


Figure 1-5 Schematic diagram of the de-excitation processes upon core electron excitation. (a) photo-absorption resulting a photoelectron and a core hole, (b) Auger process, (c) X-ray fluorescence. Solid circles: electrons, open circles: holes.

1.2.3 Recombination Process: X-ray Excited Optical Luminescence

Once the core electron is excited, Auger and fluorescence decay processes take place to fill the core hole, resulting in the creation of holes at outer shells and excessive energy to excite electrons at shallower levels. Such secondary excitation continues and produces electron-hole pairs in a cascade manner until the energy is too low for further electronic excitation. In semiconductors, the electron/hole undergoes thermalization until the electron reaches the bottom of the conduction band and the hole reaches the top of the valence band. Then they form an electron-hole pair (exciton) which recombines and the energy is released either radiatively (optical photon) or non-radiatively (phonon). The

radiative recombination process with optical photon emission is called X-ray excited optical luminescence (XEOL). The process is shown schematically in Figure 1-6. The recombination can be direct, via the formation of an exciton, which typically has the binding energy of a few meV, so that the emitted light has energy equal to the energy difference between the band gap and the exciton binding energy. The recombination can also be indirect, with the assistance of a phonon. In addition, luminescence also takes place in presence of trapped holes, electrons, or impurities, which cause the emission of energy lower than the band gap. The recombination process is essentially similar to the conventional photoluminescence (PL), though the latter uses a laser as excitation source so that only valence electrons are primarily excited.

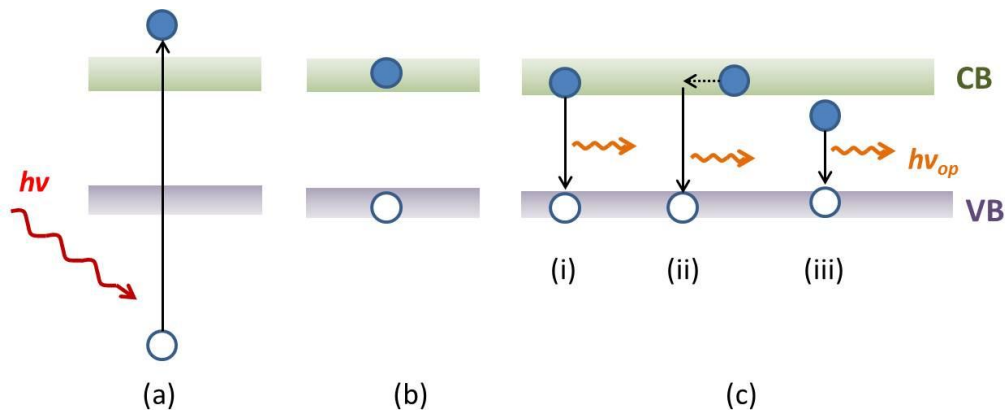


Figure 1-6 Schematic diagram of the electron-hole pair generation and recombination. (a) core electron excitation, (b) electron and hole thermalization, (c) examples of radiative recombination via (i) direct recombination, (ii) phonon-assisted indirect recombination, (iii) presence of traps

Since XEOL uses X-ray of energy sufficient to excite core-level electrons in the material, the luminescence phenomenon is associated with the absorption process of the core electrons. As for conventional PL or cathodoluminescence (CL) spectroscopy, a single-energy excitation source is used and the observed luminescence comes from contributions of all valence electrons-hole recombination. In XEOL, a tunable X-ray source can be applied to excite core electrons at specific energy level, so different de-excitation channels can be selectively measured. For example, in a multi-element or multi-component sample (e.g. an alloy or a heterostructure), if the energy transfer is favored in optical decay of one element in one chemical environment, the variation of absorption coefficient of that element across the edge is usually in accord with the variation of the XEOL intensity. The luminescence detected while exciting the core-level of other elements in that material will be less sensitive to the changing of absorption coefficient [34,35]. As a result, XEOL is often combined with XAFS to investigate the luminescence mechanism of materials with element and site specificity.

1.3 Synchrotron Radiation Overview

In order to perform the XAFS and related measurements, a tunable X-ray source is essential, which can be provided by synchrotron radiation. In fact, the development of the XAFS experimental technique and theory goes hand in hand with the advance of synchrotron radiation instrumentation. A synchrotron is a bright light source. The light is produced by accelerating electrons approaching the speed of light. When the accelerated electrons are directed in a curved orbit under a magnetic field, electromagnetic radiation is produced tangentially to the orbit. The radiated power (P) can be described using

Equation 1.7, where e is the electron charge, c is the speed of light, E is the energy of electron (in GeV), m_0 is the rest mass of the electron, and ρ is the radius of the curvature.

$$P = \frac{2e^2 c E^4}{3(m_0 c^2)^4 \rho^2} \quad (1.7)$$

Although the theoretical description of synchrotron radiation was established in the 1920s, the development of dedicated synchrotron radiation sources was not carried out until the 1960s when it became widely recognized as a powerful tool [36]. In 1968, Tantalus I, the first dedicated synchrotron radiation source became operational [37]. Since then, synchrotron radiation has been used for various ultraviolet and X-ray experiments, and synchrotron radiation facilities were built all over the world. The development of synchrotron radiation instrumentation led to the emergence of second-generation synchrotron sources such as BESSY I (Germany), NSLS (US) and Aladdin (US). Later, with the introduction of insertion devices such as undulators and wigglers (details will be given below), the third generation synchrotron facilities are able to offer synchrotron radiation of much higher brightness. The Canadian Light Source (Canada) and The Advanced Photon Source (US) where the research in this thesis was carried out are both third generation synchrotron facilities.

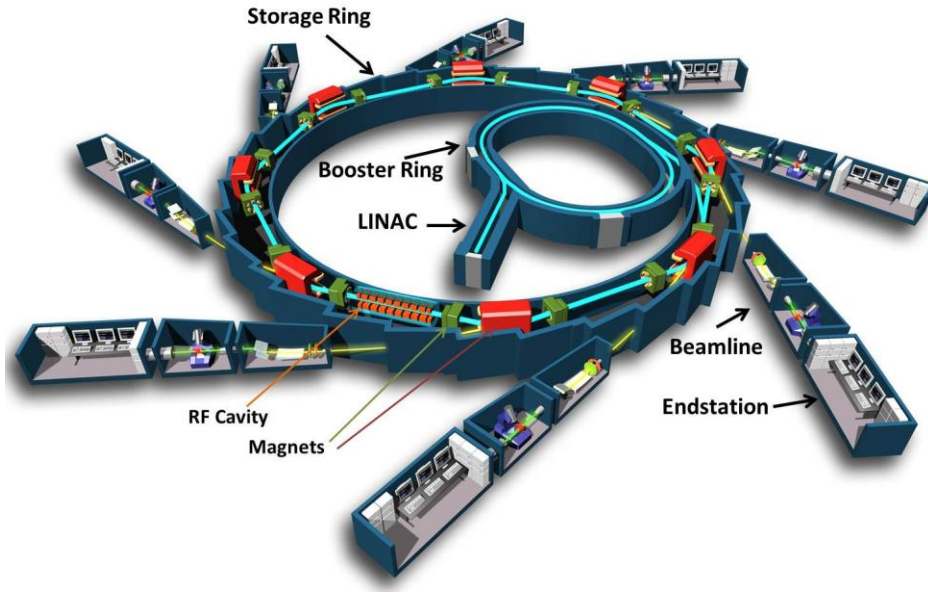


Figure 1-7 Schematic layout of a synchrotron radiation facility.

Figure 1-7 shows a schematic layout of a synchrotron radiation facility. The electrons are emitted by heating a cathode to $\sim 1000\text{ }^{\circ}\text{C}$ under direct current high voltage, and are fed into the linear accelerator (LINAC). In the LINAC, they are accelerated under another high voltage to a speed close to the speed of light with an energy of hundreds of MeV. The electrons are then injected into the booster ring and further accelerated to reach the 99.9999985% of the speed of light [38]. After the energy of electrons gets accumulated to the order of GeV, electrons are transferred into the storage ring, where they will circulate for several hours. The direction of the accelerated electrons (electron beam) is controlled by several bending magnets (dipole magnets, indicated as red-colored components in Figure 1-7) located around the circulator orbit, which bend the beam by short arcs that make up a 360° bending in total. Quadrupole magnets (indicated as green-colored components in Figure 1-7) are placed in the storage ring to maintain the transverse dimension of the beam. The energy loss as synchrotron radiation by circulating electrons

is replenished by a radio-frequency (RF) cavity, which applies an alternating electric field to add energy to increase or maintain the electron travelling speed.

As mentioned above, synchrotron radiation is emitted while the trajectory of the accelerated electrons is altered. This is achieved by the use of magnets, which are of two categories, shown in Figure 1-8 (a). The bending magnets, which are dipole magnets, are installed at the curved section of the storage ring. The wigglers and undulators, known as “insertion devices”, are arrays of magnets of alternating polarity and are placed at the straight section of the storage ring. Each type of magnets provides radiation of different spatial distribution, which is distinguished by the opening angle ($1/\gamma$), where γ is the ratio of the mass of a relativistic electron to its rest mass (Equation 1.8).

$$\gamma = \frac{E}{m_0 c^2} \quad (1.8)$$

As shown in Figure 1-8(a), a bending magnet produces sharp cone sweeps in the bending plane. Wiggler and undulator are of similar configurations, in which electrons are bent periodically, and radiation is produced at each bent. With a high magnetic field, the wiggler produces radiation beam of a large open angle ($\gg 1/\gamma$); while in the undulator, the electrons has smaller bend under lower magnetic field, resulting a narrower beam of higher brightness (number of photons per second per source area per unit angle). In the spectral distribution, shown in Figure 1-8 (b), radiated energy is continuous for both bending magnet and wiggler, the latter of which is brighter. The spectrum for an undulator consists of a series of sharp peaks of much higher brightness [39].

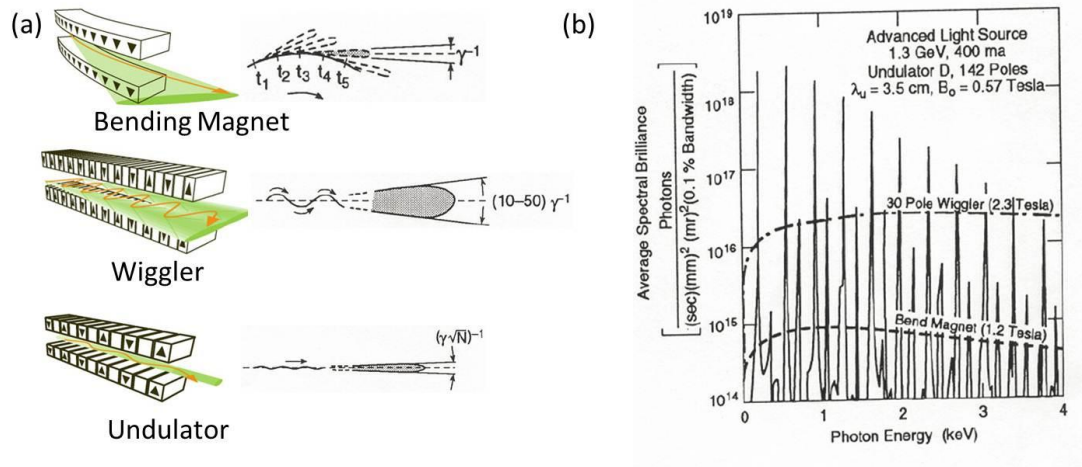


Figure 1-8 (a) schematic layout and (b) comparison of the spectral distribution of bending magnet, wiggler and undulator. γ is the opening angle, and N is the number of magnets.

Since the radiation generated from the synchrotron covers a broad energy range from infrared (IR) to hard X-ray, monochromators are installed to choose a specific energy.

The beam from the storage ring is directed by sets of mirrors and slits to the monochromator before it reaches to the endstation. For X-ray measurements, two types of monochromators are used depending on the energy range required by the experiment.

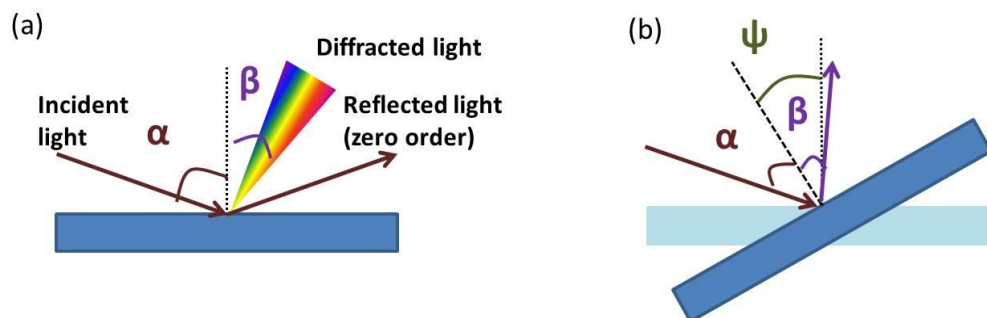


Figure 1-9 Schematic illustration of the plane grating monochromator at (a) zero order position, and (b) rotated position.

Grating monochromators are usually designed for soft X-ray beamlines. The grating refers to arrays of lines with well-defined separation and profile. The design of the monochromator is based on the diffraction theory. The incident beam hits the monochromator at grazing angle, and different energy gets diffracted at different angles. To keep the exit beam at a fixed angle, monochromatic light can be obtained by moving the optical aperture or by rotating the grating. The grazing incidence grating monochromators can be further divided into three types: plane grating, spherical grating, and aspheric grating [40]. The basic physical principle is the same among the three. Take the plane grating for example, the relationship between angle of incidence (α) and angle of diffraction (β) is shown in Equation 1.9, where k is the diffraction order, λ is the wavelength, N is so-called “grating density”, which is defined by number of lines divided by the line width.

$$Nk\lambda = \sin \alpha + \sin \beta \quad (1.9)$$

While the beam comes in at incident angle, α value is controlled by rotating the plane, shown in Figure 1-9. The rotation of the grating can be described using two parameters: the angle of grating rotation away from the normal (zero order) position (ψ), and the deviation angle (θ) of the grating (Equation 1.10). As can be seen in Figure 1-9, the selection of wavelength (energy) is limited by angles α and β , i.e. neither of them can exceed 90° . The “cut-off” wavelength is thus given by Equation 1.11.

$$\theta = \frac{\alpha - \beta}{2} \quad (1.10)$$

$$\lambda_c = 2\cos^2\theta/Nk \quad (1.11)$$

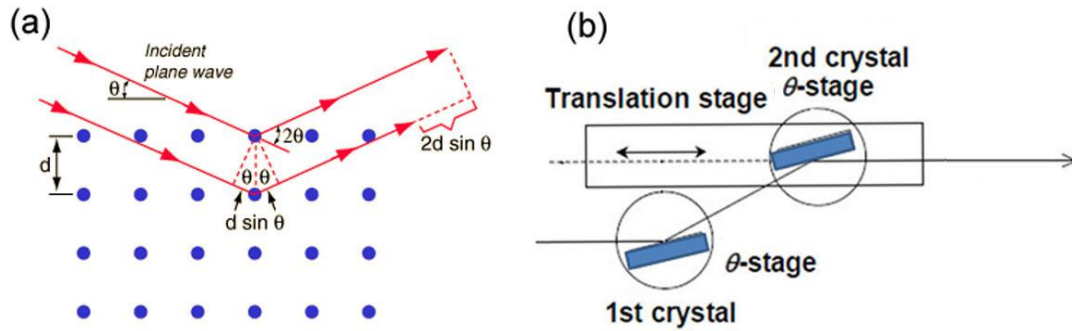


Figure 1-10 (a) Bragg diffraction. (b) Schematic layout of a double-crystal monochromator

Beamlines operating at hard X-rays usually employ double-crystal monochromators (DCM). The energy selection is based on Bragg's law, illustrated in Figure 1-10(a): the outgoing waves undergo constructive interference when Bragg's condition (Equation 1.12) is satisfied:

$$n\lambda = 2d \sin \theta \quad (1.12)$$

where n is the order of diffraction, λ is the wavelength, θ is the Bragg angle, and d is the lattice spacing of the crystal. In a DCM, two perfect crystals of the same physical parameters (i.e. same element and same d -spacing) are installed parallel to each other, as can be seen in Figure 1-10(b). The energy selection is done by rotation and translation of the two crystals so that the outgoing beam is at a fixed angle. Figure 1-10(b) shows one example of the crystal arrangements: the first crystal is mounted in such a way that it is able to rotate to get different incident beam angles (θ). The second crystal rotates and translates to direct the Bragg diffracted beam to a fixed exit point. The commonly used crystals are Si (111), Si (333), InSb (111), etc. The type of crystal or the crystal of certain

orientation (differs in d value) is selected depending on the energy range required for the measurements.

Overall, there are several advantages of using synchrotron radiation instead of traditional X-ray source[41]: (1) the photon energy is tunable from IR to hard X-ray using monochromators; (2) the flux (number of photon per second per milliradian of horizontal angle per 0.1% bandwidth integrated over all vertical angles) is as much as 12 orders of magnitude than the traditional X-ray and of much higher brightness; (3) the beam is highly collimated, which is able to provide spectra of high spatial resolution; (4) the photons are linearly polarized in the plane of the orbit and elliptically polarized out of the orbit plane; (5) the use of RF cavity produces bunched electrons so that the emitted light is pulsed with a few nanoseconds between pulses, which allows for performing time-gated spectroscopy.

1.4 Outline of Thesis

The outline of the thesis is as follows. Chapter 1 provides a general introduction of 1D nanomaterials, and a detailed description on the X-ray absorption spectroscopy techniques (XANES and XEOL) as well as an overview of synchrotron radiation.

Chapter 2 describes the instrumentation of synchrotron facilities, the experimental methods as well as XANES spectra calculation process. Chapter 3 discusses electronic structures of Si nanowires upon Pt and Au nanoparticles deposition studied using XANES and X-ray photoelectron spectroscopy (XPS). In Chapter 4, luminescence properties of various Si nanostructures are comparatively studied and their luminescence mechanism investigated using XEOL. Chapter 5 is a systematic study of SiC materials. XANES and XEOL are compared among SiC nanowires, SiC-SiO₂ core-shell nanowires,

SiC micro- and nanocrystals of different polytypes. The electronic structures among different polytypes are calculated and compared with experimental results. Chapter 6 contains electronic structure and luminescence study of BN nanotubes. The effect of isotope substitution and presence of oxide on the luminescence of BN is discussed. Chapter 7 contains the conclusions of the studies described in the thesis and a description of future work which shall be undertaken. Finally, in Appendix A, detailed synthesis procedure of Si nanowires via metal-assisted chemical etching is included, together with investigation on the experimental factors of the morphology control and a discussion on the etching mechanism.

1.5 References

- [1] Alivisatos, A. P., *Science* **1996**, *271*, 933-937.
- [2] Herron, N.; Wang, Y.; Eckert, H., *J. Am. Chem. Soc.* **1990**, *112*, 1322-1326.
- [3] Vossmeier, T.; Katsikas, L.; Giersig, M.; Popovic, I. G.; Diesner, K.; Chemseddine, A.; Weller, H., *J. Phys. Chem.* **1994**, *98*, 7665-7673.
- [4] Armelao, L.; Heigl, F.; Jurgenen, A.; Blyth, R. I. R.; Regier, T.; Zhou, X. T.; Sham, T. K., *J. Phys. Chem. C* **2007**, *111*, 10194-10200.
- [5] Armelao, L.; Heigl, F.; Brunet, S.; Sammynaiken, R.; Regier, T.; Blyth, R. I. R.; Zuin, L.; Sankari, R.; Vogt, J.; Sham, T. K., *ChemPhysChem* **2010**, *11*, 3625-3631.
- [6] Takagahara, T.; Takeda, K., *Phys. Rev. B* **1992**, *46*, 15578-81.
- [7] Delerue, C.; Allan, G.; Lannoo, M., *Phys. Rev. B* **1993**, *48*, 11024-11036.
- [8] Iijima, S., *Nature* **1991**, *354*, 56-58.
- [9] Baughman, R. H.; Zakhidov, A. A.; de Heer, W. A., *Science* **2002**, *297*, 787-792.

- [10] Wang, J., *Electroanal.* **2005**, *17*, 7-14.
- [11] Cheng, H. M.; Yang, Q. H.; Liu, C., *Carbon* **2001**, *39*, 1447-1454.
- [12] Chen, L. J., *J. Mater. Chem.* **2007**, *17*, 4639-4643.
- [13] Shao, M.; Ma, D. D. D.; Lee, S. T., *Euro. J. Inorg. Chem.* **2010**, *27*, 4264-4278.
- [14] Hoffmann, L.; Ziegler, G.; Theis, D.; Weyrich, C., *J. Appl. Phys.* **1982**, *53*, 6962-6967.
- [15] Edmond, J.; Kong, H.; Suvorov, A.; Waltz, D.; Carter, C. J., *Phys. Stat. Sol. (a)* **1997**, *162*, 481-491.
- [16] Zekentes, K.; Rogdakis, K., *J. Phys. D: Appl. Phys.* **2011**, *44*, 133001.
- [17] Chopra, N. G.; Luyken, R. J.; Cherrey, K.; Crespi, V. H.; Cohen, M. L.; Louie, S. G.; Zettl, A., *Science* **1995**, *269*, 966-7.
- [18] Suryavanshi, A. P.; Yu, M. F.; Wen, J. G.; Tang, C.; Bando, Y., *Appl. Phys. Lett.* **2004**, *84*, 2527-2529.
- [19] Chen, Y.; Zou, J.; Campbell, S. J.; Le Caer, G., *Appl. Phys. Lett.* **2004**, *84*, 2430-2432.
- [20] Blase, X.; Rubio, A.; Louie, S. G.; Cohen, M. L., *Europhys. Lett.* **1994**, *28*, 335-340.
- [21] Canham, L. T., *Appl. Phys. Lett.* **1990**, *57*, 1046-8.
- [22] Zhang, M.-L.; Peng, K.-Q.; Fan, X.; Jie, J.-S.; Zhang, R.-Q.; Lee, S.-T.; Wong, N.-B., *J. Phys. Chem. C* **2008**, *112*, 4444-4450.
- [23] Zwilling, V.; Aucouturier, M.; Darque-Ceretti, E., *Electrochimica Acta* **1999**, *45*, 921-929.
- [24] Bunker, G., *Introduction to XAFS. A practical guide to X-ray absorption fine*

structure spectroscopy. Cambridge University Press: 2010.

- [25] <http://physics.nist.gov/PhysRefData/FFast>
- [26] Stohr, J., *NEXAFS spectroscopy*. Springer: 1992; Vol. 25.
- [27] Stern, E. A.; Sayers, D. E.; Lytle, F. W., *Phys. Rev. B* **1975**, *11*, 4836-4846.
- [28] Rehr, J. J.; Albers, R. C., *Rev. Mod. Phys.* **2000**, *72*, 621-654.
- [29] Newville, M. *Fundamentals of XAFS*; Consortium for Advanced Radiation Source, University of Chicago, Chicago, IL: July, 2004.
- [30] de Groot, F. M. F., *Chem. Rev.* **2001**, *101*, 1779-1808.
- [31] de Groot, F. M. F.; Kotani, A., *Core-level Spectroscopy of Solids*. CRC Press, Taylor & Francis Group: 2008.
- [32] Müller, J. E., Wilkins, J. W., *Phys. Rev. B* **1984**, *29*, 4331-4348
- [33] Krause, M. O.; Oliver, J. H., *J. Phys. Chem. Ref. Data* **1979**, *8*, 329-38.
- [34] Sham, T. K.; Jiang, D. T.; Coulthard, I.; Lorimer, J. W.; Feng, X. H.; Tan, K. H.; Frigo, S. P.; Rosenberg, R. A.; Houghton, D. C.; Bryskiewicz, B., *Nature* **1993**, *363*, 331-334.
- [35] Sham, T. K.; Naftel, S. J.; Kim, P. S. G.; Sammynaiken, R.; Tang, Y. H.; Coulthard, I.; Moewes, A.; Freeland, J. W.; Hu, Y. F.; Lee, S. T., *Phys. Rev. B* **2004**, *70*, 045313.
- [36] Koch, E.-E.; Eastman, D. E.; Farge, Y., *Synchrotron radiation-a powerful tool in science*. North-Holland Publishing Company: 1983; Vol. 1.
- [37] Rowe, E. M.; Mills, F. E., *Particle Accelerators* **1973**, *4*, 211-227.
- [38] Walker, T. *Introduction to synchrotron radiation*; Canadian Light Source.

[39] Winick, H., Introduction and Overview. In *Synchrotron Radiation Sources: a primer*, Winick, H., Ed. World Science: 1994; Vol. 1.

[40] Johnson, R. L., Grating Monochromators and optics for the VUV and soft X-ray region. In *Handbook on Synchrotron Radiation*, Koch, E. E., Ed. North-Holland Publishing Company: 1983; Vol. 1A.

[41] Sham, T. K.; Rivers, M. L., *Rev. Mineralogy & Geochem.* **2002**, *49*, 117-147.

Chapter 2

2 Synchrotron Instrumentation and XAFS Calculation

2.1 Synchrotron Facilities

2.1.1 Canadian Light Source (CLS)

Canadian Light Source (CLS) is a third-generation synchrotron source located in the University of Saskatchewan, Saskatoon, Canada. Figure 2-1 shows the schematic layout of the CLS beamlines. It has 12 straights (9 available for insertion devices), 24 bending magnets, and over 40 possible beamlines. Currently there are 14 operating beamlines (and three under construction) which provide photon energy range from Far IR to hard X-ray and are designed to meet specific experimental techniques. The storage ring operates at an energy of 2.9 GeV and at current up to 500 mA. It has a circumference of 171m, radio frequency of 500 MHz, and the emittance of 18.2 nm·rad [1].

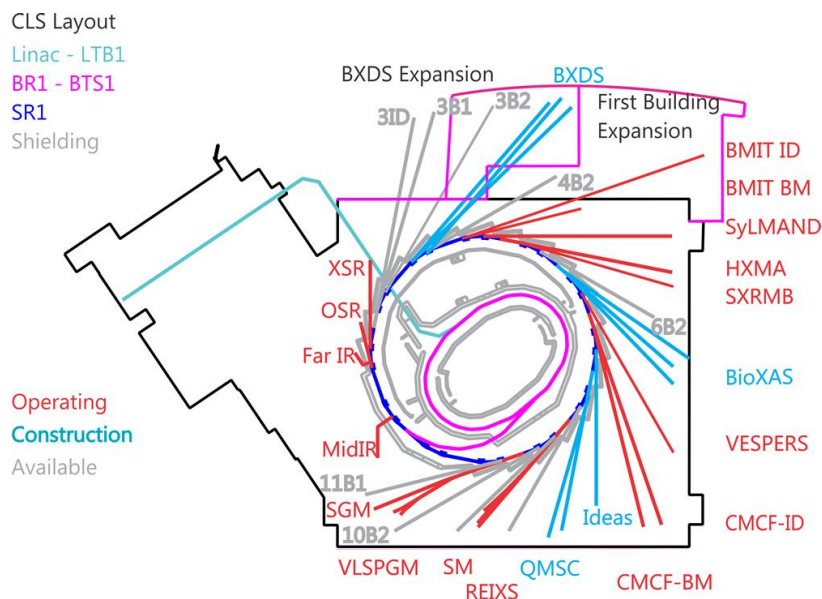


Figure 2-1 Schematic layout of the CLS beamlines as of Feb, 28, 2012[2].

2.1.2 Advanced Photon Source (APS)

Advanced photon Source (APS) is located at Argonne National Laboratory, Argonne, Illinois, USA. It is a third generation light source with a 7 GeV storage ring of 1104m circumference. The layout of the beamlines is shown in Figure 2-2. It consists of 34 sectors, and each sector contains one or more beamlines for a variety of researches. The APS operates with a storage beam current of 102 mA that runs in “top-up” mode, which means the beam is kept as a constant beam current by injection every 2 minutes. It has radio frequency of 351.927 MHz, and an electron beam emittance of 2.514 nm·rad [3].

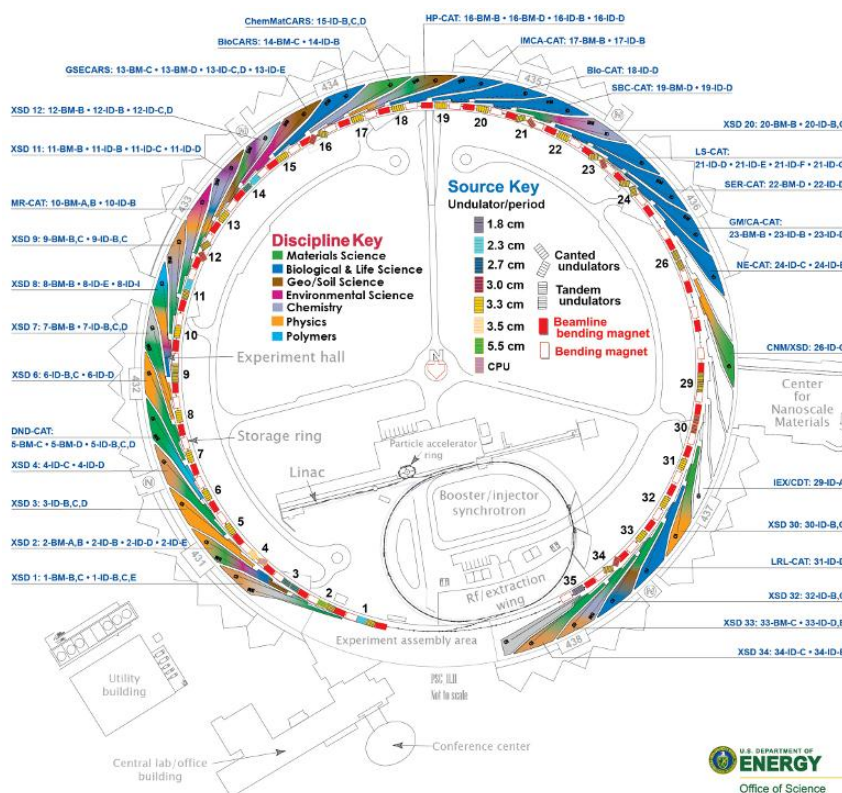


Figure 2-2 Schematic layout of the APS beamlines [4].

2.2 Beamlines

2.2.1 Variable Line Spacing Plane Grating Monochromator (VLS-PGM) Beamline–CLS 11ID-2

The VLS-PGM beamline (CLS 11ID-2) covers the energy range of 5-250 eV with a resolution $E/\Delta E > 10000$ and spot size of $500\ \mu\text{m} \times 500\ \mu\text{m}$ [5,6]. The layout of the beamline is shown in Figure 2-3. A toroidal mirror (M2) is used to focus the beam onto the entrance slit, and three spherical mirrors (M3) combined with three variable line spacing plane gratings are used to cover the desired energy range, i.e. low energy grating: 5-38 eV; medium energy grating: 25-120 eV; high energy grating: 90-250 eV. A plane mirror (M4) can be inserted to deflect the beam onto a second endstation (endstation B) for photoemission spectroscopy measurement. Mirrors M5 and M6 are for re-focusing the beam to its corresponding endstation. Endstation A is for XANES and corresponding XEOL measurements. With slit size of $50\ \mu\text{m} \times 50\ \mu\text{m}$, a photon flux of up to 2×10^{12} photons/s per 100 mA can be achieved. In this study, the Si $L_{3,2}$ -edge and B K-edge of various compounds were investigated at the VLS-PGM beamline.

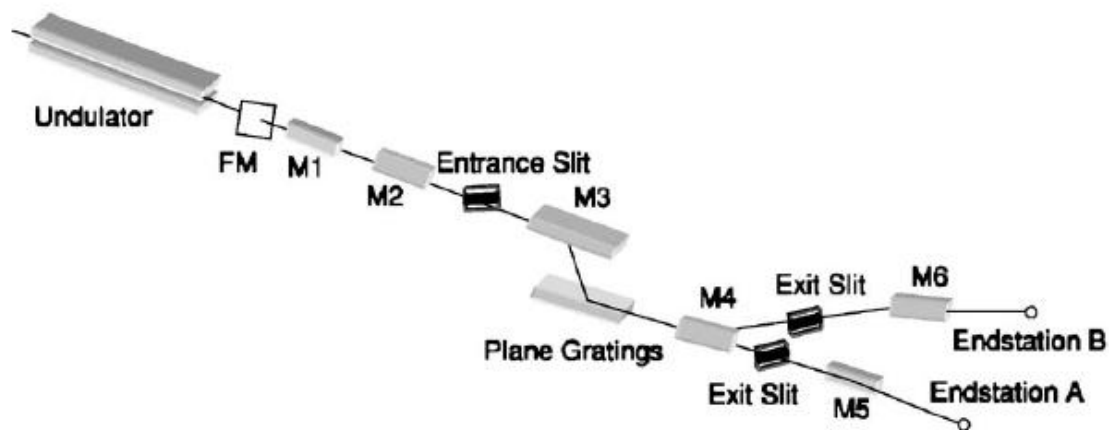


Figure 2-3 Layout of VLS-PGM beamline [5]. FM, fixed mask; M1, plane mirror; M2, toroidal mirror; M3, spherical mirror; M4, plane mirror; M5 and M6, toroidal refocusing mirrors

2.2.2 High Resolution Spherical Grating Monochromator (SGM) Beamline-CLS 11ID-1

The SGM beamline (11ID-1) at CLS covers the energy range of 250 eV-2000 eV, which is ideal for studying K-edges of low-Z elements and L-edges of transition metals. It is a dragon-type monochromator, and the layout of the beamline is shown in Figure 2-4.

Three gratings are available to choose for the desired energy range: low energy grating: 250-700 eV, medium energy grating: 450-1250 eV, and high energy grating: 740-2000 eV. The resolution $E/\Delta E$ is greater than 5000 at energy below 1500 eV with spot size of $1000\ \mu\text{m} \times 100\ \mu\text{m}$. The beamline flux (photons/s) at 100 mA is $>10^{12}$ at 250 eV and $>10^{11}$ at 1900 eV [7]. The beamline contains two endstations, referred to as the EA1 and EA2, respectively, in Figure 2-4. EA1 is desired for photoemission studies, and EA2 is for X-ray absorption measurement. XANES and XEOL experiments in this study were carried out at EA2 for measuring Si K-, N K-, O K- and C K-edge of various compounds.

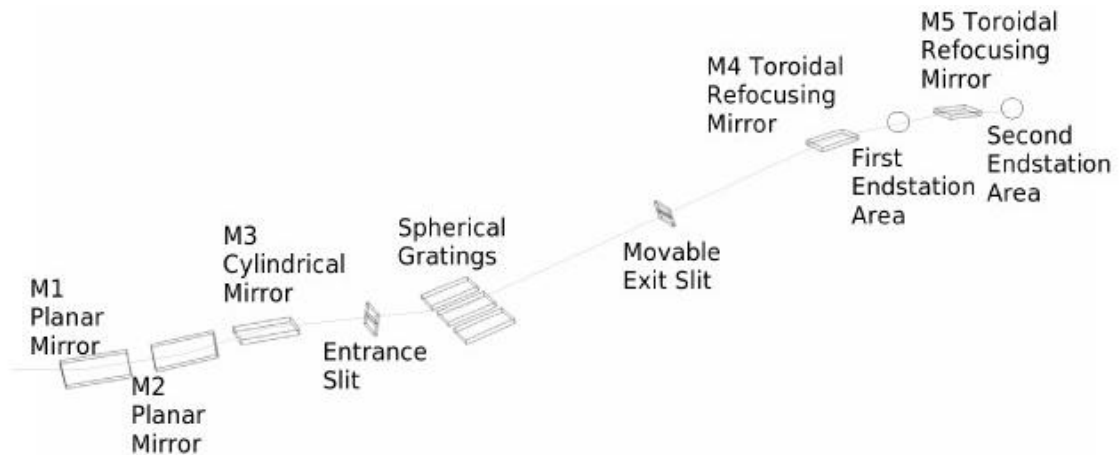


Figure 2-4 Layout of the SGM beamline [7].

2.2.3 X-ray Science Division partnered with the Pacific Northwest Consortium (PNC-XSD) Sector 20

PNC-XSD sector 20 at APS contains two beamlines, which are bending magnet (20-BM) and insertion device (20-ID), respectively. The 20-BM beamline utilizes a Si (111) double crystal monochromator providing hard X-ray of energy range 2.7-32.7 keV [8]. The energy is selected by adjusting the angles of the incidence of the beam onto the first crystal, and the second crystal rotates and translates to maintain a fixed vertical position of the exit beam. The beamline has an energy resolution ($\Delta E/E$) of 1.4×10^{-4} and the photon flux of 1×10^{11} (photons/s) at 10 keV. The beam spot size is 30 mm (horizontal) \times 1 mm (vertical). The layout of the 20-BM beamline is shown in Figure 2-5.

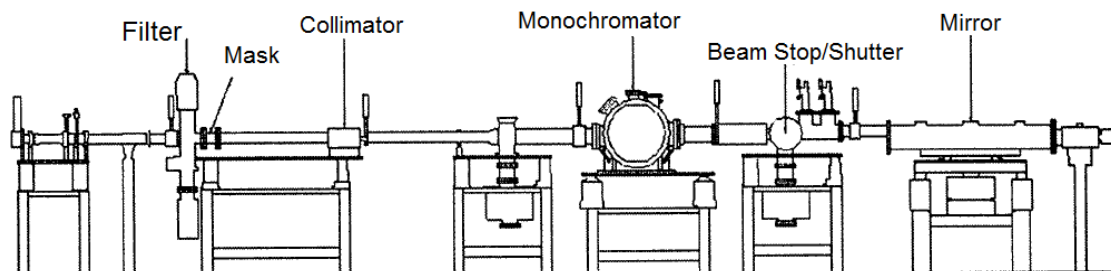


Figure 2-5 Schematic layout of the 20-BM beamline [8].

2.3 Detection Modes

XAFS can be measured in several modes as illustrated in Figure 2-6: transmission, electron yield, fluorescence yield, and in our research, luminescence (optical) yield. The transmission mode is the most straightforward one. The signals of incident photon (I_0) and transmitted photon (I) are measured by ionization chambers filled with N_2 gas located before and after the sample, respectively. The absorption coefficient μ of sample of thickness t can be obtained from the equation $I/I_0 = \exp(-\mu t)$. However, there is a certain limitation of using transmission mode for the XAFS measurement. The major concern is the sample thickness. The incident X-ray can be attenuated significantly (e.g. to $1/e$, if $t=1/\mu$), so that all photons are absorbed if the sample is too thick. If the sample is too thin (diluted sample), the absorption is not constant throughout the sample. As a result, transmission mode is ideal for measuring films (e.g. metal foils) in the hard X-ray region. For non-uniform samples, or samples require soft-X-rays, XAFS spectra are measured in the modes of total electron yield (TEY) and X-ray fluorescence yield (FY), which are based on the assumption that the yield is proportional to the absorption coefficient.

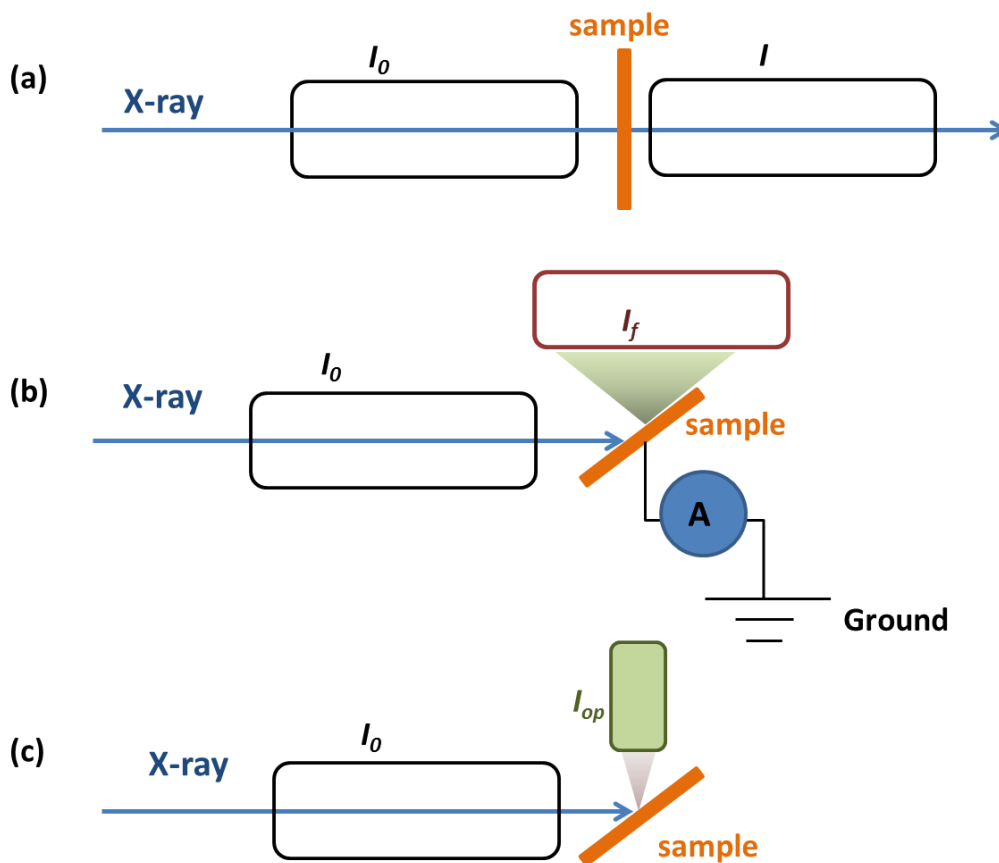


Figure 2-6 Illustration of XAFS detection modes: (a) transmission, (b) fluorescence and electron yield, (c) optical yield.

As described in Chapter 1, when a core-hole is created, an electron at a shallower level fills the core-hole while ejecting another electron via the Auger process or secondary process [9]. TEY thus measures all electrons ejected from the samples, including photoelectrons, Auger electrons and secondary electrons. Experimentally, the yield is measured by monitoring the neutralization current to ground (as shown in Figure 2-6(b)) or using an electron multiplier [10]. The TEY mode is highly surface sensitive, usually probing a sample surface of a few nm, since the electron escape depth (or inelastic mean free path, IMFP) as a function of their kinetic energy follows the universal curve, shown in Figure

2-7. It should also be noted that charging on the sample surface when it has poor electron conductivity may cause distortion in the measured yield spectra. For samples that are conducting, TEY mode is able to measure the absorption coefficient without suffering thickness effect.

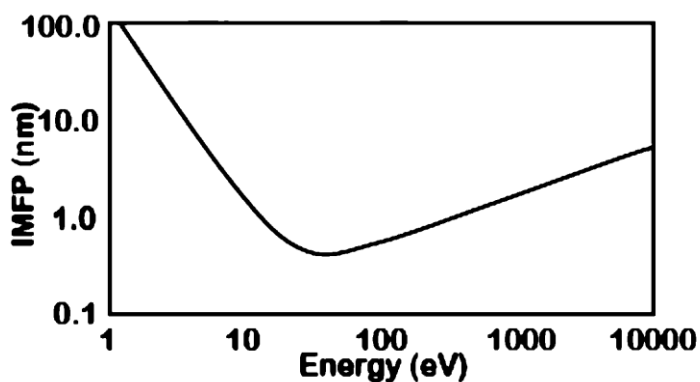


Figure 2-7 Universal curve for electron inelastic mean free path as a function of the kinetic energy

XAFS can also be measured in the mode of X-ray fluorescence yield (FY). During the decay process, X-ray fluorescence is also emitted when electrons at shallower levels fills the core-hole. Although the actual probing depth of FY depends on the photon energy and element measured, in general FY probes deeper in the sample compared to the surface sensitive TEY, thus FY is considered as “bulk” sensitive. It should also be noted that if the sample is too thick, i.e. thicker than the one absorption length (distance over which X-ray intensity decreases by a factor of $1/e$) of the emitted fluorescence, self-absorption may occur which lead to a partial (or total) inversion of the resulted FY spectra. This behavior is very common in soft X-ray spectroscopy associated with low Z elements of shallow core holes. This however, can be partially solved by using a recently

developed technique which measures the inverted partial fluorescence yield (IPFY) [11,12]. There are various detectors that have been used for monitoring the emitted X-ray fluorescence, such as channel plates, solid state detectors (e.g. multicrystal Si or Ge), or recently developed Si drift detectors.

Another detection mode, though not widely used yet, is to monitor the optical yield (PLY) from the sample following the X-ray absorption process. It is however, a powerful tool to study light-emitting materials. As mentioned in Chapter 1, upon core-hole excitation, electrons and holes may undergo thermalization, and during the electron-hole recombination near the band-gap, luminescence is produced if such recombination process is radiative. The luminescence spectrum obtained under selected excitation energy (i.e. XEOL), is collected using a charge-coupled device (CCD) detector at the wavelength range of typically 200-1000 nm, shown in Figure 2-6(c). The PLY mode is to collect XEOL spectra continuously while scanning the incident photon energy. A 2D-map is hence generated with x -axis being the excitation energy, y -axis being the wavelength of the luminescence and z -axis being the luminescence intensity.

Although listed separately in Figure 2-6, the PLY mode is usually conducted simultaneously with either transmission mode or TEY/FY mode by properly configuring the optics. During the measurement, the samples are mounted on a manipulator that can translate or rotate to the desired measuring position. For FY, the X-ray is usually set to a 45 ° incident angle and the detector is placed at 90 ° to the incident beam to minimize the elastically scattered X-ray, while for PLY (and XEOL), a set of focusing lenses is equipped between the sample and the CCD detector to get the optimal signal to noise ratio.

2.4 XAFS Calculation

Theoretical approaches for calculating XAFS spectra have been advanced significantly over the last few decades. Since the basic physics of the absorption process is reasonably well-established, the difference between the computation codes is the use of different approximations, and each has its own merit for calculating specific systems. For near-edge structure calculation, there are two types of approaches that are commonly used. One uses multiple scattering theory, such as the FEFF code [13] or the FDMNES code (the multiple scattering mode) [14], and the other one is based on band structure calculation using density functional theory (DFT), such as WIEN2k [15] and Stockholm-Berlin (StoBe) [16] software packages.

Although the detailed calculation methods differ slightly, the basic idea of the multiple scattering calculation is that, the atoms of the materials are considered as isolated free atoms forming clusters, i.e. no crystal symmetry or boundary condition is taken into account. The atomic charge densities are superimposed to create an average potential (muffin-tin potential). The phase shift caused by the outgoing wave interfering with the wave scattered by the surrounding atoms are calculated as individual scattering paths [13,17]. The multiple scattering theory has shown its advantage for calculating XAFS spectra of excitation energy well-above the threshold (i.e. EXAFS), but at the near-edge region, the calculated spectra lack fine details due to the neglecting of the band effect.

On the other hand, the WIEN2k program, used in Chapter 5, makes use of the density functional theory approach which involves solving the Kohn-Sham equations. WIEN2k is a full potential (linearized) augmented plane waves (APW) with local orbitals code that calculates the ground state electronic structure of a periodic system [15,18]. It gives

highly accurate treatment of the ground state electronic structure, including total and partial density of states, which the multiple scattering calculation is not able to produce with high quality so far. For crystalline materials with simple symmetry (e.g. tetrahedral), it is a powerful tool for calculating the near-edge region, particularly within a few eV of the threshold.

In the WIEN2k program, the unit cell is described as a basis set which consists of (1) non-overlapping atomic spheres, and (2) an interstitial region. The first part, which is within a defined nuclei radius, a linear combination of radial function times spherical harmonics is used, and the second part uses a plane wave which describes the region outside the defined radius [19]. The exchange-correlation potential can be specified using generalized gradient approximation (GGA) [20], which is integrated in the program package.

To set up a calculation, the crystal structure needs to be defined, which includes the space group, unit cell parameter, and the atomic coordination in the unit cell. The radius should also be chosen, the value of which is selected such that the neighboring atoms are almost touching. Then the number of plain waves is set for calculating the interstitial region. The XANES spectra are calculated using dipole transition. The core-hole lifetime and instrumentation broadening are also taken into account, based on the theoretical values in the literature [21].

2.5 References

- [1] <http://www.lightsource.ca/operations/machinedesign.php>
- [2] Picture courtesy of the Canadian Light Source.

http://www.lightsource.ca/experimental/images/CLS_Experimental_Hall_2011.png

[3] The Advanced Photon Source List of Parameters, compiled by H. M. Bizek, July 1996

[4] Picture courtesy of the Advanced Photon Source.

http://www.aps.anl.gov/Beamlines/Images/planview_11_3_11.jpg

[5] Hu, Y. F.; Zuin, L.; Wright, G.; Igarashi, R.; McKibben, M.; Wilson, T.; Chen, S. Y.; Johnson, T.; Maxwell, D.; Yates, B. W.; Sham, T. K.; Reininger, R., *Rev. Sci. Instrum.* 2007, 78, 083109/1-083109/5.

[6] <http://exshare.lightsource.ca/vlspgm/Pages/Specifications.aspx>, last access: Jan, 2012

[7] Regier, T.; Krochak, J.; Sham, T. K.; Hu, Y. F.; Thompson, J.; Blyth, R. I. R., *Nucl. Instrum. Methods Phys. Res., Sec. A* 2007, 582, 93-95.

[8] Heald, S. M.; Brewster, D. L.; Stern, E. A.; Kim, K. H.; Brown, F. C.; Jiang, D. T.; Crozier, E. D.; Gordon, R. A., *J. Synchrotron Radiat.* 1999, 6, 347-349.

[9] Erbil, A.; Cargill, G. S., III; Frahm, R.; Boehme, R. F., *Phys. Rev. B* 1988, 37, 2450-64.

[10] Sham, T. K.; Naftel, S. J.; Coulthard, I., *Chemical Applications of Synchrotron Radiation*. World Scientific Co., River Edge: 2002.

[11] Achkar, A. J.; Regier, T. Z.; Wadati, H.; Kim, Y. J.; Zhang, H.; Hawthorn, D. G., *Phys. Rev. B* 2011, 83, 081106.

[12] Achkar, A. J.; Regier, T. Z.; Monkman, E. J.; Shen, K. M.; Hawthorn, D. G., *Nature Scientific Reports* 2011, 1, 182.

[13] Rehr, J. J.; Albers, R. C., *Rev. Mod. Phys.* 2000, 72 (3), 621-654.

- [14] Joly, Y., *Phys. Rev. B* 2001, 63 (12), 125120.
- [15] Blaha, P.; Schwarz, K.; Sorantin, P.; Trickey, S. B., *Comput. Phys. Commun.* 1990, 59 (2), 399-415.
- [16] StoBe program: <http://www.fhi-berlin.mpg.de/KHsoftware/StoBe/index.html>
- [17] Rehr, J. J.; Mustre de Leon, J.; Zabinsky, S. I.; Albers, R. C., *J. Am. Chem. Soc.* 1999, 113 (14), 5135-5140.
- [18] Blaha, P.; Schwarz, K., *J. Phys. F* 1987, 17 (4), 899-911.
- [19] WIEN2k, An augmented plane wave plus local orbitals program for calculating crystal properties, User's guide, WIEN2k_11.1, compiled by P. Blaha, K. Schwarz, G. Madsen, D. Kvasnicka, and J. Luitz
- [20] Perdew, J. P.; Chevary, J. A.; Vosko, S. H.; Jackson, K. A.; Pederson, M. R.; Singh, D. J.; Fiolhais, C., *Phys. Rev. B* 1992, 46, 6671-87.
- [21] Fuggle, J. C.; Inglesfield, J. E., *Unoccupied Electronic States: Fundamentals for XANES, EELS, IPS and BIS*. Springer-Verlag: New York, 1992; Vol. 69.

Chapter 3

3 XANES and XPS Studies of Metal Nanoparticles Deposited SiNW

3.1 Introduction

Metal nanoparticles exhibit outstanding catalytic activities in various important redox reactions. Au nanoparticles (AuNP) are found to be good candidates for CO oxidation and partial oxidation of hydrocarbon [1-3], while Pt nanoparticles (PtNP) exhibit excellent performance in proton exchange membrane fuel cells [4]. For catalysis application, nanoparticles need to be supported on a solid surface. One of the commonly used substrates for fuel cell application is carbon black, due to its high surface area and good electrical properties compared to other bulk materials [5,6]. Recent advances in nanotechnology have also demonstrated that compared to PtNP on carbon black, carbon nanotubes and graphene supported PtNP are of much higher catalytic activity [4,6,7]. As for AuNP, metal oxide such as TiO₂ and Fe₂O₃ thin film or nanostructures are widely used for catalyst supports [1,8].

The catalytic performance can be further improved upon the formation of a bi-metal system [9,10]. Theoretical and experimental results have both demonstrated that Pt can form various alloys with other noble metals such as Ru, Pd, Rh, Au, as well as transition metals such as Ni, Fe, Co, Sn [11-13]. As one of the promising catalysts in biofuel cell applications, Pt-Au binary nanoparticles have shown improved performance in glucose

* Part of the content in this chapter has been published in *J. Phys. Conf. Series*, **2009**, 190, 012133

oxidation reactions compared to PtNP or AuNP alone [14]. It has also been reported recently that Pt-Au bimetallic nanocatalysts on graphene are of higher efficiency in methanol and formic acid fuel cells compared to PtNP-graphene or AuNP-graphene system [15,16].

There are various techniques that have been developed for nanoparticle synthesis. Wet chemical methods are usually the favored methods compared to physical techniques (e.g. vapor deposition), since the size and shape of nanoparticles can be more readily controlled by altering experimental conditions. More often, metal nanoparticles are chemically or electrochemically reduced from their ionic solutions (precursors) upon addition of reducing agent (i.e. chemical reduction) or applying an external voltage (i.e. electrochemical deposition) [17,19]. In addition, electroless chemical deposition using hydrogen-terminated Si surface as the reducing agent is a highly efficient strategy for producing metal nanoparticles coated Si surfaces. Various nanoparticles such as Cu, Ag, Au, Pt, Pd can be directly deposited onto porous Si from their ionic solutions without introducing other reducing agents [20-22]. As for Si nanowires (SiNW) as catalyst support, Ag, Au, Pd and Rh nanoparticles deposition has been reported [23,24,25].

Understanding the electronic structure of metal nanoparticles upon alloy formation and nanoparticle-substrate interface is crucial for designing catalysis devices of higher performance. It has been known that for metal nanoparticles such as Pt and Au, the *d* electrons play an important role in their catalytic properties since they can be affected by charge redistribution at metal-metal and/or metal-substrate interface [5]. X-ray absorption near-edge structure (XANES) hence is a powerful tool which directly probes metal *d* electronic states by exciting the $2p$ core electrons (i.e. the $L_{3,2}$ -edge).

Another commonly used characterization technique for metal alloys is X-ray photoelectron spectroscopy (XPS). XPS is a surface analysis technique which is capable of providing elemental composition and chemical state information on a solid surface (usually within 5~10 nm). It is an X-ray photon-in, electron-out technique, and the X-ray used for excitation is monochromatic, usually provided by the Al K_{α} or Mg K_{α} fluorescence line. The theoretical foundation of XPS technique is the photoelectric effect. The kinetic energy (E_k) of the emitted electron is measured and the atomic core level binding energy (BE) is then determined by Equation 3.1 shown below:

$$BE = h\nu - E_k - \Phi \quad (3.1)$$

where $h\nu$ is the excitation energy and Φ is the work function. The binding energy is highly sensitive to the chemical environment of the element, which is caused by the gain or loss of electrons (oxidation state). This can be observed from XPS spectrum as a binding energy peak shift of the element measured.

In this chapter, AuNP and PtNP were reductively deposited on the Si nanowire (SiNW) arrays made via electroless chemical etching. Electronic structures of nanoparticles and metal-Si interface were studied using XANES and XPS.

3.2 Experimental

3.2.1 Synthesis

N-type SiNW were synthesized using electroless chemical etching method. The synthesis detail and the morphology characterization are described in Appendix A. Briefly, phosphorous doped n-type Si wafer (500-550 μm thickness, 1-5 $\Omega\cdot\text{cm}$ resistivity) after surface impurity removal was dipped in a mixture of AgNO_3 (0.005 M) and HF (4.8 M)

solution to form a thin layer of Ag nanoparticles, and then the Si wafer was immersed in the etching solution containing 0.4 M H₂O₂ and 4.8 M HF for 30 min. The PtNP and AuNP were reductively deposited on the as-prepared SiNW: the SiNW was first treated with 5% HF for 3 min to form H-terminated surface, and then was dipped in the metal-ion contained aqueous solutions for 90 seconds under slow stirring. 5x10⁻⁴ M K₂PtCl₄ solution was used to form PtNP-coated SiNWs (denoted as Pt-SiNW), and NaAuCl₄ solution of 5x10⁻⁴ M was used to form AuNP-coated SiNWs (denoted as Au-SiNW). A mixture containing both K₂PtCl₄ (5x10⁻⁴ M) and NaAuCl₄ (5x10⁻⁴ M) was used to form bimetallic alloy nanoparticles on SiNW (denoted as Pt-Au-SiNW).

3.2.2 Characterization

The morphologies of nanoparticles deposited SiNW were characterized using scanning electron microscopy (SEM, LEO1540, Nanofabrication Laboratory at UWO) and transmission electron microscopy (TEM, Philips CM10, Biotron at UWO). Figure 3-1(a) and 1(b) show the top-view SEM images of Pt-SiNW and Au-SiNW, respectively.

Nanoparticles can be clearly seen on the surface of SiNW. Detailed morphology of SiNW after nanoparticles deposition is revealed by the TEM image. Figure 3-1(c) shows the TEM of Pt-SiNW as an example. It can be seen that the tips of the nanowire are covered by aggregated PtNP. Meanwhile, toward the middle of the nanowire, the PtNP get smaller in size and more evenly distributed.

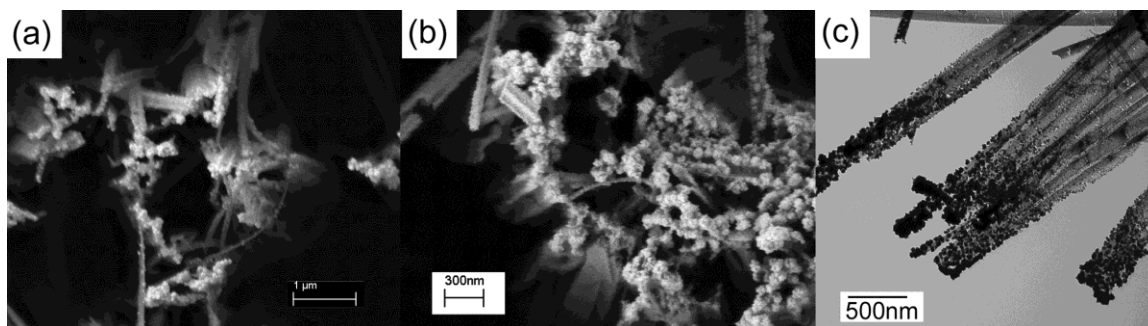


Figure 3-1 Selected SEM and TEM images of Pt and Au deposited SiNW. (a) SEM of Pt-SiNW, (b) SEM of Au-SiNW, (c) TEM of Pt-SiNW

XPS was carried out using a Kratos Axis Ultra spectrometer at Surface Science Western (SSW). A monochromatic Al K_{α} X-ray source is applied and the analysis area is $\sim 700 \mu\text{m} \times 300 \mu\text{m}$ on the surface. The work function is calibrated to give a binding energy of metallic Au $4f_{7/2}$ at 83.95 eV, and the binding energies were referenced to C $1s$ peak at 284.8 eV of the surface adventitious carbon.

XANES measurements were conducted at two beamlines providing soft X-rays and hard X-rays, respectively. Si K-edge XANES were measured at the spherical grating monochromator (SGM) beamline at Canadian Light Source (CLS) [26]. XANES were measured in the modes of total electron yield (TEY) and X-ray fluorescence yield (FY). Pt and Au L-edge XANES were measured at BM-20, PNC/XSD (X-ray Science Division partnered with the Pacific Northwest Consortium) at the Advanced Photon Source (APS), Argonne National Laboratory [27]. Au and Pt foils measured in transmission mode were used as references. Au and Pt L-edges of SiNW samples were measured in the mode of FY. All spectra are normalized to the incident photon flux.

3.3 Results and Discussion

3.3.1 XANES of Metal Deposited SiNW

We first discuss the mono-metal nanoparticles deposited samples Pt-SiNW and Au-SiNW in comparison with their bulk metal counterparts. Figure 3-2 shows the XANES spectra of metal deposited SiNW at (a) the Pt L₃-edge, (b) the Pt L₂-edge, and (c) the Au L₃-edge. The L₃-edge probes the electron transition from 2*p*_{3/2} to unoccupied 5*d*_{5/2} and 5*d*_{3/2} states. Since Pt has an unfilled 5*d*_{5/2} orbital, the spectrum displays a sharp peak (also referred to as “whiteline”) at the edge jump (Figure 3-2(a)), whereas Au has a full 5*d* band, only broad oscillations are seen at the whiteline region (Figure 3-2(c)). The oscillations beyond the whiteline arise from multiple scattering.

The spectral pattern of Pt-SiNW is similar to that of Pt foil at the Pt L₃-edge, which is a characteristic face-centered cubic (fcc) structure. A detailed comparison of the whiteline and post-whiteline features is shown in the inset of Figure 3-2(a). First, it can be seen there is a slight increase of whiteline intensity of Pt-SiNW, indicating that there is an increase of Pt 5*d* hole population (loss of 5*d* electrons). The increase of Pt 5*d* holes could be due to multiple reasons: e.g. increase of surface atoms upon nanoparticles formation, or charge redistribution between Pt and Si substrate. The formation of nanoparticles usually leads to a *d* charge depletion due to rehybridization, which has been observed from Pt deposited porous Si [20]. The inset of Figure 3-2(a) also clearly shows that the post whiteline peaks of Pt-SiNW is significantly broadened compared to those of Pt foil, indicating that Pt in Pt-SiNW is lack of long-range order, which confirms the formation of small Pt clusters.

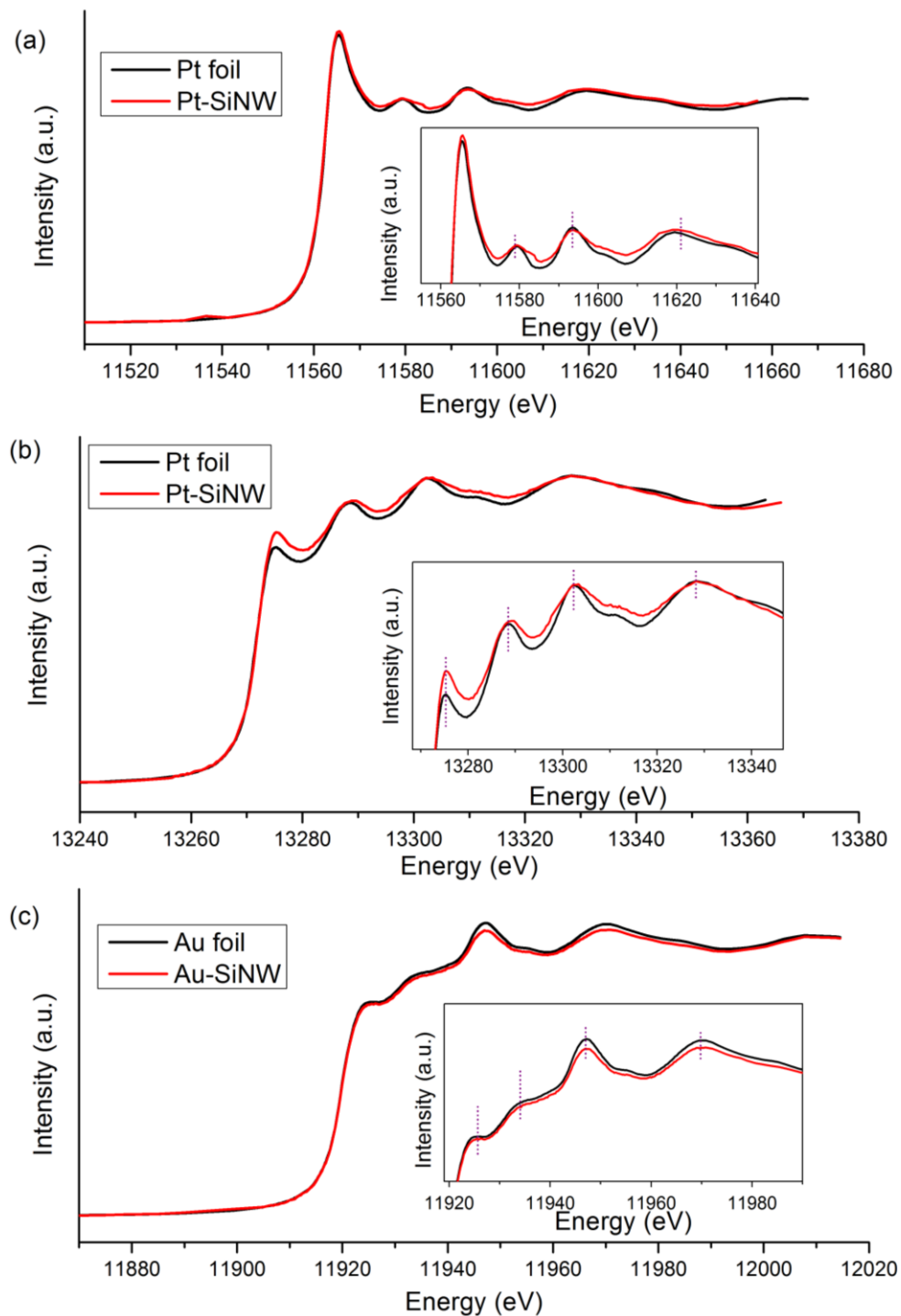


Figure 3-2 XANES of Pt-SiNW and Au-SiNW at (a) the Pt L_3 -edge, (b) the Pt L_2 -edge, and (c) the Au L_3 -edge. The spectra are normalized to unit edge jump. The insets show the magnified white line region.

At the Pt L_2 -edge, the Pt $2p_{1/2}$ core electrons are excited, hence XANES selectively probes the unoccupied Pt $5d_{3/2}$ state. Unlike the sharp whiteness seen in L_3 -edge XANES, there is no sharp feature at the Pt L_2 -edge due to its filled $5d_{3/2}$ band (Figure 3-2(b)). The XANES of Pt foil only exhibits broad oscillations above the edge. Upon the formation of PtNP, Pt-SiNW shows an increase in whiteness intensity compared to Pt foil. The redistribution of Pt $5d$ holes clearly has a stronger effect on the L_2 -edge XANES, and Pt loses more $5d_{3/2}$ charge than $5d_{5/2}$ charge upon deposition on Si. On the other hand, oscillation peak broadening of Pt-SiNW relative to Pt foil can also be seen at the L_2 -edge, which is in accord with the observation of the L_3 -edge XANES.

XANES of Au-SiNW exhibit similar resonance patterns as that of Au foil at the Au L_3 -edge, shown in Figure 3-2(c). The as-formed AuNP are of the fcc crystal structure [28]. Only subtle difference is seen when comparing Au-SiNW with Au foil. The whiteness intensity exhibits a slight decrease in XANES of Au-SiNW. A similar observation has been reported on AuNP deposition on porous Si [28]. Unlike Pt, atomic Au has filled $5d$ band, so the observed whiteness is due to the rehybridization between Au d and sp band above the Fermi level, which occurs preferentially in bulk Au. Upon the formation of small Au clusters, Au is more atomic-like, hence the rehybridization is less efficient, resulting a decrease in $5d$ hole count (decrease in whiteness intensity). It should also be noted that in previously reported XANES measurements on alkanethiolate-capped AuNP, an increase in Au L_3 -edge whiteness was observed, which is due to the interaction between Au and S-contained capping molecule [29]. As a result, we should also take into account of the metal nanoparticle-Si substrate interaction, which will be discussed shortly.

XANES of PtNP and AuNP co-deposited SiNW was first examined at the Pt L₃- and L₂-edge, shown in Figure 3-3. The spectra are plotted in the way that the L₃- and L₂-XANES are aligned to the absorption threshold (E_0), so that the x -axis is $\Delta E = E - E_0$. The area under the difference curve between L₃-XANES and L₂-XANES thus reflects the number of 5*d* holes in Pt. It can be clearly seen that upon the co-deposition, there is a decrease in Pt 5*d* hole population, indicating that Pt gains electrons from Au. More interestingly, when comparing the post-edge features between Pt foil and Pt-Au-SiNW, the latter exhibits a progressive mismatch of the oscillation peaks, in which the peaks are getting closer to each other toward the higher excitation energy. Since the post-edge features in XANES are due to multiple scattering from neighboring atoms, the observed mismatch qualitatively indicates that the inter-atomic distance of Pt increases in Pt-Au-SiNW. This observation indicates that Au and Pt form an alloy in the nanoparticles; in other words, not as monocomponent nanoparticles or core-shell nanoparticles. Similar mismatches with an opposite trend should also be seen at the Au L₃-edge (see below). This is expected since Au and Pt, being adjacent noble metal elements on the periodic table, have very similar backscattering amplitudes.

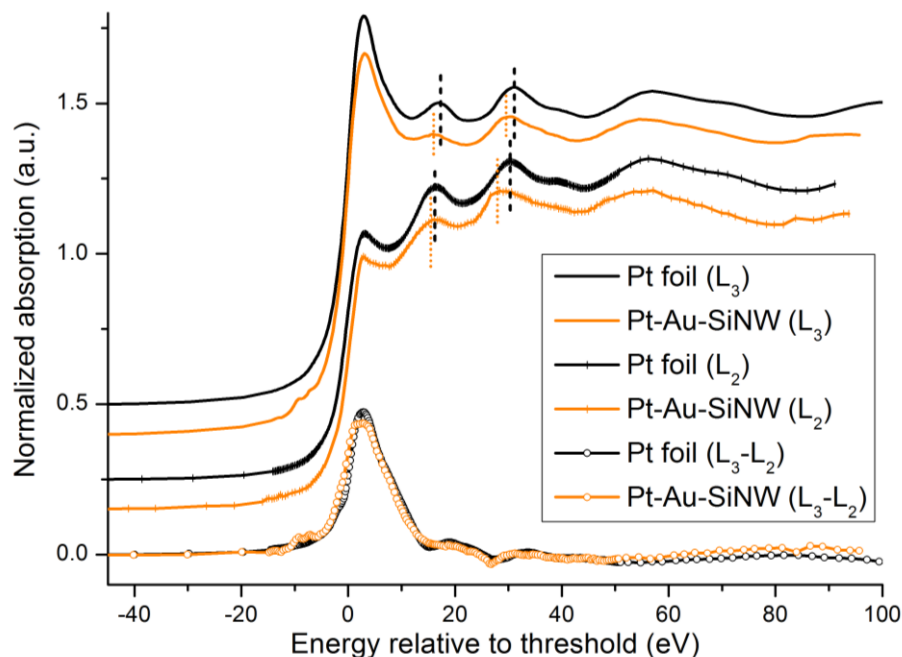


Figure 3-3 XANES of Pt-Au-SiNW obtained at the Pt L_3 - and L_2 -edge in comparison with Pt foil. The difference curves are done by subtracting XANES of L_2 from L_3 for Pt foil and Pt-Au-SiNW, respectively.

A similar mismatch is indeed observed from the Au perspective. Shown in Figure 3-4, the post-edge oscillations in the Au L_3 -edge XANES of Pt-Au-SiNW are getting further apart from each other as the excitation energy increases. In contrast to Pt, the inter-atomic distance of Au decreases once Au is co-deposited with Pt. The expansion of Pt lattice and contraction of Au lattice in the alloy nanoparticles is expected from Vegard's law, since the lattice constant for Au is larger than Pt. On the other hand, it should be noted that the whiteline of Pt-Au-SiNW is much higher than the one of Au foil, which further confirms the charge redistribution process takes place during which Au loses d charge while Pt gains d charge.

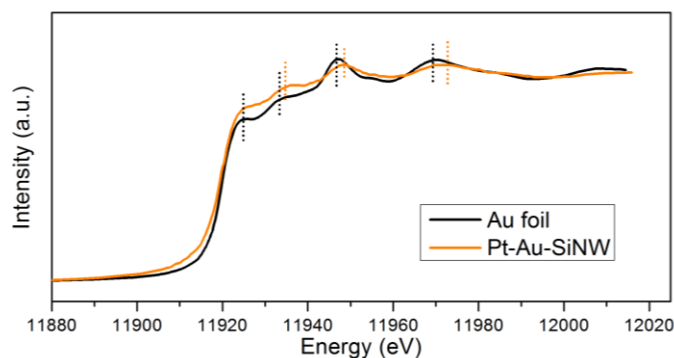


Figure 3-4 Au L₃-edge XANES of Pt-Au-SiNW in comparison with Au foil.

We then take a look at the electronic structure from the Si perspective before and after metal deposition. Shown in Figure 3-5, the Si K-edge XANES of the as-prepared SiNW and metal deposited SiNW are recorded in TEY (a) and FY (b), respectively. The spectra are normalized to unit edge jump and shifted vertically for clarity. It should be noted that TEY probes sample surfaces within 1~2 nm, while FY is dominated by the contribution from the bulk (i.e. SiNW) since it has a deeper probing depth (a few microns). The TEY-XANES of all SiNW samples exhibit several characteristic features of Si and its oxide, which are labeled as A, B, and C in the figure. Peak A is originated from the Si 1s to 3p transition of elemental Si (Si⁰), and peak C is the whiteline of fully oxidized Si (i.e. SiO₂). Peak B is attributed to Si oxide of intermediate state (suboxide, SiO_x, 0 < x < 2) [30]. In FY spectra, the Si⁰ features dominate in all samples, since the major contribution is from the SiNW array.

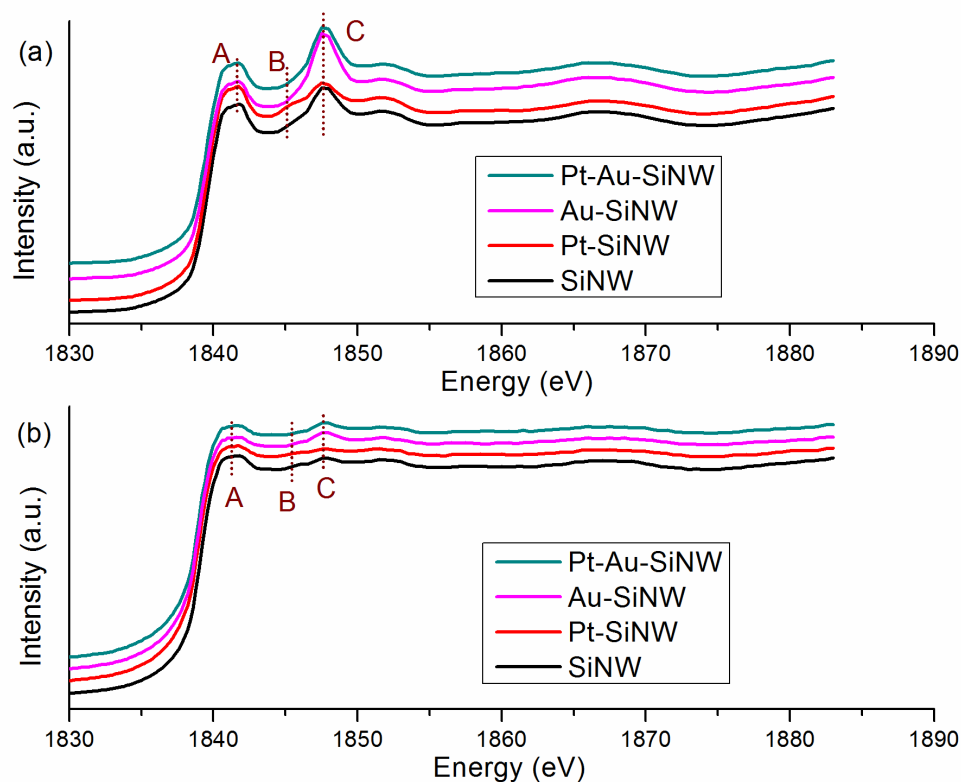


Figure 3-5 Si K-edge XANES of SiNW before and after metal deposition. (a) TEY, (b) FY.

The amount of oxide on the surface can be semi-quantified by comparing the edge jump ratio between Si^0 (peak A) and Si^{4+} (peak C) from the TEY-XANES (Figure 3-5(a)). The as-prepared SiNW shows both Si and SiO_2 contributions. Weak but distinguishable resonance at region B indicates the presence of suboxide at the Si/ SiO_2 interface. The presence of surface oxide on SiNW is due to air exposure (native oxide). After AuNP deposition, the oxide peak C increases significantly, which is not surprising since the reduction of Au^{3+} to Au^0 leads to the surface oxidation of Si into SiO_2 [23]. However, upon PtNP deposition, the intensity of peak C decreases, while peak B exhibits a noticeable increase in intensity, indicating that part of the SiO_2 is reduced to SiO_x . Recall

the L-edge XANES of Pt and Au (Figure 3-2), where the Pt $5d$ holes ($5d_{3/2}$ in particular) increases upon interaction with SiNW, while Au shows only subtle changes. This is in agreement with the observed Si K-edge XANES: Pt tends to have a stronger interaction with the Si substrate than Au does, and Pt donates its d charge to the substrate which results in a partial reduction of SiO_2 into SiO_x . On the other hand, Au is more electronegative, so it is less likely for electron transfer from Au to Si to take place. In the PtNP and AuNP co-deposited sample, a surface oxide peak is also seen, but the intensity is less than the one of Au-SiNW.

3.3.2 XPS of Metal Deposited SiNW

To further examine the charge redistribution process upon metal nanoparticle deposition on SiNW, XPS measurements were also performed on metal $4f$ states as well as Si $2p$ states. Figure 3-6 shows the Pt and Au $4f$ XPS spectra of metal deposited SiNW in comparison with bulk metals. We first discuss the mono-metal deposited samples. In Figure 3-6(a), the Pt-SiNW exhibit two asymmetric peaks at binding energies of 71.2 eV and 74.5 eV, which correspond to the Pt $4f_{5/2}$ and $4f_{3/2}$ core levels, respectively. Compared to the $4f$ XPS of bulk Pt, the Pt-SiNW $4f$ peaks show slight energy shift: the peak positions of Pt-SiNW appear at binding energies ~ 0.1 eV higher than the ones of bulk Pt. Similarly, when comparing the Au $4f_{5/2}$ and $4f_{3/2}$ features of Au-SiNW with the ones of pure Au, a higher binding energy shift can also be observed in Au-SiNW, as shown in Figure 3-6(c). The Au $4f_{7/2}$ and $4f_{5/2}$ peaks of Au-SiNW locate at 84.1 eV and 87.6 eV, which are at binding energies ~ 0.1 eV higher than bulk Au.

The higher binding energy shift usually indicates an increase in the oxidation states. For Pt-SiNW, it could be due to a loss of Pt d charge which effects the $4f$ states upon

Coulomb interaction (the $F(5d,4f)$ integral) [20,28]. If we recall the XANES results discussed before, the d -charge loss of Pt in Pt-SiNW is suggested by (1) Pt $L_{3,2}$ -edge XANES as an increase of whiteline intensity, and (2) Si K-edge XANES as SiO_2 is partially reduced to SiO_x . However, for Au-SiNW, since no significant charge transfer between Au and Si is observed from the XANES results, the d -charge has little contribution to the binding energy shift observed in XPS of Au-SiNW. Previous studies have shown that the Au $4f$ binding energy increases as the Au cluster size decreases [28,31]. The binding energy increase in this case is likely due to the formation of small nanoparticle clusters (size effect).

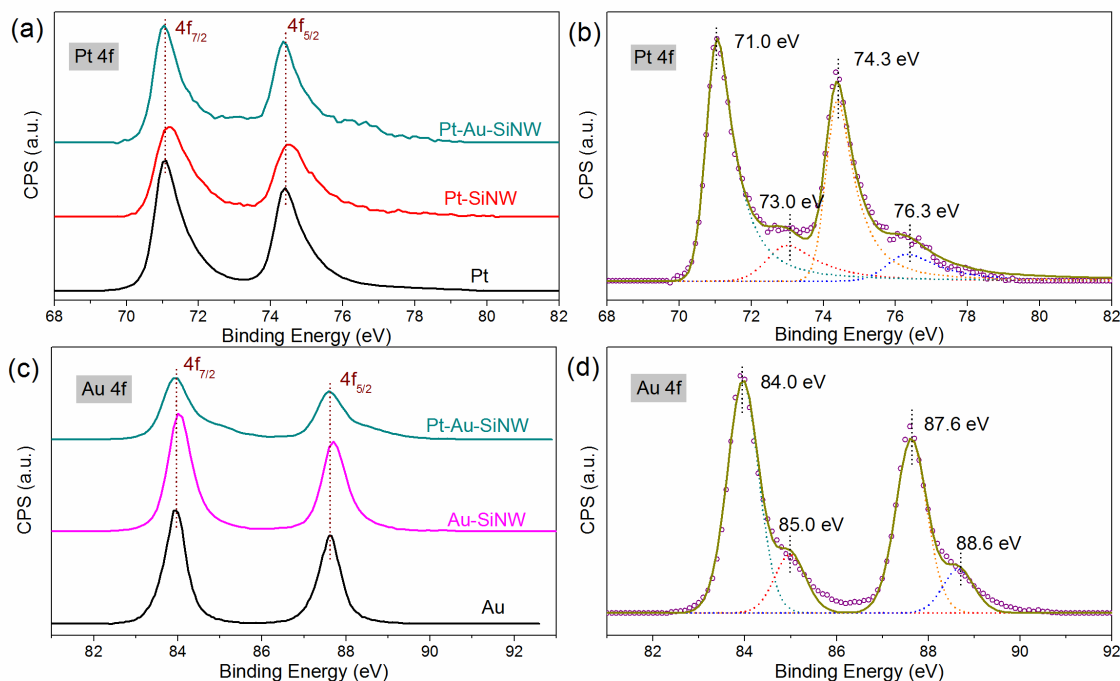


Figure 3-6 XPS spectra of Pt and Au deposited SiNW. (a) Pt $4f$ XPS of Pt-SiNW, Pt-Au-SiNW and bulk Pt, (b) peak fittings of Pt-Au-SiNW at Pt $4f$, (c) Au $4f$ XPS of Au-SiNW, Pt-Au-SiNW and bulk Au, (d) peak fittings of Pt-Au-SiNW at Au $4f$

We then turn to discuss the Pt-Au-SiNW. Interestingly, in both Pt 4*f* and Au 4*f* XPS spectra, Pt-Au-SiNW shows two main peaks of binding energies similar to the bulk metals, but there is a distinguishable shoulder-like feature at higher binding energy side next to each main peak. Shown in Figure 3-6(b) and 3-6(d), each spectrum of Pt-Au-SiNW contains four components. At the Pt 4*f* region, the two shoulder features can be fitted with two peaks at binding energies of 73.0 eV and 76.3 eV, which are about 2 eV apart from the main peaks. At the Au 4*f* region, the peak fitting results shows that Au 4*f*_{7/2} peak consists of two peaks at 84.0 eV and 85.0 eV, and the Au 4*f*_{5/2} peak has two components at 87.6 eV and 88.6 eV, respectively.

While in the metal L-edge XANES shown in Figures 3-3 and 3-4 suggest the formation of Pt-Au alloy, the XPS shows that part of nanoparticles still remain as mono-component PtNP and AuNP, and only the shoulder features are originated from the Pt-Au alloy. For both Pt and Au, the alloy formation results in an increase of binding energy relative to pure metals. From the metal L-edge XANES measurements, we know that Pt gains *d* charge while Au loses *d* charge upon alloy formation. The loss of Au *d* charge is consistent with the higher binding energy shift observed in XPS (Figure 3-6(d)). As for Pt, although it gains *d* charge, the charge redistribution between Pt and Si still takes place, since the Si K-edge XANES show that the surface SiO₂ is partially reduced to SiO_x (Figure 3-5). This gives an overall charge loss in Pt, resulting in the appearance of the high binding energy shoulder feature.

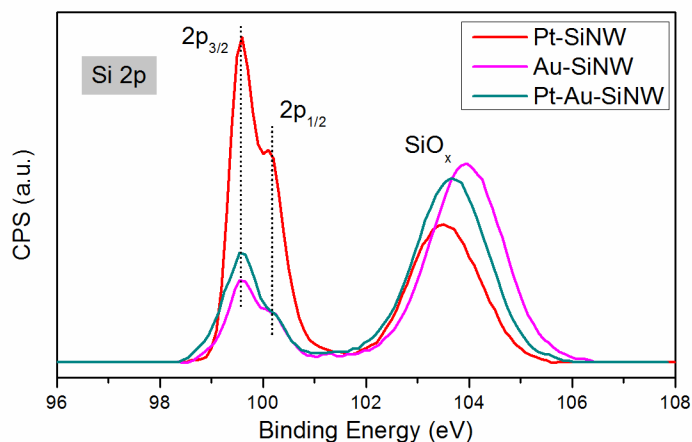


Figure 3-7 Si 2p XPS spectra of Pt-SiNW, Au-SiNW and Pt-Au-SiNW

Lastly, Si 2p XPS were also examined on the SiNW after metal deposition, shown in Figure 3-7. The XPS spectra of metal deposited SiNW show features at two energy regions: (1) a doublet with main peak at 99.6 eV and a shoulder at 100.1 eV, is from the $2p_{3/2}$ and $2p_{1/2}$ of elemental Si; (2) the broad resonance peak at binding energy ~ 103 eV belongs to the Si oxide. It can be seen that the oxide peaks appear at slightly different energies, among which Pt-SiNW is at the lowest binding energy, followed by Pt-Au-SiNW, and Au-SiNW is at the highest energy. Meanwhile, the peak ratio between elemental Si and oxidized Si are also different: the elemental Si peak is considerably higher in Pt-SiNW than the other two, and Au-SiNW has the most intense oxide peak. Such an observation indicates there is a redox reaction occurring between metal and Si/SiO₂ during the deposition. Upon PtNP deposition, part of the SiO₂ on the surface is reduced to Si and Si suboxide, however, the reduction of SiO₂ does not occur during the AuNP deposition.

3.4 Conclusion

PtNP and AuNP were reductively deposited onto SiNW and examined using XANES and XPS. Pt and Au exhibit different charge redistribution behaviors when brought into contact with Si. Pt donates its electrons to Si, resulting in a partial surface reduction of SiNW from SiO₂ to SiO_x, while no significant interaction between Au and SiNW was observed. When metallic Pt and Au are reduced from their ionic solution mixture, not only mono-component PtNP and AuNP are formed individually, but also Pt-Au alloy nanoparticles. The alloy formation results in an expansion of the Pt lattice and contraction of Au lattice. Au loses its *d* charge to Pt. Pt gains *d* charge but donates its *f* charge to Si, resulting in an overall charge loss at the Pt site.

3.5 References

- [1] Valden, M.; Lai, X.; Goodman, D. W., *Science* **1998**, *281*, 1647-1650.
- [2] Stephen, A.; Hashmi, K.; Hutchings, G. J., *Angew. Chem. Int. Ed.* **2006**, *45*, 7896-7936.
- [3] Hughes, M. D.; Xu, Y. J.; Jenkins, P.; McMorn, P.; Landon, P.; Enache, D. I.; Carley, A. F.; Attard, G. A.; Hutchings, G. J.; King, F.; Stitt, E. H.; Johnston, P.; Griffin, K.; Kiely, C. J., *Nature* **2005**, *437*, 1132-1135.
- [4] Zhang, J., *PEM fuel cell electrocatalysts and catalyst layers: fundamentals and applications*. Springer-Verlag: London, 2008.
- [5] Antolini, E., *J. Mater. Sci.* **2003**, *38*, 2995-3005.
- [6] Antolini, E., *Appl. Catalysis B* **2009**, *88*, 1-24.
- [7] Seger, B.; Kamat, P. V., *J. Phys. Chem. C* **2009**, *113*, 7990-7995.

- [8] Haruta, M., *Catalysis Today* **1997**, *36*, 153-166.
- [9] Lim, B.; Jiang, M.; Camargo, P. H. C.; Cho, E. C.; Tao, J.; Lu, X.; Zhu, Y.; Xia, Y., *Science* **2009**, *324*, 1302-1305.
- [10] Rice, C.; Ha, S.; Masel, R. I.; Wieckowski, A., *J. Power Sources* **2003**, *115*, 229-235.
- [11] Stamenkovic, V. R.; Mun, B. S.; Arenz, M.; Mayrhofer, K. J. J.; Lucas, C. A.; Wang, G.; Ross, P. N.; Markovic, N. M., *Nature Mater.* **2007**, *6*, 241-247.
- [12] Markovic, N. M.; Radmilovic, V.; Ross, P. N., *Catalysis and Electrocatalysis at Nanoparticle Surfaces*. Marcel Dekker: New York, Basel, 2003.
- [13] Toda, T.; Igarashi, H.; Uchida, H.; Watanabe, M., *J. Electrochem. Soc.* **1999**, *146*, 3750-3756.
- [14] Habrioux, A.; Servat, K.; Kokoh, B.; Alonso-Vante, N., Au-Pt nanomaterials and enzymatic catalysts for biofuel cell application. In *Mixed Metal Nanomaterials*, Kumar, C. S. S. R., Ed. Wiley-VCH: Weinheim, 2010; Vol. 3.
- [15] Hu, Y.; Zhang, H.; Wu, P.; Zhang, H.; Zhou, B.; Cai, C., *Phys. Chem. Chem. Phys.* **2011**, *13*, 4083-4094.
- [16] Rao, C. V.; Cabrera, C. R.; Ishikawa, Y., *J. Phys. Chem. C* **2011**, *115*, 21963-21970.
- [17] Brust, M.; Walker, M.; Bethell, D.; Schiffrin, D. J.; Whyman, R., *J. Chem. Soc., Chem. Commun.* **1994**, 801-802.
- [18] Sun, Y.; Xia, Y., *Science* **2002**, *298*, 2176-2179.
- [19] Reetz, M. T.; Helbig, W., *J. Am. Chem. Soc.* **1994**, *116*, 7401-7402.
- [20] Coulthard, I.; Sham, T. K., *Solid State Commun.* **1998**, *105*, 751-754.

- [21] Sham, T. K.; Coulthard, I.; Lorimer, J. W.; Hiraya, A.; Watanabe, M., *Chem. Mater.* **1994**, *6*, 2085-2091.
- [22] Coulthard, I.; Jiang, D. T.; Lorimer, J. W.; Sham, T. K.; Feng, X. H., *Langmuir* **1993**, *9*, 3441-3445.
- [23] Sun, X. H.; Sammynaiken, R.; Naftel, S. J.; Tang, Y. H.; Zhang, P.; Kim, P. S. G.; Sham, T. K.; Fan, X. H.; Zhang, Y. F.; Lee, C. S.; Lee, S. T.; Wong, N. B.; Hu, Y. F.; Tan, K. H., *Chem. Mater.* **2002**, *14*, 2519-2526.
- [24] Zhang, P.; Zhou, X.; Tang, Y. H.; Sham, T. K., *Langmuir* **2005**, *21*, 8502-8508.
- [25] Sun, X. H.; Wong, N. B.; Li, C. P.; Lee, S. T.; Kim, P. S. G.; Sham, T. K., *Chem. Mater.* **2004**, *16*, 1143-1152.
- [26] Regier, T.; Krochak, J.; Sham, T. K.; Hu, Y. F.; Thompson, J.; Blyth, R. I. R., *Nucl. Instrum. Methods Phys. Res., Sec. A* **2007**, *582*, 93-95.
- [27] Heald, S. M.; Brewster, D. L.; Stern, E. A.; Kim, K. H.; Brown, F. C.; Jiang, D. T.; Crozier, E. D.; Gordon, R. A., *J. Synchrotron Radiat.* **1999**, *6*, 347-349.
- [28] Coulthard, I.; Degen, S.; Zhu, Y. J.; Sham, T. K., *Can. J. Chem.* **1998**, *76*, 1707-1716.
- [29] Zhang, P.; Sham, T. K., *Phys. Rev. Lett.* **2003**, *90*, 245502.
- [30] Sham, T. K.; Naftel, S. J.; Kim, P. S. G.; Sammynaiken, R.; Tang, Y. H.; Coulthard, I.; Moewes, A.; Freeland, J. W.; Hu, Y. F.; Lee, S. T., *Phys. Rev. B* **2004**, *70*, 045313.
- [31] Mycroft, J.; Bancroft, G. M.; McIntyre, N. S.; Lorimer, J. W., *Geochim. Cosmochim. Acta* **1995**, *59*, 3351-3365.

Chapter 4

4 The Effect of Thermal Oxidation On the Luminescence Properties of Nanostructured Silicon

4.1 Introduction

The optical properties of low-dimensional silicon nanostructures have attracted extensive interest since the discovery of photoluminescence (PL) from porous Si [1,2]. As an indirect band gap semiconductor, Si does not emit visible light unless its size is reduced to a significantly small scale (i.e. less than 10 nm) by which the effect of quantum confinement becomes significant. Various experiments have been carried out over the years to study the luminescence mechanism of low-dimensional Si. In silicon quantum dots, the dominant PL is the radiative recombination of electrons and holes via excitonic transition, which is highly predicable theoretically by band-gap calculation [3-5].

Experimentally, solution based quantum dots with controllable size distribution have been successfully synthesized, the PL of which can be tuned from red to deep purple as a function of the quantum dot size [6,7]. However, luminescence mechanism of solid-state nano Si, such as porous Si (PS) and Si nanowires (SiNW), is more complex, since the surface of such Si nanostructures is usually mixed with oxide formed either during synthesis (thermal oxide or anodic oxide) or by exposure to air or moisture (native oxide). Although SiO₂ has a wide band-gap (~9 eV), it has been known as a promising light emitting material in both amorphous and crystalline forms due to its rich defect centers.[8-10] Such SiO₂-Si mixed structures exhibit luminescence at many different

* A version of this chapter has been published in *Small*, 2012, DOI: 10.1002/sml.201200175

wavelengths from ultraviolet (UV) to orange-red due to the presence of encapsulated quantum confined Si crystallites, surface states, defects in oxide and suboxide (usually formed at the interface). The luminescence intensity observed from oxide-contained nano Si is often of several orders of magnitude higher than that from purely quantum confined Si.

The most commonly observed luminescence involving oxide is located at 460 nm, which has been attributed to oxygen vacancies of SiO₂ [11]. Luminescence is also observed at shorter wavelength (e.g. 300 nm) and longer wavelength (e.g. 530-700 nm) from various Si-based nanostructures such as SiNW, Si-SiO₂ core-shell nanowires and SiO₂ nanowires, but emission bands reported in the literature are of great divergence due to the complexity of the Si-SiO₂ interface [12,13]. The oxidation of Si is a complex process in which different oxidation techniques and experimental conditions result in SiO₂ and the co-existing suboxides of various structures and morphologies. For example, PS having different light emitting properties under ambient oxidation and AgNO₃ oxidation has been reported [14]. The formation of thermal oxide usually requires temperature as high as 1000 °C to obtain fully oxidized Si. Until now, few systematic studies have been done on the oxidation of nanosized Si at relatively mild temperature, and the mechanism of luminescence involving nanostructured Si-SiO₂ composite is still unclear.

In this chapter, thermal oxidation was performed on a series of Si nanostructures. PS, SiNW and porous SiNW were oxidized under moderate and high temperatures. Their electronic structures and corresponding luminescence were comparatively studied using XANES and XEOL.

4.2 Experimental

SiNW and porous SiNW were synthesized following a metal assisted electroless chemical etching. The detailed synthesis process is described in Appendix A. Boron-doped Si wafers of (100) orientation were used: one has the resistivity of 3-10 $\Omega\cdot\text{cm}$ (lightly doped) to produce regular SiNW, and the other one has the resistivity of 0.005-0.025 $\Omega\cdot\text{cm}$ (heavily doped) to produce porous SiNW. PS was synthesized electrochemically using a two-electrode configuration [1]. A p-type (boron-doped, 3-10 $\Omega\cdot\text{cm}$) Si (100) wafer was etched in a 1:1 mixture of 48% hydrofluoric acid and absolute ethanol, under an applied current density of 100 mA/cm^2 for 20 minutes. The as-prepared SiNW and PS were then thermally oxidized in air at 800 $^{\circ}\text{C}$ for 2 hours. Two lightly doped SiNW were oxidized at 1000 $^{\circ}\text{C}$ for 2 hours and 6 hours in air, respectively, in order to form thicker oxide layers. The denotation of the samples can be found in Table 4-1.

Table 4-1: Denotation of SiNW and porous Si

Sample Description	Denotation
As-prepared regular SiNW	SiNW-r
As-prepared porous SiNW	SiNW-p
Regular SiNW, 800 $^{\circ}\text{C}$ oxidized	SiNW-r-800
Porous SiNW, 800 $^{\circ}\text{C}$ oxidized	SiNW-p-800
Regular SiNW, 1000 $^{\circ}\text{C}$ oxidized, 2hr	SiNW-r-1000
Regular SiNW, 1000 $^{\circ}\text{C}$ oxidized, 6hr	SiO ₂ nw
As-prepared porous Si	PS
Porous Si, 800 $^{\circ}\text{C}$ oxidized	PS-800

Synchrotron measurements were conducted at variable line spacing plane grating monochromator (VLS-PGM) beamline and spherical grating monochromator beamline

(SGM) at the Canadian Light Source (CLS) [15,16]. Si $L_{3,2}$ -, K-edge and O K-edge XANES and XEOL were measured. XANES spectra were collected in total electron yield (TEY) and X-ray fluorescence yield (FY). XEOL spectra were obtained while tuning the excitation photon energy from below to above the absorption edge. All spectra are normalized to incident photon flux.

4.3 Results and Discussion

4.3.1 XANES of Nanostructured Si Before and After Oxidation

Figure 4-1 compares the Si K-edge XANES of SiNW and PS before and after oxidation. Si K-edge XANES probes transition of Si $1s$ to the unoccupied $3p$ states, and elemental Si and oxidized Si can be distinguished by the energy of edge jump, marked by vertical lines in the figure. It can be seen from TEY (Figure 4-1(a)) that the XANES of the as-prepared SiNW-r and SiNW-p show only elemental Si contribution, characterized by the edge jump at 1840 eV [17]. PS however, has a more complicated surface structure. The TEY is composed of (a) elemental Si, which is the same as in the SiNW-r and SiNW-p, (b) SiO_2 , characterized by the whiteline at 1848 eV, and (c) suboxide SiO_x ($0 < x < 2$), appeared as weak resonances between Si and SiO_2 features. These spectral features are in good accord with previous observation, i.e. Si with a large surface area (as in the case of PS) can get oxidized more readily even by exposure in air or moisture [18]. The FY XANES in Figure 4-1(b) also shows that the three as-prepared samples are dominated by Si, and the ratio of SiO_2/Si also decreases in PS since FY contains more contribution from the bulk.

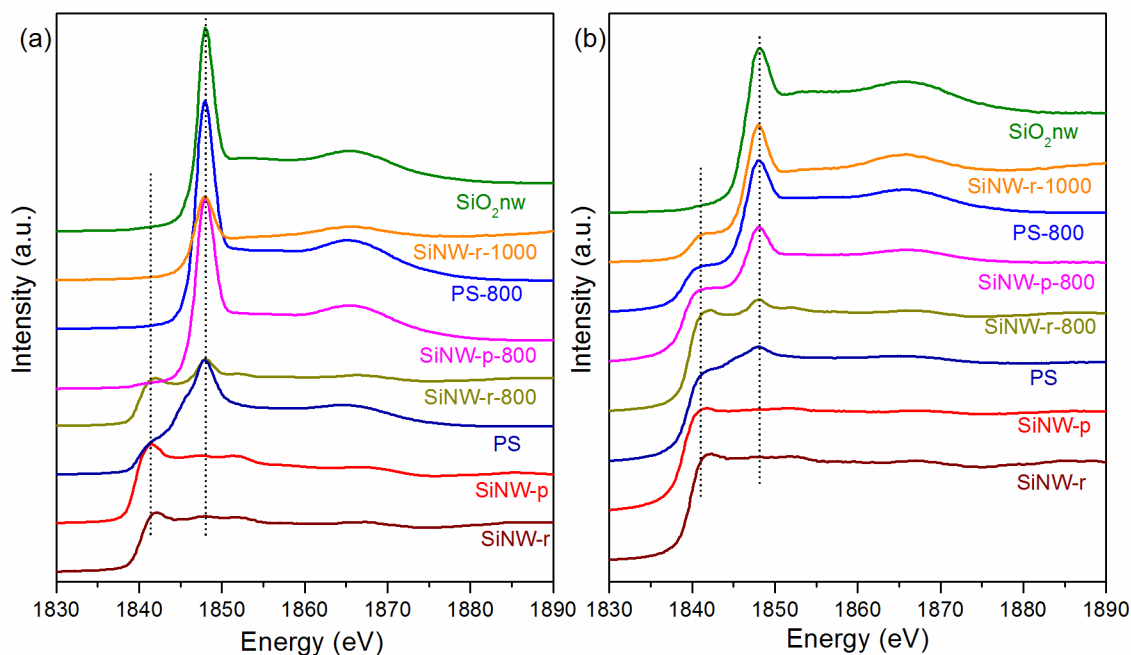


Figure 4-1 Si K-edge XANES of SiNW and PS samples before and after oxidation in (a) TEY and (b) FY.

The TEY-XANES of all the oxidized Si in Figure 4-1(a) show only SiO₂ contribution, i.e. the sharp 1848 eV whiteline, except for SiNW-r-800, in which elemental Si contribution is dominant. The relative thickness of the oxide layer can be determined by comparing the edge jump ratio of SiO₂:Si from FY-XANES (Figure 4-1(b)). For samples oxidized at 800 °C, the SiO₂:Si ratio is the highest in PS-800 (~1.1), followed by SiNW-p-800 (~0.4), and only ~0.1 in SiNW-r-800. Hence regular SiNW-r is more resistant to thermal oxidation compared to the porous SiNW-p. For SiNW-r, only after oxidation under a much higher temperature, a significant increase in SiO₂:Si edge jump ratio can be seen, and after oxidation at 1000 °C for 6 hours, SiNW-r is fully oxidized, showing no elemental Si signal in either TEY or FY.

4.3.2 Luminescence From Oxidized SiNW and PS

It is well known that light-emitting Si has to either have size small enough for quantum confinement or contain oxide. In this case, SiNW made using electroless chemical etching are relatively large in diameter (~ 100 nm), and the HF-contained etchant solution leaves SiNW surface free of SiO_2 , hence no luminescence is expected nor detected from the as-prepared SiNW-r and SiNW-p. PS, on the other hand, emits weak orange luminescence upon X-ray excitation. Shown in Figure 4-2, with the excitation energy of 1900 eV (above Si K-edge), the XEOL spectrum of PS shows a broad peak centered at 645 nm. The Si K-edge TEY (Figure 4-1(a)) as noted above, shows that the surface of PS has a complex structure, which is composed of Si and its oxide of various oxidation states (+1 to +4). The luminescence spectrum is consistent with previous observation in which the luminescence is attributed to the presence of a significant Si-SiO₂ interface [19]. The luminescence from PS has been extensively studied before [14,18], hence in the following the luminescence property of PS will be discussed in connection with the oxidized SiNW.

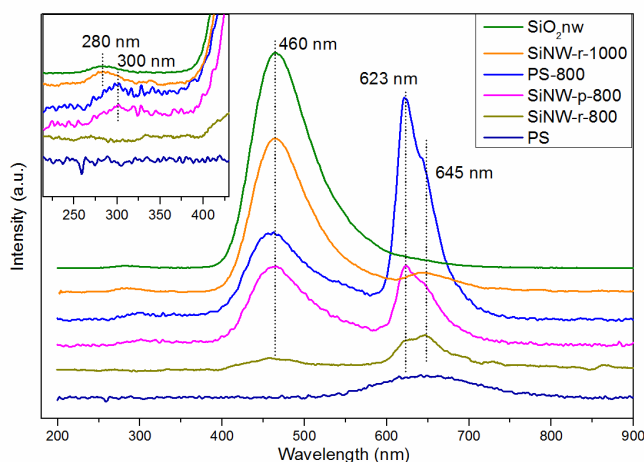


Figure 4-2 XEOL of SiNW and PS with excitation energy at 1900 eV.

Upon thermal oxidation, bright luminescence is seen from both SiNW and PS. Shown in Figure 4-2, the XEOL spectra are obtained under excitation energy of 1900 eV and normalized to the incident photon flux. All thermally oxidized Si samples have much higher luminescence intensity than that of the as-prepared PS. Although the absolute intensity of luminescence is affected by multiple factors (e.g. the amount of samples being excited by X-ray), it is still valid to compare the relative XEOL intensities among samples, since the size of the beam is constant and the attenuation length of 1900 eV photon in Si is on the order of μm (close to total absorption) [20]. The XEOL spectra of all the oxidized samples show some fine spectroscopic features which fall in three regions: (1) visible blue light centered at 460 nm, (2) orange light at 600-700 nm, and (3) if we take a close look at the shorter wavelength region, a weak UV emission peak at ~ 300 nm (inset of Figure 4-2).

The relative intensity between different emission regions (branching ratio) also varies. For example, samples oxidized under moderate temperature (800 °C), such as SiNW-r-800, SiNW-p-800 and PS-800, the blue emission and orange emission have comparable contributions to the total luminescence, while under higher temperature oxidation (SiNW-r-1000 and SiO₂nw), only the blue luminescence persists. For SiNW-r-1000, as shown in Figure 4-2, the orange luminescence only appears as a weak broad peak without fine structures. As for SiO₂nw, the XEOL only shows a single 460 nm emission.

Perhaps the most interesting feature is that from all 800 °C oxidized samples, the orange emission in XEOL profile can be seen splitting into a well-defined doublet at wavelengths of 623 nm and 645 nm, respectively. For PS-800 and SiNW-p-800, the 623 nm emission has a higher intensity than the 645 nm one, while for SiNW-r-800 the two

peaks are of relatively equal intensity. Interestingly, in spite of various relative peak intensities among the samples, the wavelength of each emission peak remains constant. On the other hand, the UV emission is at 300 nm for SiNW-p-800 and PS-800, but blue-shifted to 280 nm in SiNW-r-1000 and SiO₂nw. If we recall the Si K-edge XANES in Figure 4-1, we recognize that all samples have surface oxide layers of various thicknesses. In the discussion below, SiNW-p-800 will be focused on first to reveal the mechanism of the luminescence at different wavelengths, since it clearly exhibits optical emission in the three wavelength regions of interest. Discussions on the luminescence of PS-800 and SiO₂nw then follow.

4.3.2.1 PLY-XANES of SiNW-p-800

Luminescence of SiNW-p-800 with excitation energy across the Si L_{3,2}-edge is measured. Figure 4-3(a) is a XANES-XEOL display which shows the 2D contour map of the emission intensity (color-coded *z*-axis) as a function of incoming X-ray energy (*y*-axis) and emission wavelength (*x*-axis). In this display a horizontal cut yields the XEOL at a given excitation energy and a vertical cut yield the PLY at a given emission wavelength. The line spectrum shown on top is an example of a single XEOL spectrum obtained at an excitation energy of 120 eV (above the Si L_{3,2}-edge). The line shape of XEOL is similar to the one obtained above the Si K-edge (Figure 4-2). A closer examination of the 120 eV XEOL and 1900 eV XEOL side by side reveals that the branching ratio of the blue emission is greater under excitation energy of 120 eV. At the Si L-edge, the probing is more surface sensitive, thus a higher relative intensity of the blue emission indicates that this emission is more likely surface-related. The orange emission is less surface-sensitive, which could be from either the Si-SiO₂ interface or deep defect center of SiO₂.

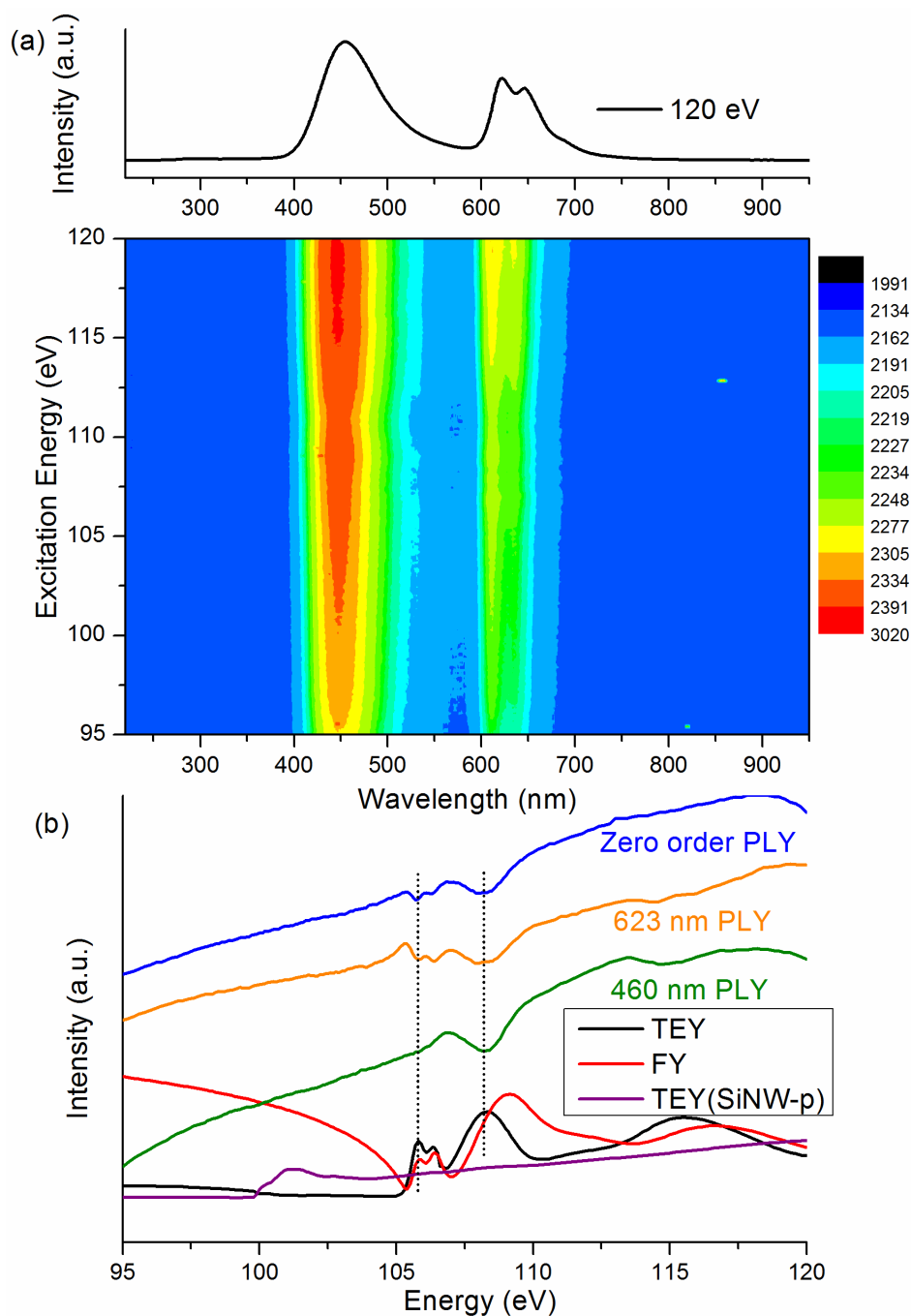


Figure 4-3 PLY of SiNW-p-800 across the Si $L_{3,2}$ -edge. (a) 2D XANES-XEOL plot and individual XEOL obtained under 120 eV excitation. (b) PLY-XANES at zero order and selected wavelengths (vertical cuts from Fig. 4-3(a)) in comparison with TEY and FY as well as the TEY of as-prepared SiNW-p.

It can be seen from the map that the total luminescence intensity shows a progressive increase as the excitation energy increases. This is because when the excitation is away from the threshold, the absorption is more monotonic: the higher the energy of the photon absorbed, the more the energy will be transferred to the optical channel. More abrupt changes often show up at the threshold when a new absorption channel turns on. Subtle variations of luminescence intensities are more clearly seen by extracting line spectra at wavelength of interest. In the following, the 460 nm emission and the 623 nm emission are chosen to represent the blue and the orange luminescence, respectively.

Figure 4-3(b) compares the PLY at zero order (total luminescence, 200-900 nm window), 460 nm and 623 nm with TEY- and FY-XANES. The TEY of SiNW-p before oxidation is also included as a reference. From the TEY, we can see that before oxidation, SiNW-p shows a clean elemental Si signal with the edge jump at ~ 99 eV, while the TEY of SiNW-p-800 is almost flat at this region. The resonances between 105-110 eV, marked by dotted lines, are the characteristic features of crystalline SiO_2 of tetrahedral local symmetry, and the sharp doublet arises from the spin-orbit splitting [21]. The FY of SiNW-p-800 shows a decrease in intensity toward 105 eV followed by a positive SiO_2 edge jump. This is due to self-absorption of the fluorescence X-ray for an optically thick sample. At the Si $L_{3,2}$ -edge, the attenuation length is $0.5 \mu\text{m}$ below and $0.05 \mu\text{m}$ above the edge, thus the sampling depth changes abruptly across the Si $L_{3,2}$ -edge [20]. Unlike Si K-edge FY, in which the X-ray penetrates considerably deeper so that Si contribution is discernible (Figure 4-1(b)), at the Si $L_{3,2}$ -edge, the elemental Si underneath is not detectable, and only SiO_2 features are observed with some distortion. Zero order PLY exhibits oscillations between 105-110 eV, showing spectral profile identical to the SiO_2

resonance in TEY and FY though inverted. At Si⁰ region (~99 eV), the PLY spectrum only displays monotonic response.

The 623 nm emission PLY shows a similar profile as the zero order PLY: a partially inverted spectrum with SiO₂ features. The PLY of 460 nm emission, however, only has a dip at ~108 eV without the fine structures. In other words, the spin-orbit splitting L₃- and L₂-edge is blurred. The observation suggests that the 460 nm emission is associated with a more distorted (chemically inhomogeneous) Si environment. The inversion of PLY at the edge could be due to multiple reasons: (a) the element in the material contributes to the light emission negatively, in other words, the decay of core electron after excitation prefers non-radiative channel (e.g. phonons); (b) the abrupt decrease of X-ray attenuation length (increase in absorption cross-section) leads to less efficient energy transfer to the optical channels, so the Auger and secondary electrons escape from surface without contributing to the optical emission via thermalization. Since a partial inversion is observed rather than a total inversion, it is more likely caused by the factor (b). In the following, the Si K-edge PLY is also examined to further support this point.

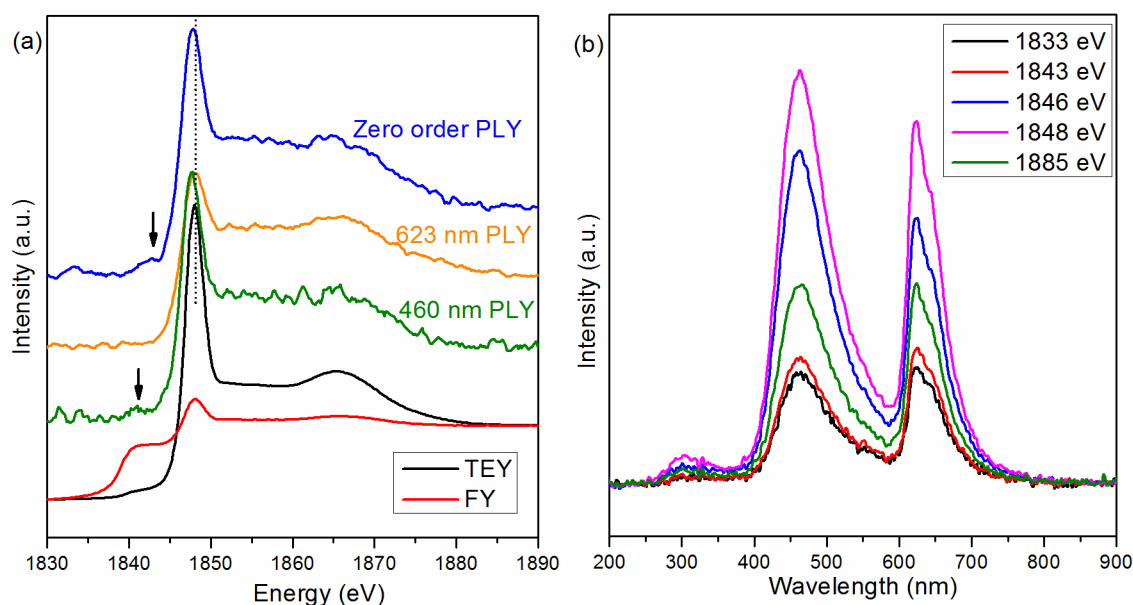


Figure 4-4 (a) Si K-edge PLY-XANES of SiNW-p-800, (b) selected XEOL of SiNW-p-800 with excitation energies below to above the Si K-edge.

Figure 4-4(a) shows the wavelength selected PLY with excitation energy across the Si K-edge. Both TEY and FY are included for comparison. It can be seen that at the Si K-edge, all PLY spectra have positive edge jumps, thus the X-ray energy is more efficiently transferred to the optical channel via secondary processes due to the considerably increased X-ray penetration depth at the Si K-edge. It can be seen that the zero order PLY follows the same trend as TEY, showing dominant SiO₂ features. Interestingly however, the peak maximum of PLY shifts slightly toward lower energy relative to TEY and FY. Also, a weak shoulder can be seen before the SiO₂ whiteline, marked by the arrow in the figure. This indicates that the luminescence observed from SiNW-p-800 is not entirely due to SiO₂, but also contains a noticeable contribution from species of a suboxide nature.

The two wavelength-selected PLY at 460 nm and 623 nm, shown in Figure 4-4(a), clearly reveals how the two emission bands contribute to the total luminescence. On one hand, both 460 nm and 623 nm PLY spectra are dominated by SiO₂ features, indicating that both of them are of primarily oxide origins. On the other hand, the low-energy peak shift of the SiO₂ whiteline is clearly seen from the 460 nm PLY. The peak maximum appears at 1847.6 eV, suggesting that the oxide, which is responsible for the blue luminescence, contains Si of oxidation state slightly less than +4 on average. Similar results have been reported by Daldosso *et al* on Si nanocrystals embedded SiO₂ films [22]. In their work, a lower energy shift in PLY relative to TEY was observed and the luminescence was attributed to Si-SiO₂ interface. In our case, however, the origin of the 460 nm luminescence could only partially come from the interface. If we recall the XEOL spectra of all SiNW samples (Figure 4-2), the 460 nm emission is always present even after the nanowires are heavily oxidized. Another possible origin of this 460 nm band should hence be considered. As it has been commonly observed, the 460 nm emission is also seen from silica samples and is attributed to the formation of oxygen deficient center (ODC) defect in which an oxygen atom is missing in the ≡Si-O-Si≡ network. The missing O atom could lead to an unpaired electron around Si, making the formal coordination state of Si less than +4. In fact, a previous XEOL study on quartz crystal also shows that there is an emission band at energy between 2.60 eV and 2.64 eV upon X-ray excitation that is attributed to structural defect of SiO₂ [23].

Returning to our case, the PLY spectra are more sensitive to the chemical environment associated with optical emission, while TEY or FY gives an averaged signal of SiO₂ absorption site, hence peak shift is observed in PLY but not in TEY or FY. However the

Si-SiO₂ interface may also contributed to the luminescence, the evidence is that a weak shoulder is seen at the lower energy side of the whiteline, indicating the luminescence also comes from Si suboxide formed at the Si-SiO₂ interface during oxidation. Whether it is a missing O defect in SiO₂ or Si suboxide at the interface, in both cases, the Si site of interest is in an oxidation state less than 4, which is responsible for the 460 nm emission band.

The 623 nm PLY, on the other hand, shows pure SiO₂ features identical to TEY as is observed at the Si L_{3,2}-edge discussed above. Although previously reported chemically or ambient oxidized porous Si as well as SiNW have luminescence within the similar wavelength region [14,24], the PLY spectra in those cases have a mixed feature of Si and SiO₂. In our case, no Si or its suboxide contribution is observed, thus the doublet 623-645 nm emission is likely solely due to SiO₂. In fact, silica is known to exhibit a PL band at this region (1.9 eV-2.0 eV), which has been attributed to non-bridging oxygen hole centers (NBOHC, ≡Si-O·) [8,23,25]. More details on the formation of NBOHC will be comparatively discussed later with ODC defect.

Figure 4-4(b) shows XEOL obtained with selected excitation energies from below to above the Si K-edge. The ratio of emission peak intensity varies along the excitation energies. When excited below the Si K-edge at 1833 eV, the 460 nm and the 623 nm emission are of relatively equal intensities. The energy at this point is not sufficiently high to excite any Si 1s electron, so the luminescence comes from the thermalization of electrons excited from the shallower levels. At 1843 eV, when Si 1s electrons from elemental Si are excited with an abrupt increase in Si absorption coefficient, the XEOL only shows a slight increase, indicating the decay of Si 1s electron from elemental Si

does not effectively transfer the energy to the optical channels. Both 460 nm and 623 nm emission increase under the excitation of 1846 eV, which is above the Si K-edge of elemental Si, but has not yet reached the SiO₂ whiteline. It is interesting that the 460 nm emission becomes more intense than the 623 nm one, and both emission peaks reach maximum at 1848 eV excitation while the 460 nm emission is of higher intensity. A close comparison of two emission bands reveals that the intensity ratio of 460 nm to 623 nm emission is slightly higher under the excitation of 1846 eV than 1848 eV, suggesting that the suboxide species also contributes to the 460 nm emission. The increase of the 460 nm emission intensity also agrees with the Si K-edge PLY spectra in Figure 4-4(a). Since the spectra are normalized to unit edge jump, the area under the SiO₂ whiteline in PLY is proportional to the quantum efficiency of energy transfer to the corresponding optical channels. It can be clearly seen that the 460 nm PLY has higher whiteline intensity than that of the 623 nm emission, which means (a) the site that contributes to the 460 nm emission favorably is of larger quantity than the one that favorably contributes to the 623 nm emission or (b) all sites contribute to both channels but the energy transfer to the 460 nm emission channel is more efficient. The latter is likely the dominant factor. The oxidized nano Si gives off luminescence at two wavelength regions of three possible origins: ODC emission from SiO₂ and the interface suboxide at 460 nm, and structural hole defect NBOHC emission of SiO₂ at 623-645 nm. The latter can be quenched entirely when Si is mostly converted to SiO₂.

The PLY of blue and orange emission at the O K-edge is also examined, shown in Figure 4-5(a). The absorption spectra (TEY and FY) of SiNW-p-800 show typical SiO₂ features: a broad resonance between 538 eV and 550 eV. The total PLY and the two sub-regions

show positive response once the O 1s electrons are excited. Particularly, the 623 nm emission is highly sensitive to the change in O absorption coefficient, and the spectrum follows the same trend as the absorption spectra across the edge. Figure 4-5(b) shows selected XEOL from below to above the O K-edge. It can be seen that the 623 nm emission is the optically preferred channel upon excitation of O 1s electron, showing a much higher intensity relative to the 460 nm emission at the edge. Comparing with Si K-edge XEOL, the 623 nm emission becomes sharper and of higher relative intensity than the 645 nm emission, which suggests the presence of two kinds of defect centers that are associated with the NBOHC defect, and the decay of O 1s core electron upon excitation has more efficient energy transfer to the 623 nm channel. It is also interesting to compare the XANES-XEOL results of SiNW in this work with free-standing SiNW using bottom-up vapor-liquid-solid (VLS) technique [26]. The VLS synthesized SiNW exhibit nearly identical behavior although it appears to contain less surface oxide. The orange and blue emission bands characterized by PLY at the O K-edge of VLS synthesized SiNW exhibit similar spectral features as observed in Figure 4-5(a) for SiNW-p-800: the orange emission (649 nm) tracks the O K-edge TEY-XANES but the blue emission (468 nm) is less sensitive to the variation of O absorption coefficient.

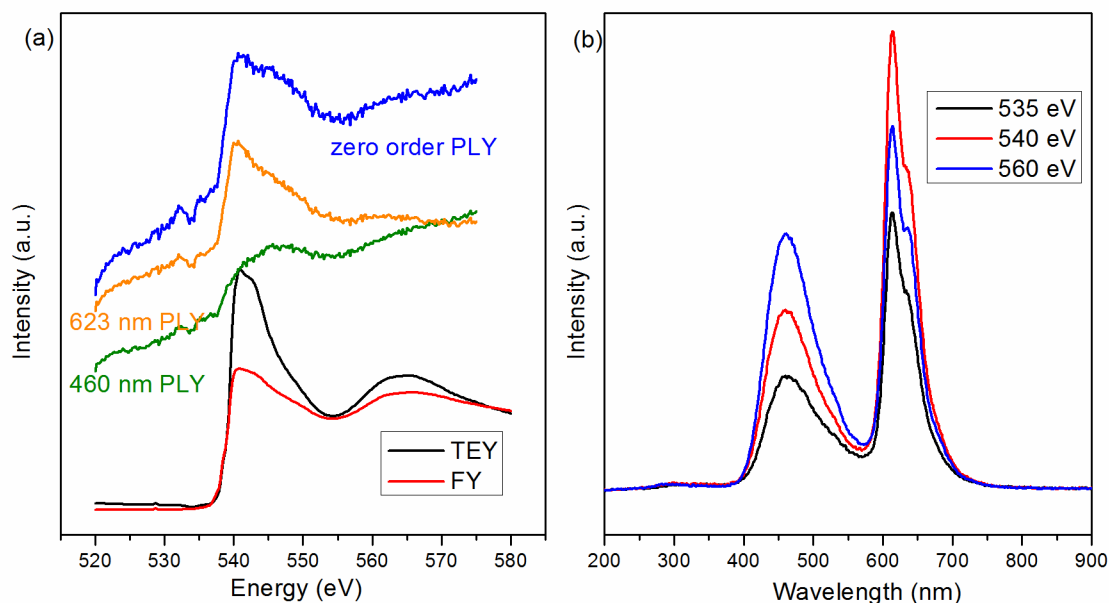


Figure 4-5 (a) O K-edge PLY-XANES of SiNW-p-800, (b) selected XEOL of SiNW-p-800 with excitation energies below to above O K-edge.

4.3.2.2 PLY-XANES of PS-800 and SiO₂nw

Wavelength selected PLY-XANES of PS-800 and SiO₂nw were also examined at the Si K-edge and the O K-edge, shown in Figure 4-6. It can be seen that PS-800 shows similar luminescence properties as SiNW-p-800: at the Si K-edge (Figure 4-6(a)), the whiteline of 460 nm luminescence shifts to lower energy; at the O K-edge (Figure 4-6(c)), only the 623 nm PLY shows positive optical response along the variation of O absorption coefficient. It should be noted that in SiNW-p-800, the blue emission has a larger contribution to the total luminescence, while PS-800 shows dominant orange emission. Heavily oxidized SiO₂nw has only the 460 nm emission, and the PLY tracks the absorption coefficient at Si K-edge, but is almost flat at the O K-edge. Interestingly, the 460 nm emission from SiO₂nw at Si K-edge has no sign of Si⁰ feature, indicating that the

luminescence is mainly from oxygen vacancy from bulk SiO_2 instead of the Si-SiO₂ interface, which is reasonable because either the SiNW is fully oxidized or the oxide layer is so thick that the interface region is no longer able to be probed by X-ray.

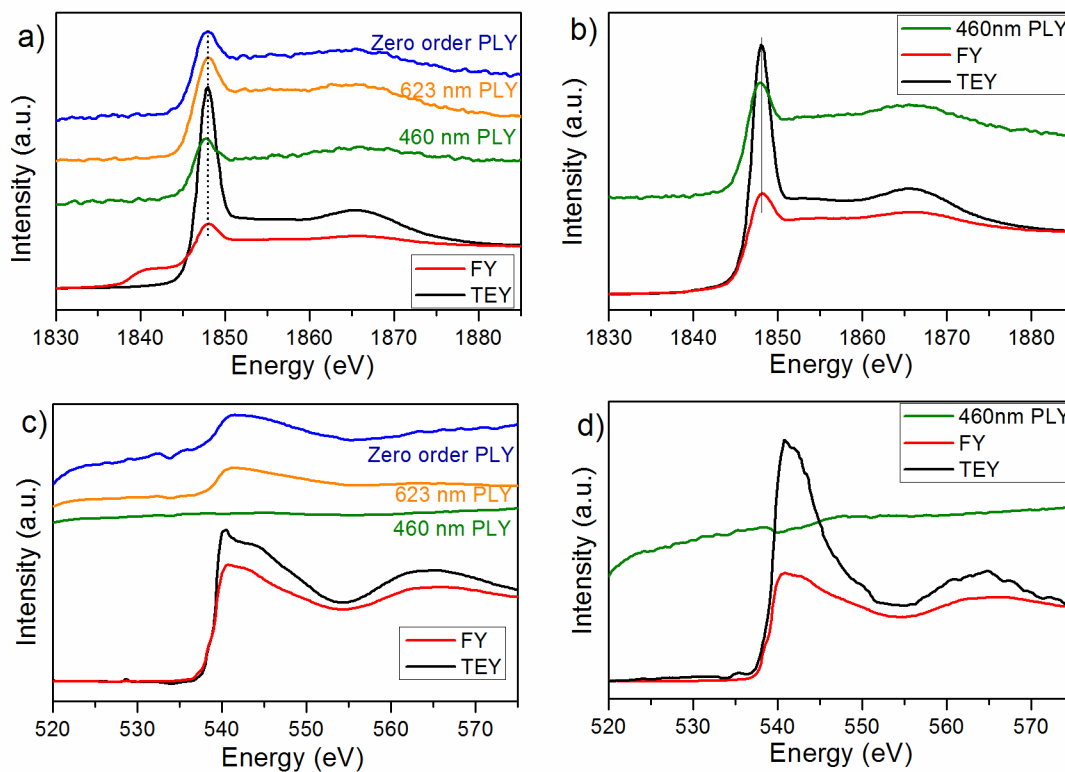


Figure 4-6 Si K-edge PLY-XANES of (a) PS-800 and (b) SiO₂nw, O K-edge PLY-XANES of (c) PS-800 and (d) SiO₂nw.

4.3.2.3 Luminescence centers and their correlation with material morphology and oxidation temperature

From PLY-XANES at Si L_{3,2}-, K- and O K-edge presented above, we know that the blue emission is sensitive to the absorption coefficient variation of Si core electrons in the SiO₂ environment, but less sensitive to O core electrons. Hence the blue emission is most likely associated with defect of silicon centers in an oxygen-deficient system, which is

consistent with the observation of the lower-energy shift of the Si K-edge PLY whiteline such as the one shown in Figure 4-4(a). The oxygen-deficient environment could be of two origins. Firstly, it could be the interface between Si and SiO₂, which is referred to as Si suboxide. Secondly, in SiO₂, there is an optically active defect center, which has been referred to as ODC centers in quartz or other silica samples [27-30]. According to theoretical calculations and previous photoluminescence (PL) experiments, two absorption bands at ~5 eV and ~7 eV, respectively, are attributed to two types of ODC centers: ODC (I)-type (7 eV), in which two adjacent Si atoms form a weak Si-Si bond ($\equiv\text{Si}-\text{Si}\equiv$), and ODC (II)-type (5 eV), in which paired electrons localized preferentially onto one Si atom forming divalent Si ($\equiv\text{Si}:\text{Si}\equiv$). The PL studies on high-purity silica glasses have shown the absorption of either 5 eV or 7 eV light could result in two PL bands at 4.4 eV (281 nm) and 2.7 eV (460 nm), which are identified as singlet-to-singlet transition (fast decay) and triplet-to-singlet transition (slow decay), respectively [29,31]. Actually, as shown in XEOL (Figure 4-2), the two emission bands are observed in all oxidized samples, though the intensity of 4.4 eV emission is fairly low. As of different probing mechanisms in which PL are populated by direct UV excitation whereas XEOL is populated by energy transfer, this discrepancy between PL and XEOL is due to the different decay process between excitation of valence electrons (PL) and core electrons (XEOL), and the latter favors the slow decay via thermalization (energy transfer).

The 623-645 nm luminescence is associated with the NBOHC. In contrast to the ODC luminescence, NBOHC related emission only shows up when Si is at an oxygen-rich environment [31]. Previously reported PL at 1.9 eV (652 nm) under laser excitation has emission peak sharper than the ODC luminescence [10,32], which is in good agreement

with our observation. The XEOL spectra show emission peak splitting into 623 nm and 645 nm regardless of sample morphology, but such splitting is rarely seen in PL.

Theoretically, O'Reilly and Robertson have calculated the energy diagrams of SiO₂ with oxygen defect centers of various configurations such as NBOHC ($\equiv\text{Si}-\text{O}\cdot$), peroxy radical ($\equiv\text{Si}-\text{O}-\text{O}\cdot$) and peroxy bridge ($\equiv\text{Si}-\text{O}-\text{O}-\text{Si}\equiv$) [27]. Experimentally, however, PL is only observed in the orange region which is associated with the formation of NBOHC. Meanwhile, it has been pointed out that the amount of $-\text{OH}$ content in the sample might be responsible for the PL emission peak at around 2 eV [33].

Here, the presence of two luminescent centers is suggested as the reason causing the emission peak splitting. The 645 nm emission is attributed to NBOHC, since its energy (1.92 eV) is close to the well-studied 1.9 eV PL emission. The NBOHC can be produced by multiple reactions: breaking the O-H bond in Si-O-H, or breaking the O-O bond in Si-O-O-Si or in Si-O-O-H [34]. The 623 nm emission, on the other hand, is attributed to the NBOHC ($\equiv\text{Si}-\text{O}\cdot$) bonded to the adjacent $\equiv\text{Si}-\text{H}$ forming a weak hydrogen bonding ($\equiv\text{Si}-\text{O}\cdots\text{H}-\text{O}-\text{Si}\equiv$). During chemical etching, the presence of HF in the solution causes the Si surface to be H-terminated ($\equiv\text{Si}-\text{H}$). Upon oxidation in air, the surface reacts with moisture in air forming $-\text{OH}$ termination ($\text{Si}-\text{H} + \text{H}_2\text{O} \rightarrow \text{Si}-\text{OH} + \text{H}_2$). The intensity of the 623 nm emission is thus qualitatively proportional to the amount of $-\text{OH}$ related NBOHC in the samples, among which PS-800 shows the highest intensity which is due to its high surface porosity. Further oxidation will remove the $-\text{OH}$ groups by the reaction $\text{Si}-\text{OH} + \text{Si}-\text{OH} \rightarrow \text{Si}-\text{O}-\text{Si} + \text{H}_2\text{O}$, hence quenches the 623 nm luminescence. This explains that both 645 nm and 623 nm emission present in SiNW-r-800 but the latter disappears in SiNW-r-1000.

4.4 Conclusion

The effect of thermal oxidation on the luminescence properties of various Si nanostructures is investigated. SiNW with smooth and porous surface, as well as porous Si are studied. It was found that although as-prepared SiNW and PS are barely light-emitting, bright luminescence is observed upon thermal oxidation. The emission spreads into three main sub-regions: the blue luminescence centered at 460 nm, the orange luminescence at 623 nm with a shoulder at 645 nm, and a weak emission in the UV 300 nm. The 460 nm and the UV emission originate from Si in an oxygen-deficient environment such as ODC defect of SiO₂ and the Si suboxide at Si-SiO₂ interface. The orange luminescence is from NBOHC in oxygen-rich SiO₂. The proposed mechanism of oxidation induced luminescence is as follows: at the initial stage of oxidation, oxygen-rich layer is formed and the presence of –OH and –O–O– produces intense orange luminescence; as the oxidation proceeds, oxide layer formed is oxygen-deficient thus the blue luminescence dominates and the orange luminescence ultimately diminishes entirely when the SiNW is fully oxidized.

4.5 References

- [1] Canham, L. T., *Appl. Phys. Lett.* **1990**, *57*, 1046-1048.
- [2] Cullis, A. G.; Canham, L. T.; Calcott, P. D. J., *J. Appl. Phys.* **1997**, *82*, 909.
- [3] Takagahara, T.; Takeda, K., *Phys. Rev. B* **1992**, *46*, 15578-15581.
- [4] Allan, G.; Delerue, C.; Lannoo, M., *Phys. Rev. Lett.* **1996**, *76*, 2961-2964.
- [5] Van Buuren, T.; Gao, Y.; Tiedje, T.; Dahn, J. R.; Way, B. M., *Appl. Phys. Lett.* **1992**, *60*, 3013-3015.

- [6] English, D. S.; Pell, L. E.; Yu, Z.; Barbara, P. F.; Korgel, B. A., *Nano Lett.* **2002**, *2*, 681-685.
- [7] Kang, Z.; Liu, Y.; Tsang, C. H. A.; Ma, D. D. D.; Fan, X.; Wong, N.-B.; Lee, S.-T., *Adv. Mater.* **2009**, *21*, 661-664.
- [8] Glinka, Y. D.; Lin, S.-H.; Hwang, L.-P.; Chen, Y.-T.; Tolk, N. H., *Phys. Rev. B* **2001**, *64*, 085421.
- [9] Pacchioni, G.; Ierano, G., *Phys. Rev. Lett.* **1997**, *79*, 753-756.
- [10] Stathis, J. H.; Kastner, M. A., *Phys. Rev. B* **1987**, *35*, 2972-2979.
- [11] Liao, L.-S.; Bao, X.-M.; Zheng, X.-Q.; Li, N.-S.; Min, N.-B., *Appl. Phys. Lett.* **1996**, *68*, 850-852.
- [12] Sham, T. K.; Naftel, S. J.; Kim, P. S. G.; Sammynaiken, R.; Tang, Y. H.; Coulthard, I.; Moewes, A.; Freeland, J. W.; Hu, Y. F.; Lee, S. T., *Phys. Rev. B* **2004**, *70*, 045313.
- [13] Yu, D. P.; Hang, Q. L.; Ding, Y.; Zhang, H. Z.; Bai, Z. G.; Wang, J. J.; Zou, Y. H.; Qian, W.; Xiong, G. C.; Feng, S. Q., *Appl. Phys. Lett.* **1998**, *73*, 3076-3078.
- [14] Coulthard, I.; Antel, W. J.; Antel Jr, W. J.; Freeland, J. W.; Sham, T. K.; Naftel, S. J.; Zhang, P., *Appl. Phys. Lett.* **2000**, *77*, 498-500.
- [15] Hu, Y. F.; Zuin, L.; Wright, G.; Igarashi, R.; McKibben, M.; Wilson, T.; Chen, S. Y.; Johnson, T.; Maxwell, D.; Yates, B. W.; Sham, T. K.; Reininger, R., *Rev. Sci. Instrum.* **2007**, *78*, 083109.
- [16] Regier, T.; Paulsen, J.; Wright, G.; Coulthard, I.; Tan, K.; Sham, T. K.; Blyth, R. I. R., *AIP Conf. Proc.* **2007**, *879*, 473-476.
- [17] Sham, T. K.; Naftel, S. J.; Kim, P. S. G.; Sammynaiken, R.; Tang, Y. H.;

- Coulthard, I.; Moewes, A.; Freeland, J. W.; Hu, Y. F.; Lee, S. T., *Phys. Rev. B* **2004**, *70*, 045313.
- [18] Sham, T. K.; Jiang, D. T.; Coulthard, I.; Lorimer, J. W.; Feng, X. H.; Tan, K. H.; Frigo, S. P.; Rosenberg, R. A.; Houghton, D. C.; Bryskiewicz, B., *Nature* **1993**, *363*, 331-334.
- [19] Coulthard, I.; Sham, T. K., *Solid State Commun.* **1999**, *110*, 203-208.
- [20] X-ray Calculator. http://henke.lbl.gov/optical_constants/
- [21] Kasrai, M.; Lennard, W. N.; Brunner, R. W.; Bancroft, G. M.; Bardwell, J. A.; Tan, K. H., *Appl. Surf. Sci.* **1996**, *99*, 303-312.
- [22] Daldosso, N.; Luppi, M.; Ossicini, S.; Degoli, E.; Magri, R.; Dalba, G.; Fornasini, P.; Grisenti, R.; Rocca, F.; Pavesi, L.; Boninelli, S.; Priolo, F.; Spinella, C.; Iacona, F., *Phys. Rev. B* **2003**, *68*, 085327.
- [23] Jurgensen, A.; Anderson, A. J.; Sham, T. K., *Phys. Chem. Minerals* **2009**, *36*, 207-216.
- [24] Rosenberg, R. A.; Shenoy, G. K.; Kim, P. S. G.; Sham, T. K., *J. Phys. Chem. C* **2008**, *112*, 13943-13946.
- [25] Sham, T. K., *Int. J. Nanotechnol.* **2008**, *5*, 1194-1246.
- [26] Sham, T. K.; Kim, P. S. G.; Lam, S.; Zhou, X. T.; Rosenberg, R. A.; Shenoy, G. K.; Heigl, F.; Jurgenen, A.; Regier, T.; Coulthard, I.; Zuin, L.; Hu, Y. F., *SRMS-5 Conference* **2006**, 112.
- [27] O'Reilly, E. P.; Robertson, J., *Phys. Rev. B* **1983**, *27*, 3780-3095.
- [28] Imai, H.; Arai, K.; Imagawa, H.; Hosono, H.; Abe, Y., *Phys. Rev. B* **1988**, *38*, 12772.

- [29] Skuja, L., *J. Non-Cryst. Solids* **1998**, *239*, 16-48.
- [30] Tohmon, R.; Mizuno, H.; Ohki, Y.; Sasagane, K.; Nagasawa, K.; Hama, Y., *Phys. Rev. B* **1989**, *39*, 1337-1345.
- [31] Nishikawa, H.; Shiroyama, T.; Nakamura, R.; Ohki, Y.; Nagasawa, K.; Hama, Y., *Phys. Rev. B* **1992**, *45*, 586-591.
- [32] Anedda, A.; Bongiovanni, G.; Cannas, M.; Congiu, F.; Mura, A.; Martini, M., *J. Appl. Phys.* **1993**, *74*, 6993-6995.
- [33] Munekuni, S.; Yamanaka, T.; Shimogaichi, Y.; Tohmon, R.; Ohki, Y.; Nagasawa, K.; Hama, Y., *J. Appl. Phys.* **1990**, *68*, 1212-1217.
- [34] Nishikawa, H.; Nakamura, R.; Tohmon, R.; Ohki, Y.; Sakurai, Y.; Nagasawa, K.; Hama, Y., *Phys. Rev. B* **1990**, *41*, 7828-7834.

Chapter 5

5 Electronic Structure and Optical Property Studies of SiC Nanostructures and Polytypes

5.1 Introduction

Silicon carbide (SiC) has a variety of unique properties. It is of high chemical inertness and good thermal conductivity and is regarded as a promising substitute for silicon in fabricating devices which operate at extreme conditions (i.e., high temperature and high power) [1,2]. In SiC crystals, the Si and C atoms are linked through an sp^3 bonding network, forming close-packed Si-C tetrahedral units. SiC crystals can be further categorized according to the stacking sequence of such tetrahedral units, referred to as polytypes. The commonly found SiC polytypes are denoted 6H-, 4H-, 2H- and 3C-SiC. The letters in the labels represent the types of the crystal systems (i.e. H for hexagonal and C for cubic), while the numbers refer to the layers of Si-C per unit cell. All SiC polytypes are indirect band gap semiconductors, and the band gap increases with increasing of hexagonal character in the polytypes. The band gaps for the common SiC polytypes are: 2.36 eV in 3C-SiC, 3.02 eV in 6H-SiC, 3.23 eV in 4H-SiC, and 3.33 eV in 2H-SiC [3]. Studies have been carried out on the physical and chemical properties of all four types of SiC, among which 6H-SiC and 3C-SiC are the most stable structures and the easiest to obtain, hence are of most interest. 6H-SiC single crystals can be grown in high quality in industry at high temperature (i.e. >1700 °C), while 3C-SiC requires lower temperature and are often grown under a controlled condition. The advantages of 6H-SiC

* A version of this chapter has been published in *J. Phys. Chem. C* **2010**, *114*,6966

are its high breakdown field strength due to the large band gap and its commercial availability [4]. 3C-SiC, on the other hand, has higher electron mobility and is usually fabricated at the nanoscale. It has been reported that the oxide coated 3C-SiC nanostructure is a good candidate for photocatalysis applications [5].

There have been many studies on the electronic structures of SiC polytypes both experimentally and theoretically. Although having the same Si-C tetrahedral local structure, the band structure becomes increasingly complicated as the symmetry of the crystal structure lowers. *Ab initio* pseudopotential calculations have been widely used for band structure studies of SiC polytypes, and the results show that the valence band structure of SiC is very similar regardless of the polytypes [6-9]. However, the unoccupied density of states (DOS)/conduction band shows noticeable differences among the polytypes. It is hence considered that the differences in the unoccupied DOS play a major role in causing a variation in the energy of band gap [8]. Despite many theoretical calculations on SiC polytypes, experimental results are relatively lacking.

In addition, luminescence from SiC materials has been widely studied as the wide band gap makes them good light-emitting materials [10]. It has been reported that bulk SiC exhibits weak photoluminescence (PL) at 600 nm at low temperature, which is assigned to donor-acceptor recombination [11,12]. SiC of micro- and nanostructures, on the other hand, are found to emit light with significantly increased intensity compared to their bulk counterparts. Porous SiC, which is made by electrochemically etching a piece of SiC wafer (6H-SiC in most cases), exhibits blue-green PL and the PL intensity is enhanced upon irradiation and oxidation [13]. This makes SiC an attractive light-emitting material in the fields of micro- and nanoelectronic and optical devices. The origin of the

luminescence has been widely discussed. Since the PL observed in most cases are below the band gap energy, the luminescence is usually attributed to surface-related defects [14-16]. Luminescence from other SiC nanostructures, such as SiC nanocrystals embedded matrix [17,18], SiC nanowires [19,20], and SiC-SiO₂ complexes [21], has been reported in the range of 400 nm-600 nm. The origin of the luminescence is still not yet clearly understood. On one hand, luminescence has been assigned to SiC band gap emission upon quantum confinement. On the other hand, SiO₂, which is usually present on the SiC surface, is known to show an intense blue emission band at 460 nm. The origin of the observed emission is thus difficult to distinguish due to the possibility of contributions from either or both species.

In this chapter, four micro- and nanostructured SiC of 6H- and 3C-phases are studied comparatively using X-ray absorption near-edge structure (XANES) and X-ray excited optical luminescence (XEOL). Theoretical calculations are also performed using density functional theory (DFT) which provides band structures and DOS information as well as simulated XANES for comparison with the experimental spectra. The luminescence of SiC is studied using wavelength selected photoluminescence yield (PLY)-XANES providing element and site specificity in order to reveal the origin of the observed emission bands.

5.2 Experimental and Calculation Procedures

The 3C-SiC core-shell nanowires were prepared using a thermal evaporation method [22]. The synthesis was carried out in a vertical high-frequency induction furnace which consists of a quartz tube and an inductive heat cylinder crucible of high-purity graphite. The SiO powder, used as the source material, was placed in the graphite crucible. An

activated carbon fiber (ACF) layer was packed outside of the crucible. The system was rapidly heated to 1450 °C within 2 minutes and maintained for 15 minutes under high purity Ar. The SiO gas was carried to the ACF layer by Ar, and the deposition reaction took place on the ACF surface, forming core-shell SiC –SiO₂ nanowires of a light-blue color. The scanning electron microscopy (SEM) image (Figure 5-1 (a)) and transmission electron microscopy (TEM) image (Figure 5-1(b)) show that the as-prepared SiC nanowires are core-shell structures with diameter of ~50 nm. X-ray diffraction (XRD) patterns (Figure 5-1(c)) confirms that the SiC nanowires are of cubic (3C-SiC) structure. To remove the SiO₂ shell, the product was immersed into a 5% hydrofluoric acid (HF) for 3 minutes and then rinsed with water. The as-prepared core-shell SiC nanowires were denoted “3C-cs”, and the nanowires after shell removal were denoted “3C-nw”.

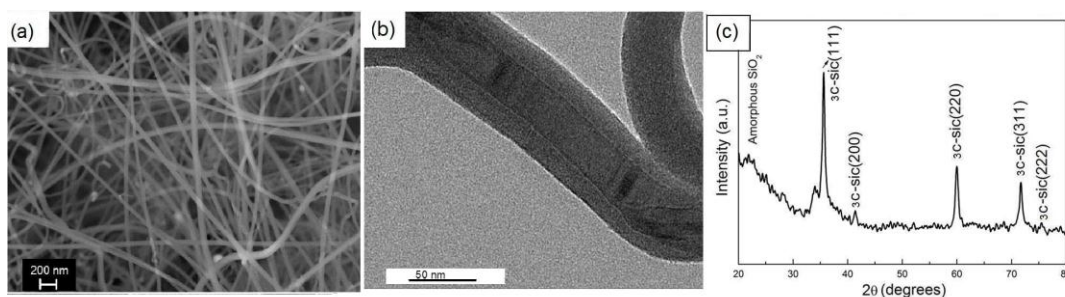


Figure 5-1 Morphology of 3C-cs in (a) SEM and (b) TEM, (c) XRD pattern of 3C-cs

The 6H-SiC microcrystals were obtained from Sigma Aldrich and denoted “6H-mc”. The crystals are of 200-450 mesh in particle size, which are ~50 μm. 6H-SiC crystal powders, which were obtained from Alfa Aesar, are of 1 μm in average particle sizes and denoted “6H-pd”. 3C-SiC nanopowders of particle size 45-55 nm were obtained from Alfa Aesar and denoted “3C-pd”. All commercially obtained samples were measured directly without further purification.

Synchrotron measurements were performed at the Canadian Light Source (CLS). XANES and XEOL spectra of all the SiC samples were examined at Si K- and C K-edge at the high resolution spherical grating monochromator beamline (SGM) [23]. XANES were recorded in the modes of total electron yield (TEY) and X-ray fluorescence yield (FY). XEOL was measured with XANES using a dispersive optical spectrometer (Ocean Optics QE65000). Photoluminescence yield (PLY) was obtained by simultaneously collecting XEOL while measuring XANES spectra. PLY can be recorded as the total luminescence (zero order, 200-1000nm) or by selecting a desired optical window (partial PLY). All spectra are normalized to the incident photon flux.

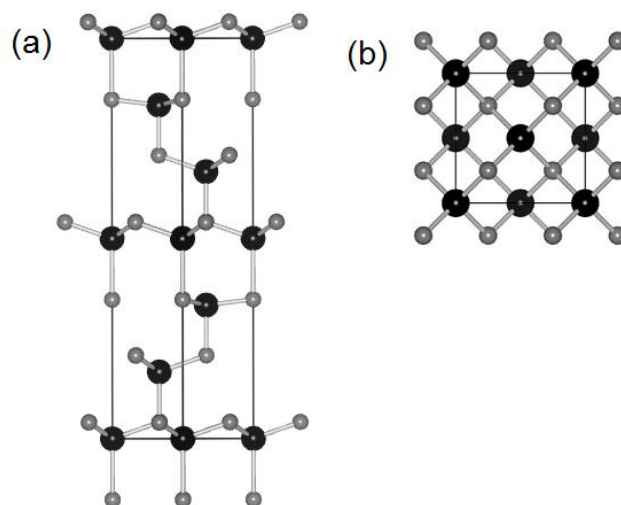


Figure 5-2 Sketch of SiC crystal structures drawn using the VESTA program [24]

(a) 6H-SiC and (b) 3C-SiC. Si atoms in black, C atoms in grey

The electronic structures of SiC were calculated using the density functional theory (DFT) [25,26] together with generalized gradient approximation (GGA) [27]. The full potential augmented plane wave method was utilized in the numerical calculation

employing the WIEN2k code [28,29]. The crystal structures of 6H-SiC and 3C-SiC were based on the models illustrated in Figure 5-2. 6H-SiC has a hexagonal unit cell with the space group of $P6_3mc$, and the lattice constants are $a=3.073 \text{ \AA}$, $c=15.08 \text{ \AA}$. The Si and C atoms occupy the $2a$ $(0, 0, u)$ and $2b$ $(1/3, 2/3, v)$ positions with $u[\text{Si}]=1/8$, $v[\text{Si}]=7/24$, $23/24$, $u[\text{C}]=0$ and $v[\text{C}]=1/6, 5/6$. For 3C-SiC, the zincblende crystal structure with the symmetry group of $F-43m$ and lattice constant $a=4.358 \text{ \AA}$ were used. The Si atoms are located at the $4a$ positions of $(0, 0, 0)$ and the C atoms are located at the $4c$ positions of $(1/4, 1/4, 1/4)$ [30,31]. The atomic sites are represented by spherical base sets, which are generated by a linear combination of radial wave functions and non-overlapping spherical harmonics. The interstitial regions are expressed by a set of 10000 plane waves. The boundary condition between the atomic sites and the interstitial areas satisfies the Dirichlet boundary condition. In the numerical calculation, the tetrahedron method [32] for the k-space integration was used. The theoretical XANES spectra were then calculated using the electrical dipole transition, convoluted by instrumental Gaussian and core-hole lifetime Lorentzian broadening. The core-hole lifetime used is 0.48 eV for Si K-shell and 0.2 eV for C K-shell [33].

5.3 Results and Discussions

5.3.1 Electronic Structures and SiC

5.3.1.1 Si K-edge XANES

Figure 5-3 shows the Si K-edge XANES of 6H-pd, 6H-mc and 3C-pd. Let us first take a look at the two 6H-SiC samples. The TEY spectra of the two samples are identical: a shoulder at 1841 eV, three peaks at 1846 eV, 1852 eV and 1860 eV, which are the characteristic features of SiC [34]. The peak of the highest intensity, the 1846 eV

resonance, is attributed to the excitation from Si 1s to Si 3p-C 2sp hybridized states [35,36]. The resonances at higher energies correspond to the Si unoccupied *p*-DOS due to multiple scattering. The FY spectra show similar features as the TEY but broadened, particularly in 6H-mc. The attenuation of FY spectrum is due to self-absorption (thickness effect). The X-ray one-absorption length at the Si K-edge is $\sim 1.26 \mu\text{m}$, which is smaller than the average size of SiC microcrystals (6H-mc) [37], so that the X-ray fluorescence is partially re-absorbed by the sample, resulting a distortion in the FY spectrum. Less attenuation is seen in the FY of 6H-pd, due to the decreased particle size.

The XANES of 3C-pd exhibits similar profile as its 6H-phase counterpart. This is not surprising since both 6H-SiC and 3C-SiC have a similar Si-C local structure, as shown in the schematic drawing in Figure 5-2. A closer examination reveals that the main resonance peak in 3C-pd is narrower compared to 6H-pd and 6H-mc, indicating that the interaction between the Si-C tetrahedral units in the 3C-phase SiC is less extensive than that in the 6H-SiC.

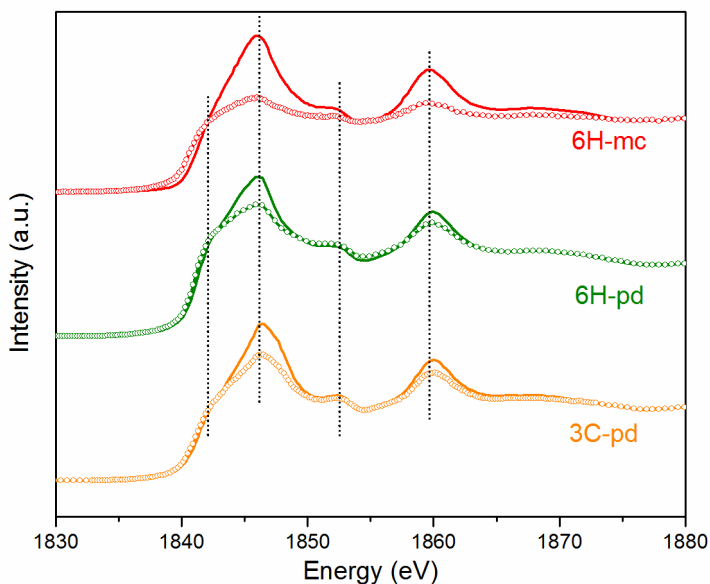


Figure 5-3 Si K-edge XANES of 6H-mc, 6H-pd and 3C-pd. Solid lines: TEY, open circles: FY.

Figure 5-4 shows the calculated partial density of states (DOS) at the Si site and the Si K-edge XANES spectra of 6H- and 3C-SiC calculated by WIEN2k in comparison with the experimental ones. It can be seen that although the partial DOS gets more complicated with increasing crystal packing complexity, the overall profiles are similar between 6H- and 3C-SiC. The partial DOS of *p* character contributes mainly to the conduction band, and the calculated XANES spectra are in good agreement with the ones measured experimentally. A more noticeable pre-edge shoulder can be seen in 6H-SiC from calculated XANES than in 3C-SiC, which explains the observed broadening of the 1845 eV peak in 6H-SiC.

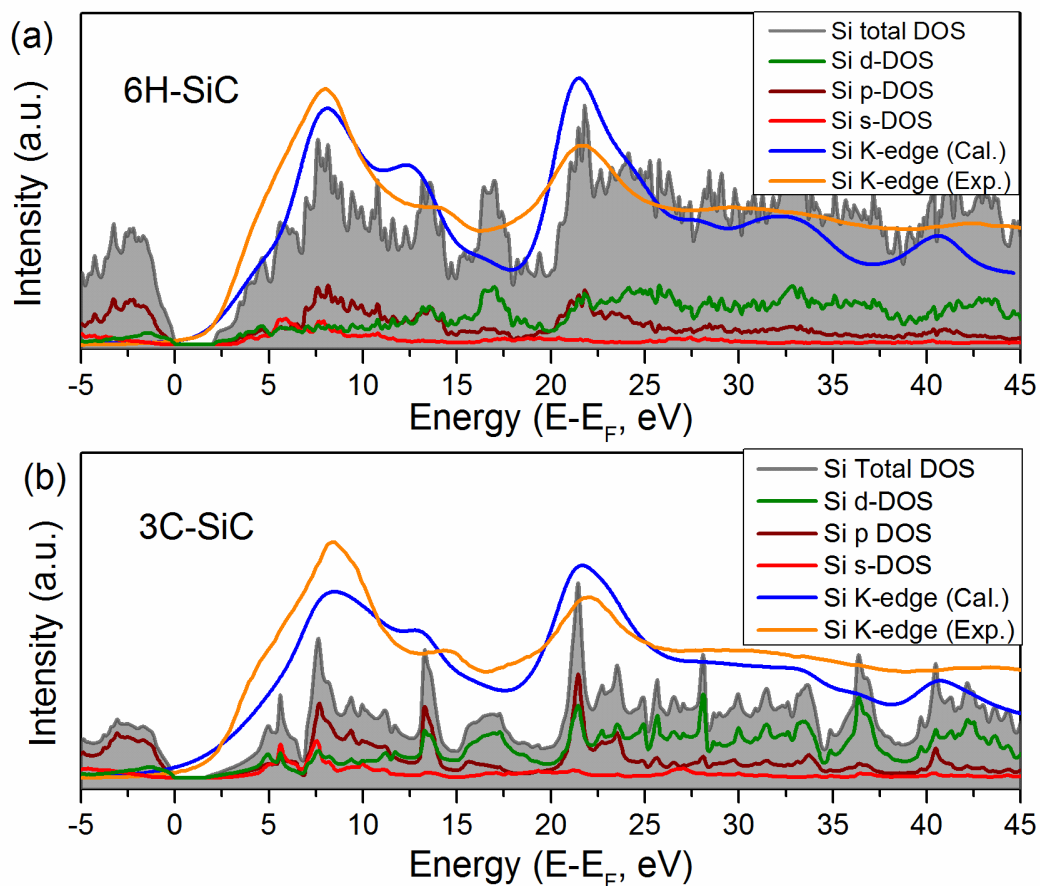


Figure 5-4 Calculated Si K-edge XANES and DOS plots in comparison with experimental XANES. (a) 6H-SiC, 6H-mc TEY is used as experimental spectrum; (b) 3C-SiC, 3C-pd TEY is used as experimental spectrum.

The XANES spectra of the as-prepared core-shell nanowires (3C-cs) and nanowires with SiO₂ shell removed (3C-nw) are shown in Figure 5-5. In 3C-cs, both TEY and FY display a shoulder at 1841 eV, which is at the same location as that observed in 3C-pd. However, the peak of maximum intensity is found at 1848 eV instead of 1846 eV, followed by two broad resonances at energies 1860 eV and 1866 eV. The 1848 eV peak is the characteristic whiteline feature of SiO₂ [38], as can be seen the similarity between 3C-cs

and SiO₂ reference spectra. The outer SiO₂ shell hence contributes to the XANES significantly in both TEY and FY. After HF treatment, the 1848 eV whiteline peak disappears, and the XANES of 3C-nw show all the characteristic features of 3C-phase SiC.

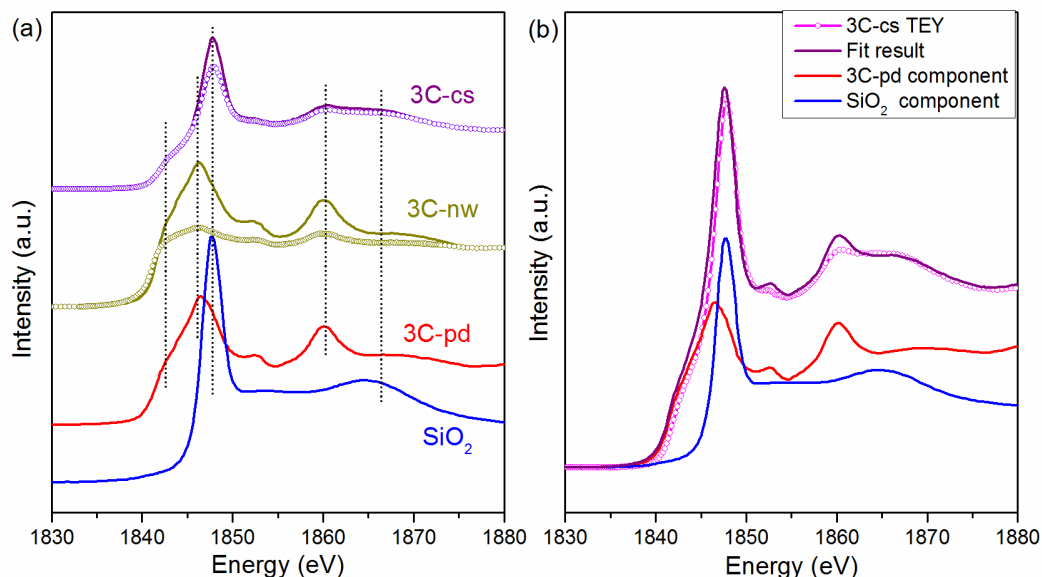


Figure 5-5 (a) Si K-edge XANES of 3C-cs and 3C-nw in TEY and FY. The TEY spectra of 3C-pd and SiO₂ are shown for comparison. (b) Linear combination fit results of 3C-cs TEY.

Figure 5-5 (b) shows a component analysis of 3C-cs using a linear combination fit. The fitting was performed on the TEY of 3C-cs using 3C-pd and SiO₂ TEY spectra as references. It can be seen the fitted spectrum is in very good agreement with the experimentally obtained TEY. The edge jump ratio of the SiC and SiO₂ components is around 1:1, indicating the core-shell SiC nanowire has a thick oxide outer layer.

However, as shown in Figure 5-5 (a), the oxide layer can be removed successfully by HF treatment.

5.3.1.2 C K-edge XANES

The C K-edge XANES of 6H-pd, 6H-mc and 3C-pd are shown in Figure 5-6. It can be seen that all spectra have rich features at energy between 285 eV and 300 eV. The main resonance is the dipole transitions of C $1s$ to σ^* from sp^3 bonded carbon [35]. The small peak seen in the TEY at 286.4 eV in 6H-mc and 6H-pd is usually assigned to C $1s$ to π^* transition [39]. Since TEY is surface sensitive, this peak is likely due to the presence of defects at the surface, in which C is sp^2 bonded. Such feature is absent in FY, since FY is more bulk sensitive. The TEY of 3C-pd shows some spikes at the pre-edge region (285 eV-288 eV), which is due to charging at the sample surface [40]. Since the photon flux and the absorption coefficient at the C K-edge are significantly higher than at the Si K-edge [41], no charging effect is observed at the Si K-edge XANES. The overall FY spectral profiles of the 6H- and 3C-SiC samples are very similar to each other, but there are also some slight differences. The onset (edge jump) of the 3C-pd FY shows up at an energy lower than the ones of 6H-mc and 6H-pd. In addition, the peaks of 3C-pd are sharper than 6H-mc and 6H-pd, and the pre-edge shoulder is apparent at 285.4 eV in 3C-pd but rather broad in 6H-mc and 6H-pd.

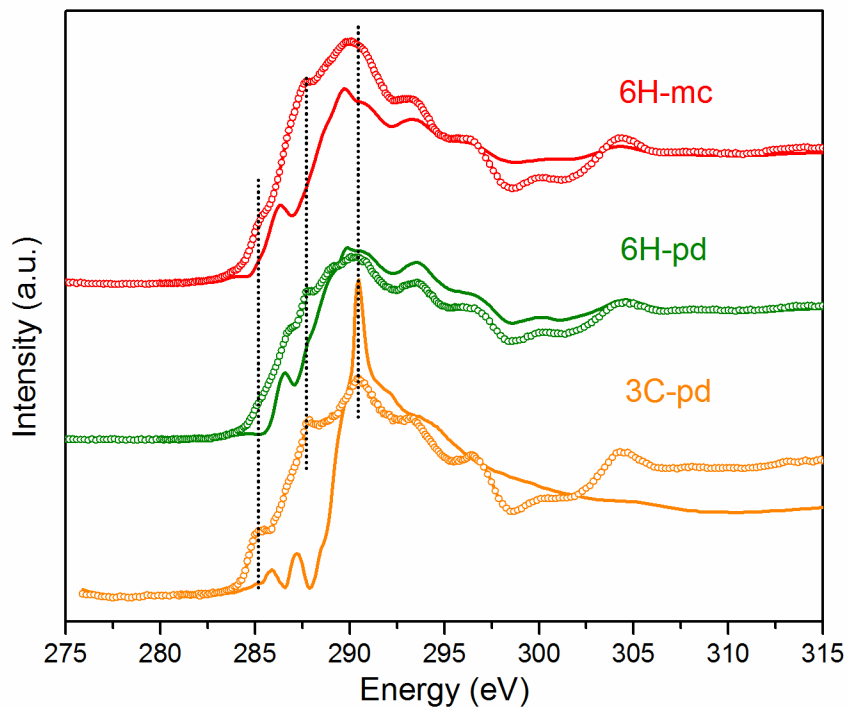


Figure 5-6 C K-edge XANES of 6H-mc, 6H-pd and 3C-pd. Solid lines: TEY, open circles: FY

The DOS plots of 6H-SiC and 3C-SiC together with the calculated XANES spectra at the C K-edge are shown in Figure 5-7. It can be seen that 3C-SiC reveals a slightly narrower band gap than that in 6H-SiC, which explains the edge jump discrepancies observed in Figure 5-6 between 3C-SiC and 6H-SiC. As the strongest contribution to the total DOS in the conduction band comes from Si *s* and C *p* band, seen from Figure 5-4 and Figure 5-7, the edge jump differences between the two phases can be more readily observed at the C K-edge but not obvious enough at Si K-edge. The calculated XANES agree with the experimental spectra reasonably well in the near-edge region, i.e. within the first 20 eV. The main resonance at ~10 eV are sharper in 3C-SiC than in 6H-SiC, which is reproduced by calculation, but the relative intensities of the peaks are not quite the same.

In addition, the calculated spectra clearly show the pre-edge feature at ~ 5 eV in both 6H-SiC and 3C-SiC. These discrepancies could be partly due to vibrational broadening and partly due to energy dependent final state lifetime.

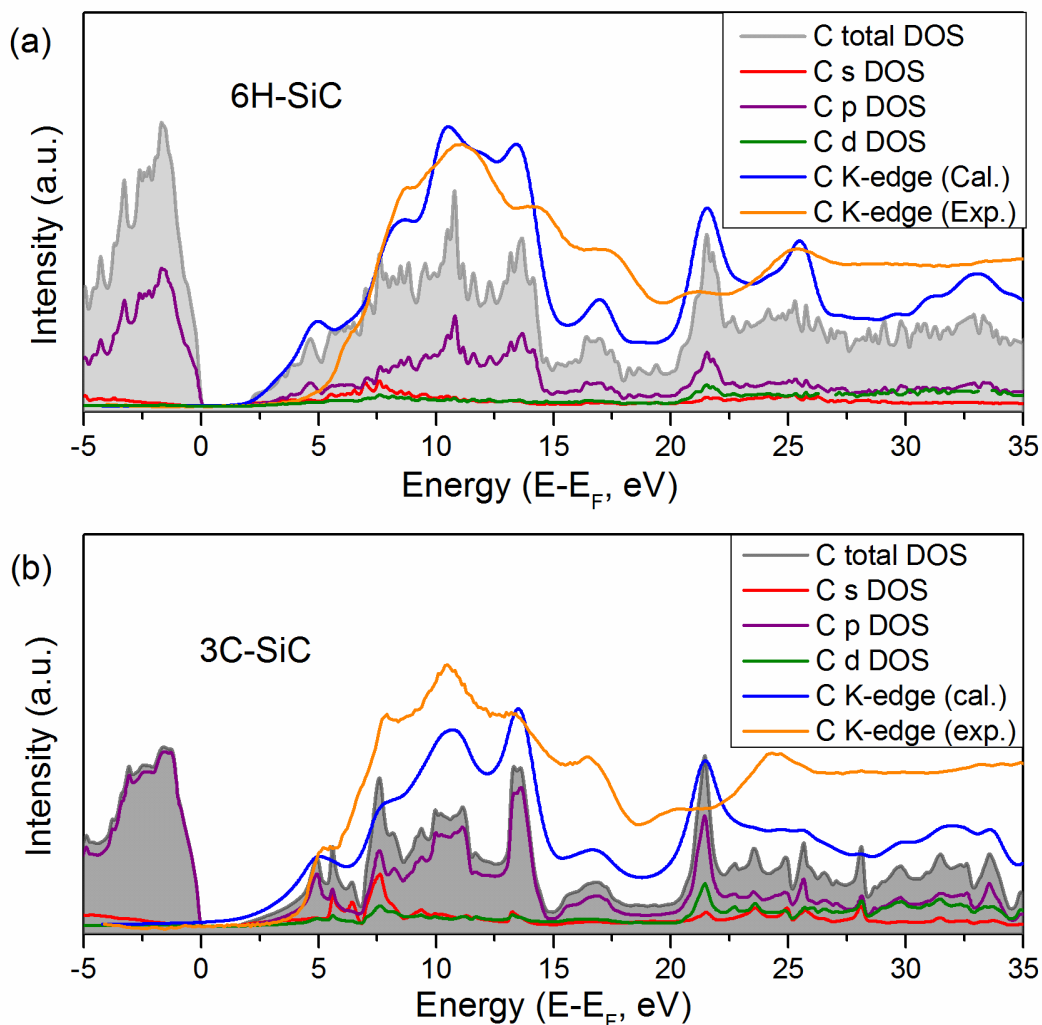


Figure 5-7 Partial DOS plots of C site and calculated C K-edge XANES in comparison with experimental XANES. (a) 6H-SiC, (b) 3C-SiC.

The C K-edge XANES of the core-shell nanowires 3C-cs and HF-treated nanowires SiC-nw samples are shown in Figure 5-8. At first glance, the XANES of SiC nanowires look

quite different before and after HF treatment. In 3C-nw, the spectra display all the resonances which belongs to 3C-SiC, in agreement with the XRD results, although the charging problem still exists in TEY, shown as a dip when the excitation energy is approaching the edge. As for the core-shell 3C-cs sample, however, both TEY and FY show a sharp peak at 286 eV and another peak at 292 eV, neither of which is present in 3C-nw or 3C-pd spectra. These peaks are almost certainly due to impurities which contain sp^2 bonded C. The source of the C impurities could be the unreacted C from the synthesis process. Assuming the majority of the impurity remains on the sample surface, a difference curve is obtained by subtracting TEY from FY after normalizing the two spectra to the π^* peak. This procedure allows minimizing the surface carbon contamination assuming that the FY contains signal from both surface and bulk whereas TEY contains mostly surface signal. Shown in Figure 5-8, the difference curve reveals all major features of 3C-SiC, marked by dotted lines. This observation confirms that the impurities were mainly on the surface and the removal of SiO_2 shell using HF also removed the surface impurities.

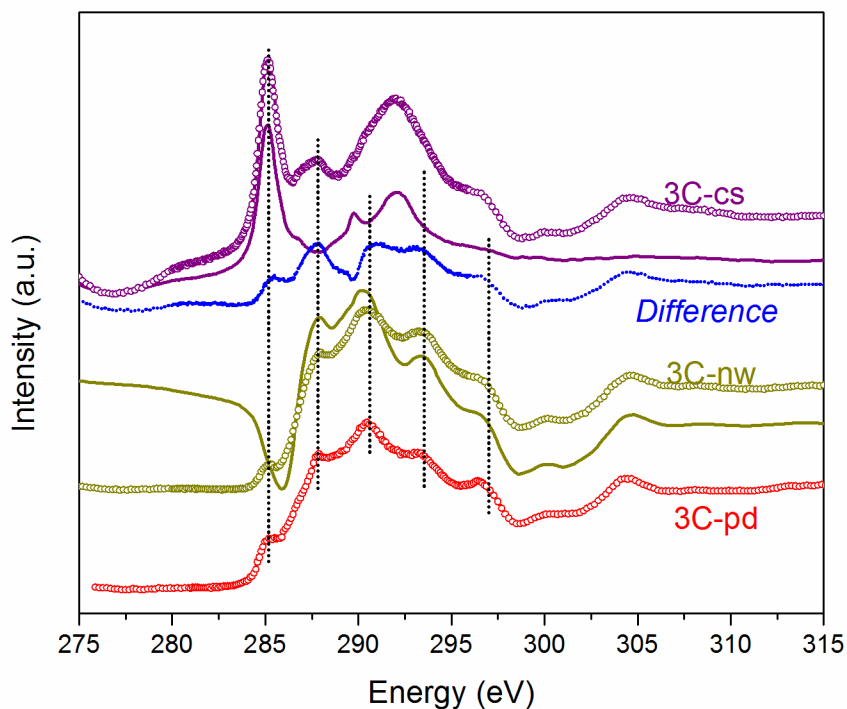


Figure 5-8 C K-edge XANES of 3C-cs and 3C-nw in TEY (solid lines) and FY (open circles). The 3C-pd FY spectrum is shown as reference.

5.3.2 Optical Properties of SiC

5.3.2.1 XEOL of 6H-SiC

The XEOL spectra of 6H-pd and 6H-mc are shown in Figure 5-9. The excitation energies selected are 1860 eV and 290 eV, which are above the Si K-edge and C K-edge, respectively. The spectra are normalized to the incident photon flux. Upon X-ray excitation, both 6H-mc and 6H-pd emit bright luminescence, shown as a broad peak at energy around 2.0 eV (620 nm), which is lower than the band gap energy of 6H-SiC (3.02 eV). At first glance, the luminescence has no apparent difference between the two samples. However, if we look at the peak profile closely, we see that the XEOL for 6H-pd, excited above both Si K- and C K-edges, can be fitted using two Gaussian peaks with

comparable intensities, located at 1.98 eV (626.3 nm) and 2.09 eV (593.3 nm), respectively. The 6H-mc on the other hand, only has one contribution at 2.08 eV. The 2.08~2.09 eV emission observed in both samples should be of the same origin. It has been reported that bulk 6H-SiC emits weak photoluminescence at wavelength around 600 nm [14,15]. In our case, the 2.09 eV emission can be similarly assigned to the bulk defect, since this emission is independent of crystal sizes beyond nanoscale. The 1.98 eV emission, observed only from 6H-pd, can be attributed to surface states, as the 6H-pd has a larger surface-to-volume ratio due to a smaller crystal size. This notion will be further advanced by the PLY-XANES discussed below. XEOL with excitation energy below the edges yields similar spectral profiles albeit with different intensities (not shown). In the following, the analysis is focused on luminescence at the Si K-edge since the spectra can be interfered by the presence of carbon impurities while looking at C K-edge.

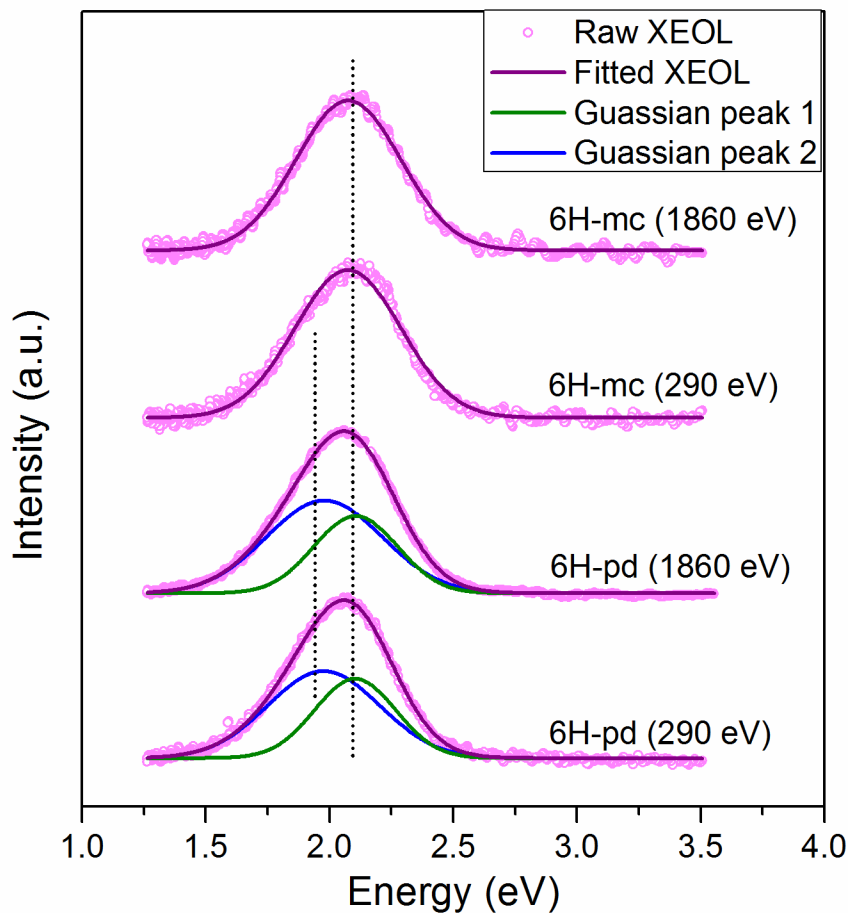


Figure 5-9 Normalized XEOL of 6H-mc and 6H-pd with excitation photon energy above the Si K- and C K-edge, respectively.

Figure 5-10 shows the PLY of 6H-mc and 6H-pd collected as total luminescence (zero order) with the excitation energy scanned stepwise across the Si K-edge, and the FY of the two samples are also included as the references. The PLY of 6H-mc displays all the characteristics of SiC FY, though inverted. We recall that in 6H-mc, there is only one contribution to the XEOL (Figure 5-9), thus the PLY-XANES tracks the intensity evolution of this 2.08 eV emission. The inversion of the PLY is caused by saturation

effect resulting from total absorption [42], which happens in the case of relatively thick samples.

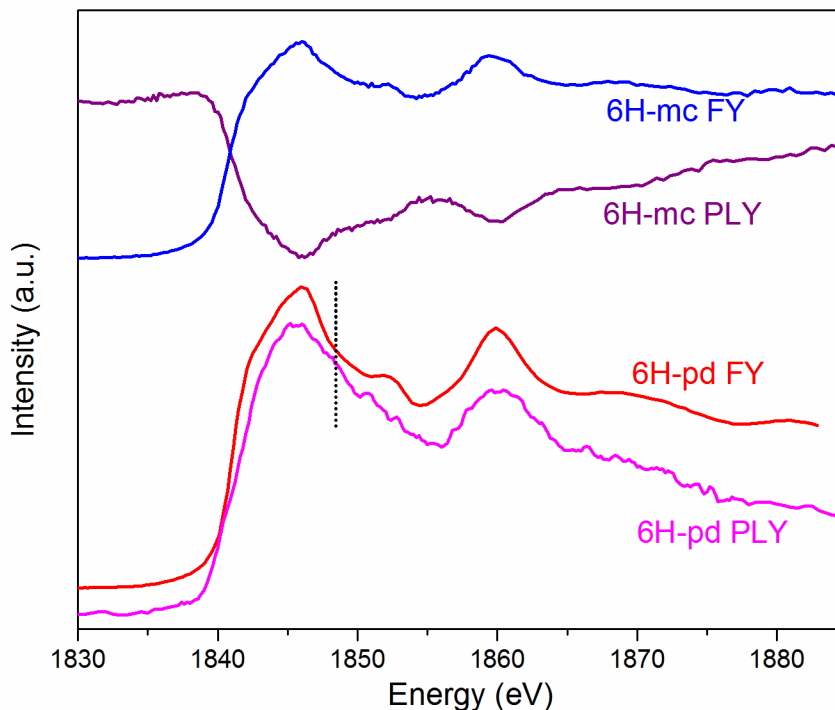


Figure 5-10 Si K-edge PLY and FY of 6H-mc and 6H-pd.

The PLY of 6H-pd, on the other hand, tracks the change of absorption coefficient across the Si K-edge. Since 6H-pd has a much smaller crystal size than 6H-mc, the saturation effect is negligible, yielding a normal PLY. Interestingly, however, aside from showing all the SiC resonance peaks, a weak shoulder, marked by the dotted line in Figure 5-10, is seen in PLY but not in FY. In addition, the peak at 1860 eV is slightly broader in PLY. These subtle differences in PLY are caused by luminescence from the SiO₂ channel, since the shoulder is at the same energy as the whiteline of SiO₂, and the broadening of the 1860 eV peak is due to the overlapping of SiC with SiO₂ multiple scattering peaks

(Figure 5-5(a)). Although the SiO₂ features are not apparent in the XANES of 6H-pd, its presence, most likely on the surface, can be revealed in the PLY-XANES if the optical decay in the SiO₂ channel is intense and efficient. The XEOL spectra shown in Figure 5-9 also indicate that there are two emission bands in the 6H-pd sample. The 2.09 eV emission is of the same origin as 6H-mc, and the 1.98 eV emission could be of an oxide origin.

5.3.2.2 XEOL of 3C-SiC

The XEOL of the three 3C-SiC samples under excitation energy at 1860 eV and 290 eV are shown in Figure 5-11. It can be seen that in each 3C-SiC sample, the luminescence from both Si K-edge and C K-edge are quite similar with only slight differences in the branching ratio. Unlike the bright luminescence from 6H-SiC, 3C-pd only emits weak light upon excitation and the signal to noise ratio is relatively large. The luminescence spectrum shows a broad peak which can be fitted with two Gaussian peaks centering at 2.07 eV (599nm) and 2.75 eV (451 nm). The 2.07 eV emission is very similar to the one observed from 6H-pd and 6H-mc (Figure 5-9), hence this emission band is not only independent of crystal sizes but also of crystal phases, and can be assigned to the defect from the bulk SiC. The 2.75 eV emission, observed in the 3C-SiC, shows different intensity ratios to the 2.07 eV emission at Si K-edge and C K-edge, indicating the 2.75 eV band is sensitive to the specific core-electron de-excitation channel.

The luminescence from 3C-cs and 3C-nw exhibit similar spectra: an asymmetric peak with highest intensity at 2.65 eV (468 nm). The Gaussian fit shows that for 3C-cs, the luminescence is composed of a broad peak at 2.44 eV (508 nm), a relatively sharp peak at 2.70 eV (459 nm) and a very weak peak at 3.30 eV (375 nm). The intensity of the 3.30

eV peak increases slightly when excited above the C K-edge. The first two emission bands are also found at the same location for 3C-nw, but the intensity of the 2.70 eV peak drops. Meanwhile, no 3.30 eV emission is observed at either the Si K- or C K-edge.

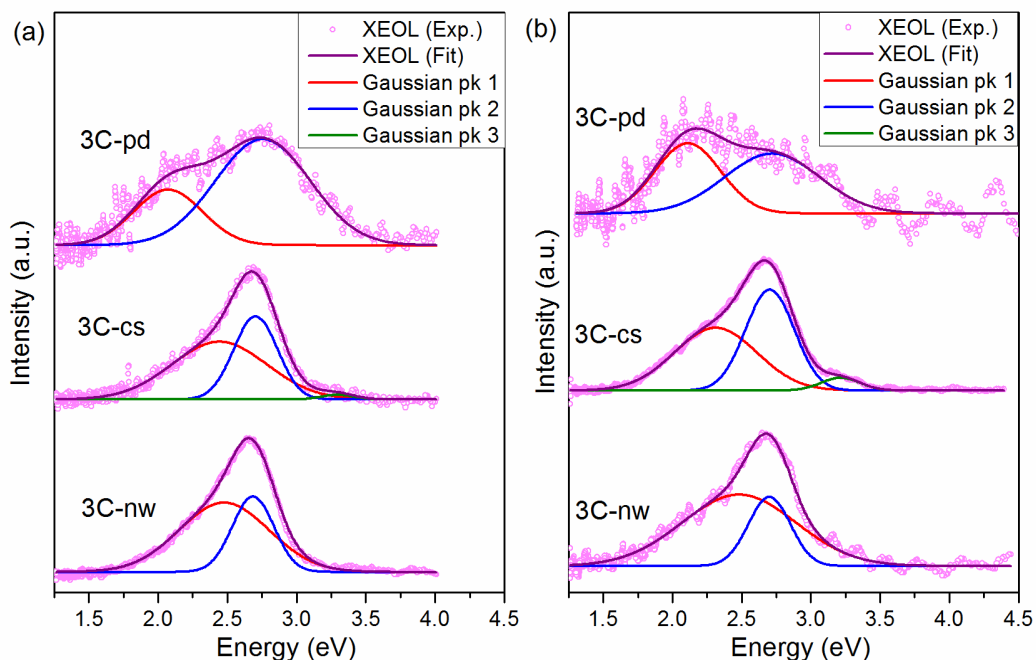


Figure 5-11 Normalized XEOL of 3C-pd, 3C-cs and 3C-nw with Gaussian fittings under excitation energy at (a) 1860 eV and (b) 290 eV.

Since the luminescence from 3C-SiC covers a broad range of wavelengths and the shoulder is distinguishable from the main peak, it is desirable to track the XANES with partial luminescence yield to enhance the site specificity. Due to the weak luminescence intensity, instead of measuring the PLY XANES by continuously scanning the energy, the partial PLY was obtained, one point at a time, according to the fitted peak areas in the XEOL spectra recorded at the selected energies.

Let us first look at the PLY XANES of 3C-pd, shown in Figure 5-12, where the spectra were collected at zero-order (total), the 2.75 eV emission and the 2.07 eV emission respectively. Although the luminescence intensity is weak, the zero-order PLY shows similar resonance as TEY, i.e. the 1842 eV edge jump, the main peak at 1846 eV, and another peak at 1860 eV. The 2.07 eV PLY clearly follows the same trend as the total PLY as well as the TEY-XANES across the edge. The 2.75 eV emission however, exhibit a shoulder at 1845 eV and then a peak maximum at 1848 eV. It suggests that SiO₂ involves the luminescence at this region, and the emission could be attributed to the localized defect on the SiO₂-SiC interface. In fact, the emission at 2.75 eV has also been observed from 3C-SiC particles in Si_{1-x}C_x:H matrix [43], and was attributed to emission from defect states on the surface. The 3C-SiC has larger surface area compared to 6H-SiC and could get oxidized more easily; hence there is a noticeable oxide contribution to the PLY-XANES.

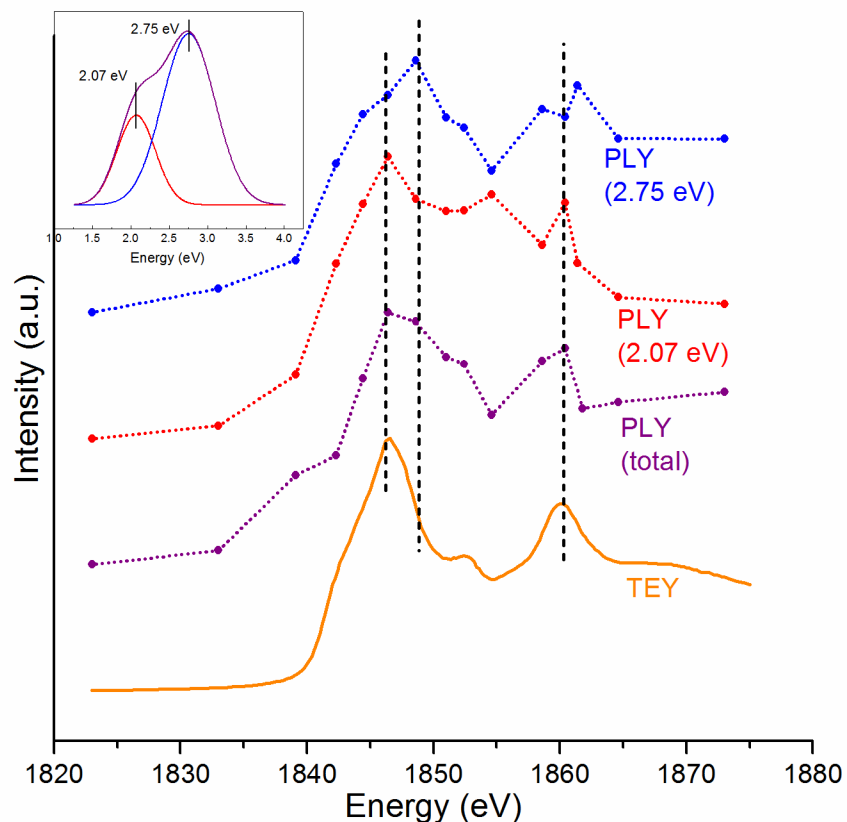


Figure 5-12 Wavelength selected PLY of 3C-pd, in which the intensity of fitted emission peaks (by peak areas) is plotted against the excitation energy, and the TEY of 3C-pd is shown as reference. XEOL with fitted peaks is shown in inset.

Figure 5-13 shows the PLY-XANES of the core-shell nanowires 3C-cs and the HF-treated nanowires 3C-nw. Luminescence at the three sub-regions were plotted for 3C-cs, shown in Figure 5-13(a). It can be seen from zero order PLY that 3C-cs shows an increase in luminescence intensity as the excitation energy approaches the Si K-edge, followed by small variations above the edge and a broad peak at higher energy (i.e. ~1860 eV). Since there is a competition for the incoming photon between the co-existence of SiC and SiO₂, TEY (and FY) shows combined features from the two

components. The 2.44 eV partial PLY, however, only exhibits features that belong to SiC. The 2.70 eV PLY, on the other hand, shows mixed features of both SiC and SiO₂, but the latter dominates. Since the 2.70 eV emission is commonly observed from Si and SiO₂ nanostructures, and as discussed in depth in Chapter 4, it is assigned to emission from the SiO₂ in which Si is in an oxygen deficient environment. In this case, the 2.70 eV emission observed in the core-shell 3C-cs could be of the similar origin, since 3C-cs is covered by a thick oxide shell.

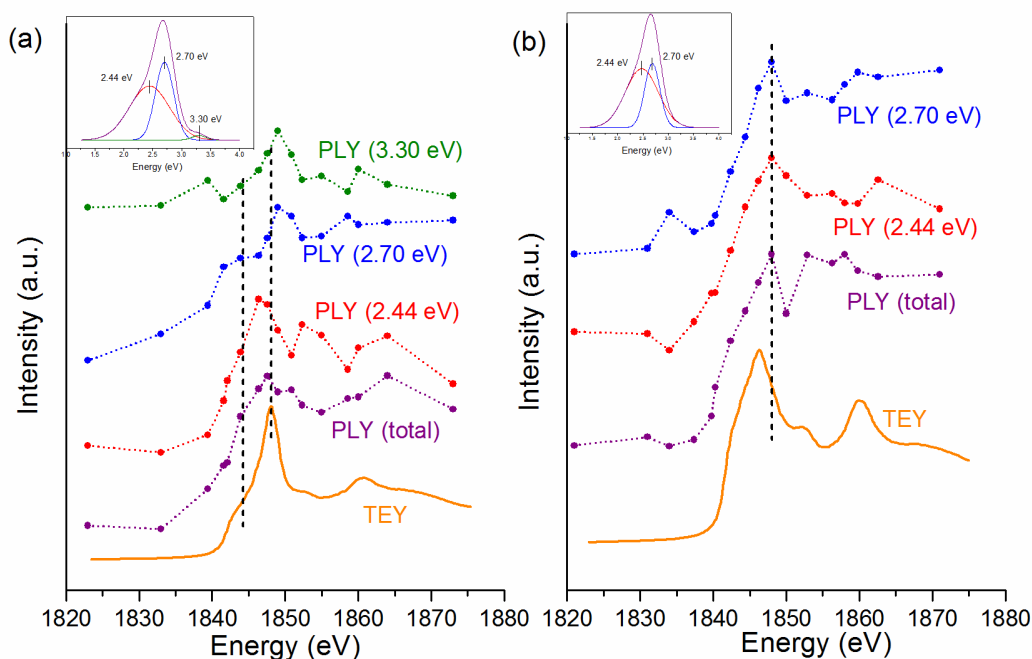


Figure 5-13 Region selected PLY of (a) 3C-cs and (b) 3C-nw. The insets show the XEOL spectra with fitted peaks.

The 2.44 eV emission can be attributed to SiC nanowires due to quantum confinement. Using the effective mass approximation, the band gap of semiconductor clusters E_g^* can be described as a function of particle radius as follows [44]:

$$E_g^* = E_g + \frac{\hbar^2 \pi^2}{2R^2} \left[\frac{1}{m_e} + \frac{1}{m_h} \right] - \frac{1.8e^2}{4\pi\epsilon_0\epsilon R} \quad (5.1)$$

In the case of 3C-SiC, E_g is the band gap (2.36 eV), R is the size of nano SiC (e.g. 5 nm), ϵ is the dielectric constant of 3C-SiC (9.72) [11], m_e and m_h are the mass of the electron and hole, respectively, which makes the reduced mass of the electron-hole pair (exciton). For 3C-SiC, $m_e=0.394m_0$ and $m_h=0.387m_0$ is used while m_0 is the mass of free electron [45]. The band gap thus calculated for SiC nanowires is 2.38 eV, which is very close to the observed 2.44 eV. However, from the observed TEM image, SiC nanowires exhibit much large diameters. This 2.44 eV emission hence could be attributed to embedded SiC nanocrystallites formed during the nanowires synthesis.

The 3.30 eV emission, though the intensity is fairly weak compared to the total luminescence, still shows optical response at the vicinity of Si K-edge. The PLY reaches its highest intensity after the SiO₂ channel turns on. Luminescence at shorter wavelength has been observed from photoluminescence spectrum of magnetron sputtered SiO₂ films annealed at high temperature [46] as well as thermally oxidized SiNW described in Chapter 3. We attribute the origin of the emission to the defect center in SiO₂.

The PLY of 3C-nw is shown in Figure 5-13(b). All three PLY spectra yield similar spectral profiles. They all show the characteristic, round rising edge of SiC, although the presence of SiO₂ whiteline is still noticeable. As shown in XEOL (Figure 5-11(b)), the intensity of the 2.70 eV emission decreases considerably after HF treatment, and two Gaussian fit peaks are mostly overlapping with each other. It is interesting to note that there is no SiO₂ features observed from TEY of 3C-nw, thus HF treatment removes most of the SiO₂ shell. However, the optical signal suggests that some surface oxide remains,

and the 2.70 eV is still the optically favored decay channel. The relative intensity of the 2.44 eV emission increases upon the removal the SiO₂ shell, and the 3.30 eV emission is no longer seen.

5.4 Conclusion

All SiC polytypes investigated here show similar near-edge structures at Si K- and C K-edges due to the same Si-C tetrahedral local structure. In comparison with the theoretical calculation using DFT, the calculated Si K-edge XANES show excellent agreement with the experimental results, but for the C K-edge, only semi-quantitative results are reproduced. The band gap differences between 3C-SiC and 6H-SiC are revealed by C K-edge XANES calculation. As for the core-shell SiC nanowires, XANES reveals a combined feature from SiC and SiO₂ at Si K-edge, and upon SiO₂ shell removal, only the SiC signal from the core persists. Both XRD and XANES results confirm that SiC nanostructure is stable as 3C-phase. It is also found that SiC emits light at different wavelengths ranging from 375 nm to 700 nm depending on the crystal structures and the morphologies. But for the same sample, luminescence exhibits similar profile upon excitation at different edge energies, showing only slight variations in the relative peak intensities.

The 2.07 eV luminescence can be observed from all SiC crystallines regardless of polytypes and crystal sizes. The origin of this emission is attributed to the SiC bulk defect. For 6H-pd, an additional defect luminescence band at 1.98 eV is observed and attributed to surface state upon the formation of surface native oxide. 3C-SiC emits much weaker luminescence under X-ray excitation. Luminescence from 3C-pd is composed of two emission bands: one is from bulk defect of SiC (2.07 eV), similar to 6H-SiC, and the

other 2.75 eV is from SiO₂. Three contributions are found in core-shell nanowires: the 2.70 eV and 3.30 eV are from SiO₂-SiC interface and defect in SiO₂, respectively, and the 2.44 eV emission is from quantum-confined SiC. After SiO₂ shell removal, the 3.30 eV emission disappeared, and SiC-nw shows quantum-confined 2.44 eV emission. The 2.70 eV emission remains, but of much less intensity, which are originated from the interface between the SiC core and SiO₂ residue.

5.5 References

- [1] Harris, C. I.; Savage, S.; Konstantinov, A.; Bakowski, M.; Ericsson, P., *Appl. Surf. Sci.* **2001**, *184*, 393-398.
- [2] Nakamura, D.; Gunjishima, I.; Yamaguchi, S.; Ito, T.; Okamoto, A.; Kondo, H.; Onda, S.; Takatori, K., *Nature* **2004**, *430*, 1009-1012.
- [3] Goldberg, Y.; Levinshtein, M.; Rumyantsev, S., *Properties of advanced semiconductor materials: GaN, AlN, InN, BN, SiC, SiGe*. Wiley: New York, 2001.
- [4] Bhatnagar, M.; Baliga, J., *IEEE Trans.* **1993**, *40*, 645-55.
- [5] Zhou, W.; Yan, L.; Wang, Y.; Zhang, Y., *Appl. Phys. Lett.* **2006**, *89*, 013105/1-013105/3.
- [6] Park, C. H.; Cheong, B.-H.; Lee, K.-H.; Chang, K. J., *Phys. Rev. B* **1994**, *49*, 4485-93.
- [7] Persson, C.; Lindefelt, U., *J. Appl. Phys.* **1997**, *82*, 5496.
- [8] Bernstein, N.; Gotsis, H. J.; Papaconstantopoulos, D. A.; Mehl, M. J., *Phys. Rev. B* **2005**, *71*, 075203/1-075203/11.

- [9] Kackell, P.; Wenzien, B.; Bechstedt, F., *Phys. Rev. B* **1994**, *50*, 10761.
- [10] Fan, J. Y.; Wu, X. L.; Chu, P. K., *Prog. Mater. Sci.* **2006**, *51*, 983-1031.
- [11] Choyke, W. J.; Patrick, L., *Phys. Rev. B* **1970**, *2*, 4959-65.
- [12] Ikeda, M.; Matsunami, H.; Tanaka, T., *Phys. Rev. B* **1980**, *22*, 2842-54.
- [13] Matsumoto, T.; Takahashi, J.; Tamaki, T.; Futagi, T.; Mimura, H., *Appl. Phys. Lett.* **1994**, *64*, 226-8.
- [14] Petrova-Koch, V.; Sreseli, O.; Polisski, G.; Kovalev, D.; Muschik, T.; Koch, F., *Thin Solid Films* **1995**, *255*, 107-10.
- [15] Jessensky, O.; Mueller, F.; Goesele, U., *Thin Solid Films* **1997**, *297*, 224-228.
- [16] Konstantinov, A. O.; Henry, A.; Harris, C. I.; Janzen, E., *Appl. Phys. Lett.* **1995**, *66*, 2250-2.
- [17] Guo, Y. P.; Zheng, J. C.; Wee, A. T. S.; Huan, C. H. A.; Li, K.; Pan, J. S.; Feng, Z. C.; Chua, S. J., *Chem. Phys. Lett.* **2001**, *339*, 319-322.
- [18] Zhao, J.; Mao, D. S.; Lin, Z. X.; Jiang, B. Y.; Yu, Y. H.; Liu, X. H.; Wang, H. Z.; Yang, G. Q., *Appl. Phys. Lett.* **1998**, *73*, 1838-1840.
- [19] Seong, H.-K.; Choi, H.-J.; Lee, S.-K.; Lee, J.-I.; Choi, D.-J., *Appl. Phys. Lett.* **2004**, *85*, 1256-1258.
- [20] Niu, J. J.; Wang, J. N., *J. Phys. Chem. B* **2007**, *111*, 4368-4373.
- [21] Rebohle, L.; Gebel, T.; Frob, H.; Reuther, H.; Skorupa, W., *Appl. Surf. Sci.* **2001**, *184*, 156-160.
- [22] Zhou, W.; Liu, X.; Zhang, Y., *Appl. Phys. Lett.* **2006**, *89*, 223124.
- [23] Regier, T.; Paulsen, J.; Wright, G.; Coulthard, I.; Tan, K.; Sham, T. K.; Blyth, R. I. R., *AIP Conf. Proc.* **2007**, *879*, 473

- [24] Momma, K.; Izumi, F., *J. Appl. Crystallogr.* **2008**, *4*, 653-658.
- [25] Hohenberg, P.; Kohn, W., *Phys. Rev.* **1964**, *136*, B864-B871.
- [26] Kohn, W.; Sham, L. J., *Phys. Rev.* **1965**, *140*, A1133-A1138.
- [27] Perdew, J. P.; Chevary, J. A.; Vosko, S. H.; Jackson, K. A.; Pederson, M. R.; Singh, D. J.; Fiolhais, C., *Phys. Rev. B* **1992**, *46*, 6671-87.
- [28] Blaha, P.; Schwarz, K., *J. Phys. F* **1987**, *17*, 899-911.
- [29] Blaha, P.; Schwarz, K.; Sorantin, P.; Trickey, S. B., *Comput. Phys. Commun.* **1990**, *59*, 399-415.
- [30] Wyckoff, R. N. G., *Crystal Structure*. John Wiley & Sons: New York, 1963; Vol. 1.
- [31] Rohrer, G. S., *Structure and Bonding in Crystalline Materials*. Cambridge University Press: Cambridge, 2001.
- [32] Blochl, P. E.; Jepsen, O.; Andersen, O. K., *Phys. Rev. B* **1994**, *49*, 16223-33.
- [33] Fuggle, J. C.; Inglesfield, J. E., *Unoccupied Electronic States: Fundamentals for XANES, EELS, IPS and BIS*. Springer-Verlag: New York, 1992; Vol. 69.
- [34] Prado, R. J.; D'Addio, T. F.; Fantini, M. C. A.; Pereyra, I.; Flank, A. M., *J. Non-Cryst. Solids* **2003**, *330*, 196-215.
- [35] Chang, Y. K.; Hsieh, H. H.; Pong, W. F.; Tsai, M. H.; Dann, T. E.; Chien, F. Z.; Tseng, P. K.; Chen, L. C.; Wei, S. L.; Chen, K. H.; Wu, J. J.; Chen, Y. F., *J. Appl. Phys.* **1999**, *86*, 5609-5613.
- [36] Baba, Y.; Sekiguchi, T.; Shimoyama, I.; Nath, K. G., *Appl. Surf. Sci.* **2004**, *237*, 176-180.
- [37] X-ray Calculator: http://henke.lbl.gov/optical_constants

38. Kim, P. S. G.; Tang, Y. H.; Sham, T. K.; Lee, S. T., *Can. J. Chem.* **2007**, *85*, 695-701.
- [39] Pong, W. F.; Yueh, C. L.; Chang, Y. D.; Tsai, M. H.; Chang, Y. K.; Chen, Y. Y.; Lee, J. F.; Wei, S. L.; Wen, C. Y.; Chen, L. C.; Chen, K. H.; Lin, I. N.; Cheng, H. F., *J. Synchrotron Radiat.* **2001**, *8*, 145-9.
- [40] Charging at very intense light source can be a problem for recording XANES of non-conducting materials in the TEY mode. This problem can be minimized by reducing the flux with filters and increasing the dead time between steps. In the case, our samples are thin enough so that FY, which is less susceptible to charging, is used for the analysis.
- [41] McMaster, W. H., *Compilation of X-ray cross sections*. UCRL: 1969.
- [42] Sham, T. K.; Coulthard, I., *J. Synchrotron Radiat.* **1999**, *6*, 215-216.
- [43] Wu, X. L.; Siu, G. G.; Stokes, M. J.; Fan, D. L.; Gu, Y.; Bao, X. M., *Appl. Phys. Lett.* **2000**, *77*, 1292-1294.
- [44] Brus, L., *J. Phys. Chem.* **1986**, *90*, 2555-60.
- [45] Wu, X. L.; Fan, J. Y.; Qiu, T.; Yang, X.; Siu, G. G.; Chu Paul, K., *Phys. Rev. Lett.* **2005**, *94*, 026102.
- [46] Song, H. Z.; Bao, X. M.; Li, N. S.; Wu, X. L., *Appl. Phys. Lett.* **1998**, *72*, 356-358.

Chapter 6

6 XANES and XEOL Studies of Boron Nitride Nanotubes

6.1 Introduction

Boron nitride has crystal structure similar to its isoelectronic carbon system. The B and N atoms can be either sp^3 hybridized, forming a cubic crystal structure similar to diamond, or they can be sp^2 hybridized, forming a hexagonal crystal structure which resembles graphite. Boron nitride nanotubes (BNNT) henceforth can be considered as a structural analogue of carbon nanotubes, in which layered hexagonal BN (hex-BN) sheets are rolled into cylinders. The possibility of the formation of BNNT was first predicted theoretically by Rubio *et al* in 1994 [1] and a year later BNNT was successfully synthesized using an arc discharge technique [2]. Since then extensive researches have been carried on developing synthesis techniques and investigating the chemical and physical properties of such materials [3-5].

BNNT is found having a constant indirect band gap of 5.5 eV regardless of nanotube morphology (e.g. diameters, helicity, etc.) [6]. Under external excitation by laser (as in photoluminescence, PL) or electrons (as in cathodoluminescence, CL), valence electrons in BN are promoted into the conduction band, and the recombination of an electron-hole pair near the band-gap (exciton) results in luminescence at 5-6 eV [7-10]. Apart from the near band-gap luminescence, which usually takes place at low temperature, room temperature luminescence measurements usually show that BN has visible light emission

* A version of this chapter has been published in *ACS Nano*, **2011**, 5,631

dominated at violet-blue [9,11]. Such luminescence has been attributed to the presence of structural defects or impurities being introduced during sample synthesis. In fact, in most cases, the luminescence spectra cover a broad wavelength region and have various features depending on the excitation source and the morphology of the materials [9-14]. It is also found that the violet-blue emission usually exhibits equally spaced sharp multiplets, especially at low temperature, which are due to the coupling between electrons and phonons (phonon replica) [9,11,14]. Since the luminescence at this region has a complex origin, and the conventional PL or CL only measures luminescence spectra using a constant excitation energy without site or element specificity, it is desirable to find out which element, or the element in what local environment, could produce luminescence at certain wavelengths.

The isotope effect of B on the structures and properties of BNNT is also worth investigating. B has two types of stable isotopes: ^{11}B and ^{10}B . The natural occurrence of B is 80% of ^{11}B and 20% of ^{10}B . Previously, Han *et al.* have successfully synthesized BNNT containing pure ^{10}B using a metal-assisted chemical synthetic route in comparison with BNNT made via the same route but containing natural B [15,16]. They found that BNNT made with natural B and pure ^{10}B have different phonon-electron coupling mechanism as revealed by Raman and infrared spectroscopy, and the CL measurements also showed that two BNNT samples exhibit different luminescence properties [15].

In this chapter, the correlation between luminescence and the electronic structures of BNNT made with natural B as well as ^{10}B are studied using X-ray absorption near-edge structures (XANES) and X-ray excited optical luminescence (XEOL). The electrons at specific core levels are selectively excited using tunable X-rays and the accompanying

luminescence during de-excitation is monitored while the photon energy is scanned across an absorption threshold of the element of interest. It is found that under X-ray excitation, BN emitted bright violet-blue light with unique features depending on the electron structures of the samples. The implications of the findings are discussed.

6.2 Experimental

The multiwalled BNNT was provided by Dr. Weiqiang Han, Center for Functional Nanomaterials, Brookhaven National Laboratory. The details of the synthesis have been described elsewhere [16,17]. In brief, the BNNT were prepared by reacting B powders with a mixture of MgO and SnO as precursors under an ammonia atmosphere. Isotope-substituted BNNT were synthesized following the same route, but natural B powder was replaced with ^{10}B powders. Both BNNT samples have similar morphologies: 20-100 nm in diameter and several tens of micrometers in length, with wall numbers typically of tens. Figure 6-1 shows a transmission electron microscopy (TEM) image of an individual BNNT made with natural B, and it can be seen that the nanotube has a diameter of 25 nm and a wall thickness of 10.2 nm. The natural BNNT are henceforth denoted as “nat-BNNT” and BNNT with isotope ^{10}B are denoted as “ ^{10}B -BNNT”. B_2O_3 powder (Sigma Aldrich) and hexagonal BN powder (Alfa Aesar) were used as references. The latter is denoted as “hex-BN”.

Synchrotron radiation measurements were carried out at the Canadian Light Source (CLS). The B K-edge measurements were performed at the VLS-PGM beamline and the N K- and O K-edge measurements were conducted at the SGM beamline [18,19]. The samples were measured in both total electron yield (TEY) and X-ray fluorescence yield

(FY) for XANES. XEOL and PLY were measured where applicable. All spectra are normalized to the incident photon flux (I_0).

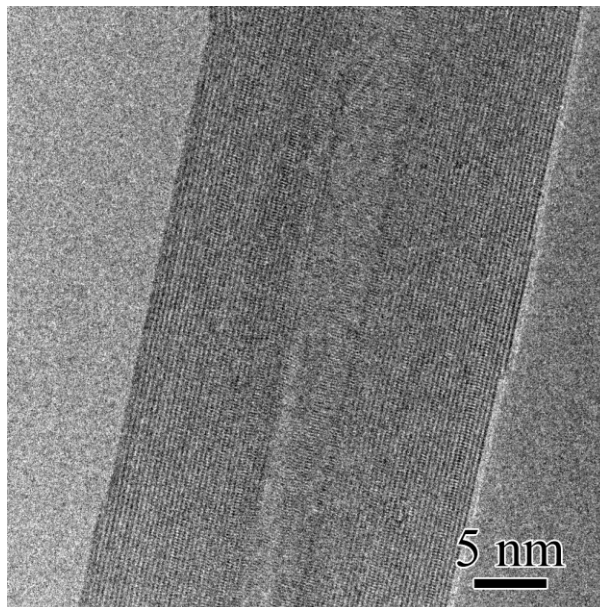


Figure 6-1 TEM image of an individual nat-BNNT.

6.3 Results and Discussion

6.3.1 Electronic Structure of BN

Figure 6-2 shows the XANES spectra of hex-BN, nat-BNNT, 10-BNNT and B_2O_3 at the B K-edge. All spectra are normalized to the unit edge jump and shifted vertically for clarity. The spectra display several sharp peaks that can be categorized into two groups, labeled by dashed lines as A and B in the figure. The A-series belongs to B in a B-N local environment, which show characteristic features of the sp^2 hybridized B-N system. The intense peak A_1 at 192 eV is the B $1s$ to π^* transition, and the doublet A_2 and A_3 , at energy 198.2 eV and 199.5 eV, respectively, are from the B $1s$ to σ^* transition [20]. The A-series peaks are clearly seen in both TEY and FY of hex-BN. The B-series, on the

other hand, is the characteristic spectral signature of B in a B-O local environment. As seen in XANES of B_2O_3 , both TEY and FY show a sharp π^* peak B_1 at 194 eV and a broad σ^* resonance B_2 centered at 203 eV.

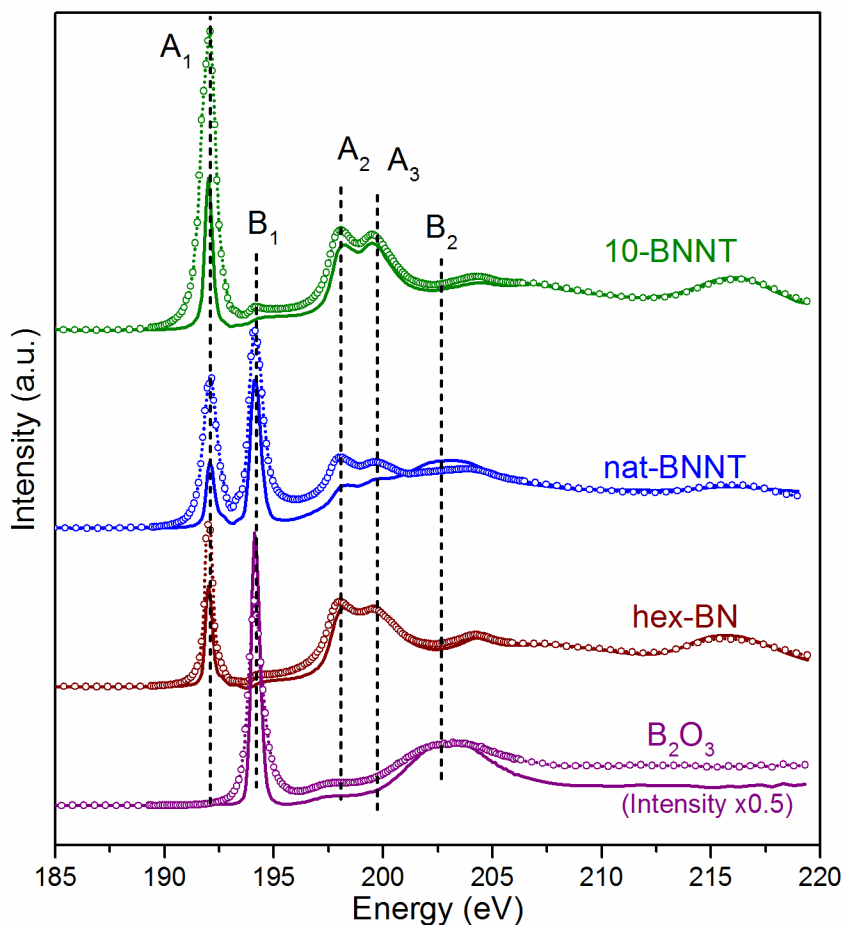


Figure 6-2 XANES of hex-BN, nat-BNNT, 10-BNNT and B_2O_3 . Solid lines: TEY, open circles: FY. The spectra are normalized to unit edge jump, and the intensity of B_2O_3 TEY is decreased by half to fit in the scale.

It should be noted that B_2O_3 has a complex structure. Under ambient condition, it is generally considered as a glassy form (vitreous B_2O_3) which contains B and O atoms in

two types of arrangements [21], illustrated in Figure 6-3. In the first structure, each B atom is triangularly surrounded by three O atoms and each O atom is bonded to two B atoms. In the second structure, the B and O atoms form boroxol group as a B_3O_6 unit, which consists of a hexagonal ring of three B and three O with another three O shared atoms outside the ring. However, both structures contribute to the B K-edge XANES similarly, since for B the local environment are similar.

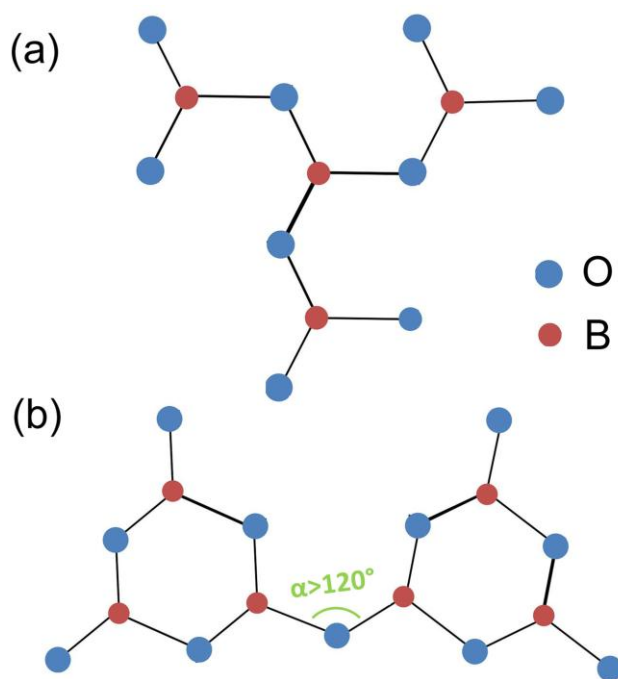


Figure 6-3 Two structure models of B_2O_3 . Oxygen atoms are in blue, and boron atoms are in red.

Back to the XANES of the nanotube samples, the peaks belonging to B-N bonding (A-series) are clearly seen in the two BNNT samples, which confirm that the nanotubes are of hexagonal B-N structures. In fact, 10-BNNT shows pure B-N features in TEY and FY spectra, which resembles the XANES of hex-BN. In nat-BNNT, however, both A-series

and B-series can be seen, indicating that nat-BNNT contains both B-N bonding and B-O bonding. In TEY, peak B₁ from B-O local environment is the most intense feature, and the doublet A₂ and A₃ from B-N is buried under the broad B₂ resonance. The relative intensity of A₁ increases in FY spectrum, but still less intense than the B₁ peak. This observation indicates that the nat-BNNT sample contains oxide in which O atoms are bond to B forming structures similar to B₂O₃.

It can also be seen that in the FY of both nanotubes samples, the π^* transition peak (peak A₁) is broadened compared to the one in TEY, but the broadening is less obvious for bulk hex-BN. The peak broadening can be attributed to the removal of the degeneracy of the π^* band as the overlapping of p_z orbitals in nanotubes is increased due to the small tube curvature [22]. Similar phenomenon has also been observed from carbon nanotubes [23]. The multiwalled nanotube structure creates differences in the outer and inner tube diameters, and the fact that only FY shows peak broadening means that a stronger curvature effect takes place at the inner side of the nanotubes. It is also interesting to note that the FY of the nanotubes shows a larger π^*/σ^* ratio, in other words, peak A₁ is more intense than A₂ and A₃ in FY relative to TEY. This is because the TEY signal mostly comes from the sample surface, where the B-N plane is less constrained and more susceptible to ambient gas adsorption, whereas FY is able to probe inner tubes with increasing constrains.

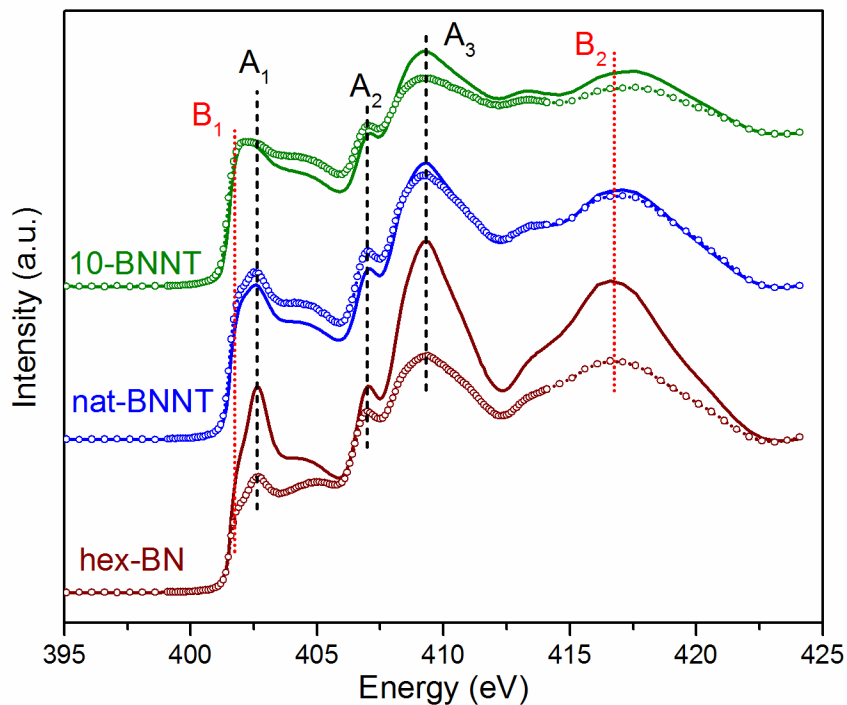


Figure 6-4 XANES of hex-BN, nat-BNNT and 10-BNNT at the N K-edge. Solid lines: TEY, open circles: FY.

The N K-edge TEY and FY-XANES of hex-BN, nat-BNNT and 10-BNNT are shown in Figure 6-4. The spectra of the three samples share several features in common, marked by dashed lines in black (the A-series) in the figure. The sharp peak A₁ at 402.6 eV is the N 1s to π^* transition peak, and two oscillations A₂ (407 eV) and A₃ (409.2 eV) belong to the N 1s to σ^* transition [24]. The FY of hex-BN displays a similar profile as the TEY but the features are broadened due to self-absorption, whereas in the two BNNT samples, such discrepancy between TEY and FY is less obvious.

Although the N K-edge XANES of BNNT exhibit a similar spectral profile as their bulk counterpart, there are still a couple of subtle differences to be noted. Firstly, the shoulder feature B₁ at 402.1 eV marked by a red dotted line in the figure, becomes more intense in

nanotube samples. In 10-BNNT, the intensity of the B_1 feature is comparable to the main A_1 peak. The occurrence of the shoulder feature at energy 0.5 eV below the main N 1s to π^* transition has also been observed from other BN nanostructures [25,26], but no conclusive explanation has been given. The difference between A_1 and B_1 in BNNT and hex-BN can be considered as a peak broadening of the A_1 (π^*) peak. In such a case, it can be explained as a decrease of N π^* density of states due to the overlapping of N p_z orbitals (curvature effect) [22,25]. The second difference is the peak B_2 at 416.6 in hex-BN shifts to 417.0 eV in nat-BNNT and 417.2 eV in 10-BNNT. The origin of B_2 is the multiple scattering. The distance between B and N in BNNT are likely smaller than that in bulk hex-BN due to the contraction of the BN lattice, hence B_2 peak shifts to higher energy.

The above observations in Figure 6-2 and Figure 6-4 show that, although synthesized via the same route, BNNT prepared with natural B and ^{10}B differ in purity. The 10-BNNT has no noticeable oxide impurities, whereas nat-BNNT is rich in surface oxide forming B-O bonding. The presence of oxide however, has little effect on the conduction band modification at the N K-edge. The reason for this is not entirely clear and may be due to kinetics, which segregates the N from the B-O interaction. As the proposed reaction mechanism for BNNT synthesis involves the formation of the B_2O_2 molecule [16], which may further grow into a B_nO_m cluster. A recent calculation also indicates that the O atoms could interact with B forming a B-O ring structure similar to the structure of B_2O_3 (Figure 6-3(b)) and substituting the B-N network [27].

6.3.2 Luminescence From BN

Figure 6-5 shows the XEOL spectra with selected excitation energies from below to above the B K-edge. The XEOL excited at the N K-edge has the same profile thus not shown. It can be seen that the luminescence from hex-BN covers a broad wavelength range: the highest emission intensity is located at near-UV region between 3.75 eV and 4.09 eV; a second emission band in the visible violet region at 3.20 eV (387.5 nm) of lower intensity, appears as a shoulder to the main emission peak. The luminescence intensity is high under excitation both below (190 eV) and far above (203 eV) the B K-edge, but decreases drastically at the edge resonance (192 eV), leading to an inversion. If we take a closer look at the main emission peak, we can clearly see that the peak is composed of three oscillations at 3.98 eV (311.5 nm), 3.87 eV (320.4 nm), and 3.77 eV (328.9 nm). These oscillations are associated with lattice vibrations of the B-N network (i.e. emission with the assistance of phonons) [28]. Similar results on hexagonal BN crystals have been observed using photoluminescence (PL) and cathodoluminescence (CL) [9,29]. The intervals between the luminescence peaks are caused by energy dissipation of the B-N A_{2u} and E_{1u} vibration bands of $\sim 800\text{ cm}^{-1}$ and $\sim 1400\text{ cm}^{-1}$, which are equivalent to energy of 0.10 eV and 0.17 eV, respectively. Such vibration bands are the characteristic feature in infrared spectrum of BN [15,30,31]. It should also be noted that, although the intensity of the luminescence varies with different excitation energies, the relative intensity ratio of the near-UV and the violet luminescence remains the same. Shown in Figure 6-4(c), the XEOL spectra are normalized to the intensity of the 3.98 eV peak, and it can be seen that the overall profile of XEOL spectrum is essentially identical

to each other, indicating that the two emission bands may have a similar luminescence mechanism.

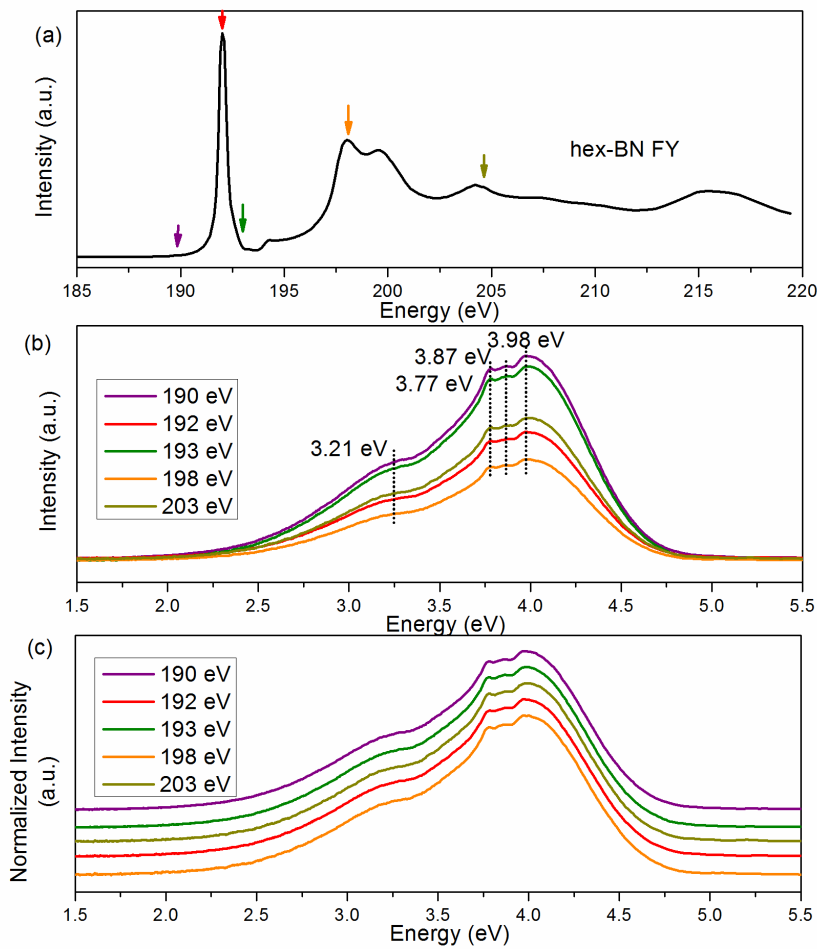


Figure 6-5 (a) FY-XANES of hex-BN with arrows indicating the energies at which XEOL spectra in (b) are obtained. (b) XEOL spectra of hex-BN at selected energies from below to above the B K-edge after normalization to I_0 . (c) XEOL spectra of hex-BN after normalization to the most intense emission peak and being shifted vertically for clarity.

We now turn to discuss the variation of luminescence intensity across the absorption edge. Figure 6-6 shows the PLY spectra of hex-BN with the excitation energy scanned

across the B K- and N K-edges in comparison with the XANES spectra recorded in TEY and FY. The zero-order PLY at both B K- and N K-edges show all the resonances observed in XANES, but completely inverted. In other words, the luminescence from hex-BN decreases significantly once the photon energy is tuned to the absorption edge of the core electron. This means the luminescence intensity of hex-BN is sensitive to how the incoming photon is absorbed for both B and N. At energies below the edge, the absorption coefficient is relatively small, hence a longer attenuation length and only electrons at shallower levels (valence and shallow inner shell electrons) are able to be prompted to the unoccupied electronic states (continuum), and the electrons/holes will thermalize resulting in electron-hole recombination via the optical channel. Once the photon energy is tuned to the edge of the core electron, the penetration depth of the incident photon abruptly decreases due to a sudden change in the absorption coefficient [32]. The main fraction of the Auger electron and fluorescence X-rays that are responsible for producing secondary electron-hole pairs via thermalization can escape the solid without transferring the energy to the optical channel. The decrease in quantum yield of the optical photon is caused by the shortening of the probing depth at both edges, thus the observed luminescence from hex-BN is likely from the bulk defect in the crystal.

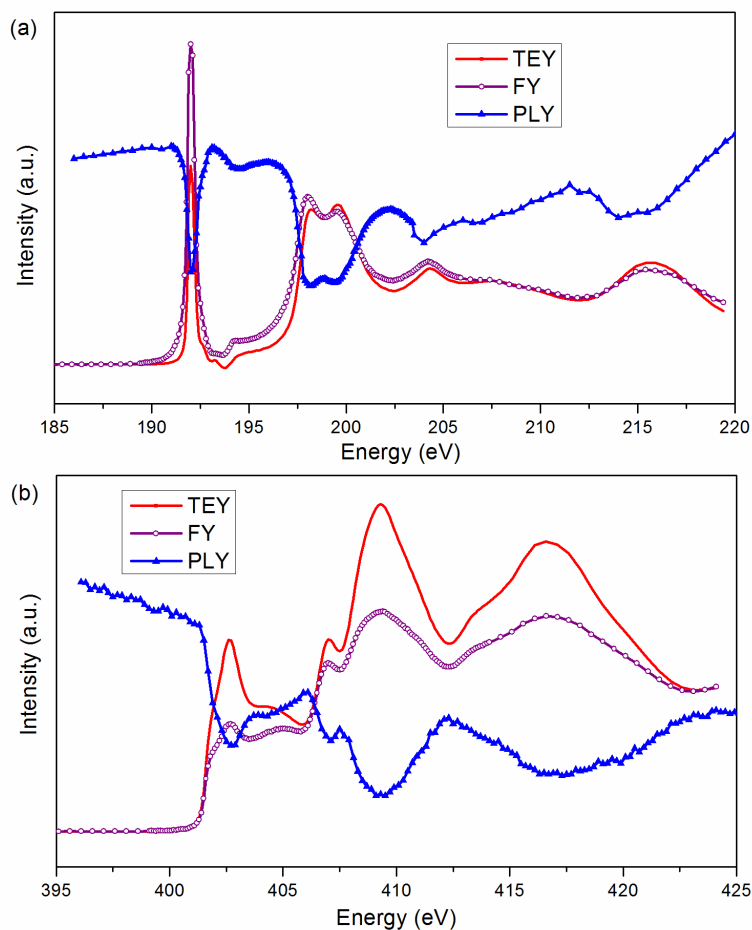


Figure 6-6 PLY (zero order)-XANES of hex-BN at (a) the B K-edge and (b) the N K-edge.

The XEOL spectra of nat-BNNT also exhibit two emission bands at near-UV and violet regions, but the spectral profiles differ significantly from those of hex-BN. Shown in Figure 6-7 (a), the XEOL spectra were obtained at energies selected from below to above the B K-edge, as indicated in Figure 6-7(b). The main emission is composed of two sharp features located at 4.05 eV (306.1 nm) and 3.89 eV (318.8 nm), a shoulder at 3.78 eV (328.0 nm), followed by several weak oscillations toward lower energy. A broad

emission at 3.08 eV (402.6 nm) can also be seen, similar to what is observed from hex-BN, but the intensity is much lower.

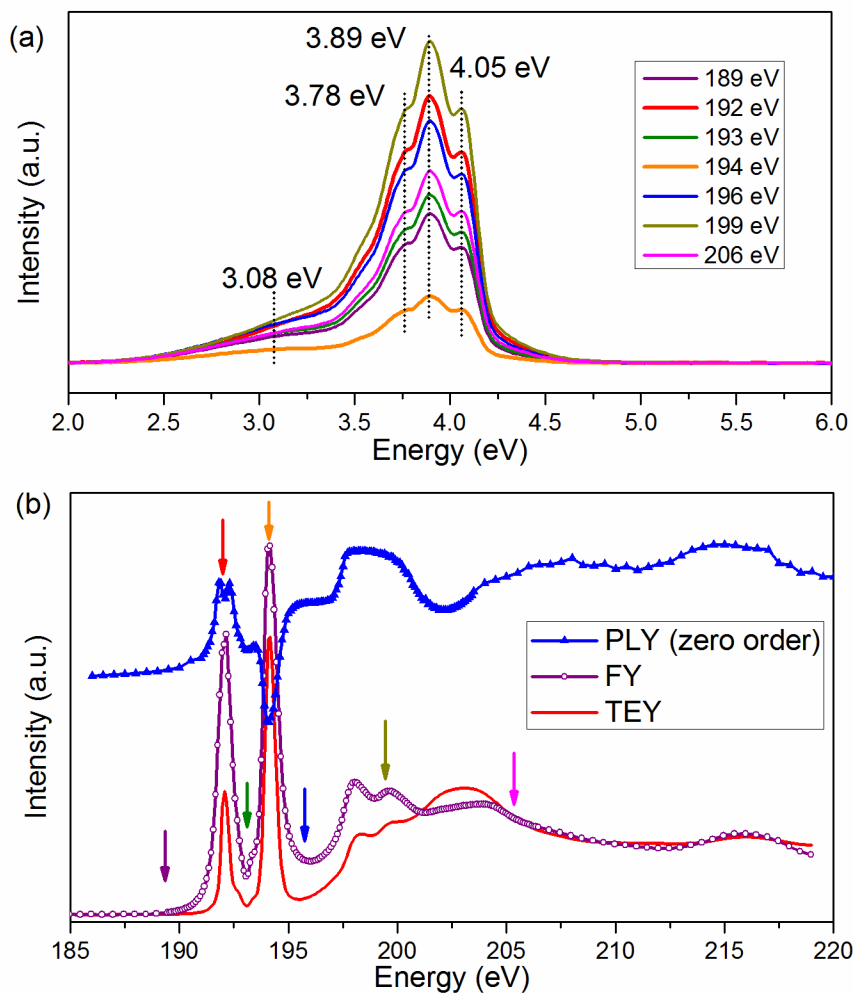


Figure 6-7 (a) XEOL spectra of nat-BNNT with selected excitation energies as indicated by arrows in (b). (b) PLY-XANES of nat-BNNT at the B K-edge in comparison with TEY and FY.

The total luminescence intensity varies while tuning the excitation energy across the edge. As discussed in the previous section, the B K-edge XANES spectrum of nat-BNNT

has both B-N and B-O contributions, hence the energies were selected where the characteristic absorption features appear. It can be seen in Figure 6-7(a), the XEOL intensity increases at the B-N absorption maximum (192 eV), whereas the minimum intensity of XEOL appears while the excitation energy is tuned to the B-O absorption peak (194 eV). This can be more readily seen from PLY-XANES, shown in Figure 6-7(b). Unlike the total inversion observed from PLY-XANES of hex-BN, in nat-BNNT, the B-N bonding contributed to the PLY positively, but the B-O bonding quenches the luminescence, shown as an inverted peak at 194 eV.

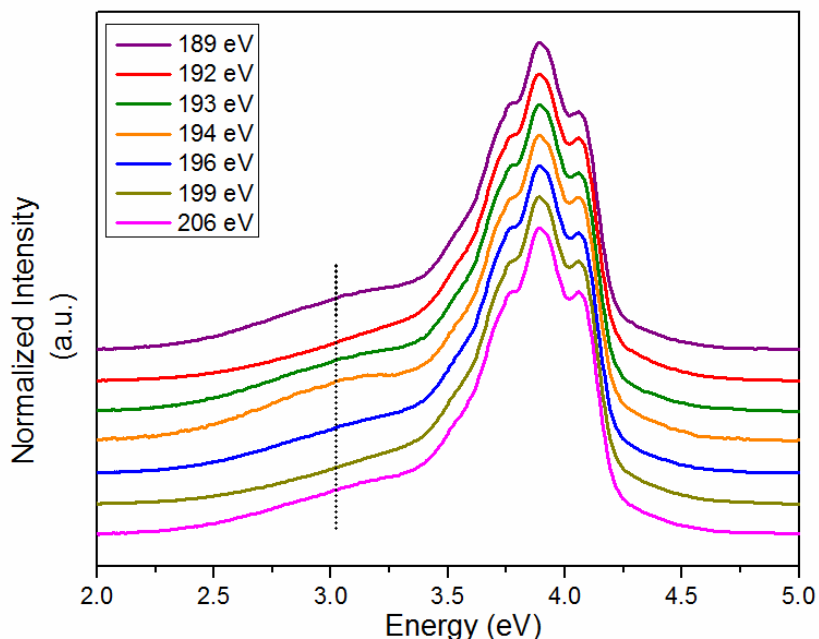


Figure 6-8 XEOL after intensity normalized to the 3.89 eV emission and shifted vertically for clarity.

Interestingly, apart from the variation of total luminescence intensity upon changing the X-ray excitation energy, the two emission bands also behave differently. Shown in Figure 6-8, the XEOL spectra are normalized to the 3.89 eV peak, and we can see that the 3.08

eV peak shows higher intensity below the edge (189 eV), at the B-O absorption peak energy (194 eV) and far beyond the edge (206 eV), while lowest intensity is observed at excitation energy of the B-N absorption peak (192 eV). This indicates in nat-BNNT, the near-UV and visible violet luminescence have different origins. In the following, wavelength-selected PLY spectra were obtained at N K-edge and O K-edge.

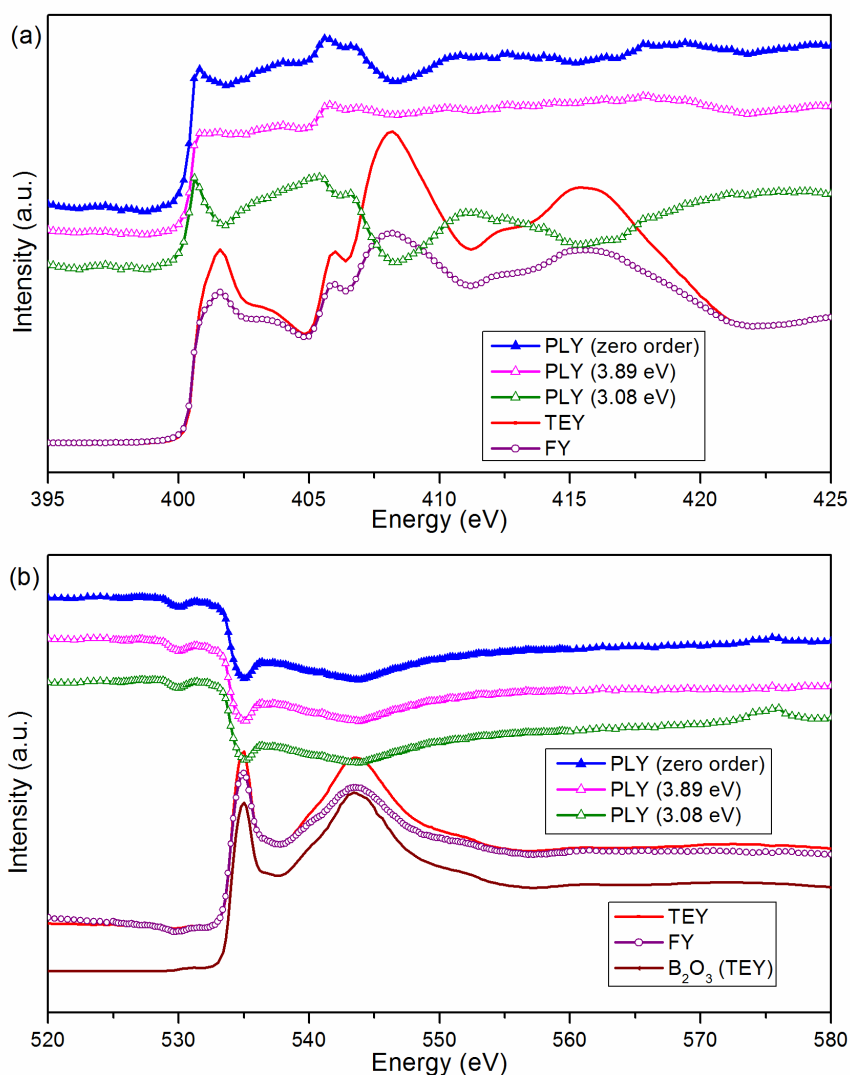


Figure 6-9 PLY-XANES of nat-BNNT at the (a) N K-edge and (b) O K-edge. The O K-edge TEY of B₂O₃ is shown as a reference.

Wavelength selected PLY at the N K-edge is shown in Figure 6-9 (a), with optical windows set to monitor the main 3.89 eV emission and the 3.08 eV shoulder emission. We clearly see that the main 3.89 eV luminescence shows little intensity variation above the edge. As for the 3.08 eV luminescence, although the intensity is weak compared to the 3.89 eV emission band, it displays all the same features as the ones in the absorption spectra with partial inversion. The changing of absorption coefficient of N does not affect the 3.98 eV near-UV emission but modulates the 3.08 eV emission significantly, hence N site contributes mainly to the luminescence of the latter.

On the other hand, the O K-edge XANES shown in Figure 6-9 (b) display well-defined features that resemble the O K-edge XANES of B_2O_3 , albeit inverted. This further confirms the presence of oxide in nat-BNNT, and the local environment of O in the nanotubes is similar to the one in B_2O_3 . The PLY across the O K-edge shows a strong dependence on the variation of the absorption coefficient regardless of the emission window selected, thus both luminescence bands have a significant oxide contribution. All PLY spectra are completely inverted, which is mainly due to a reduced quantum yield caused by O absorption at the O K-edge (as compared to B absorption at the B K-edge) as well as a saturation effect (penetration depth of soft X-ray is ~250 nm above the O K-edge [32]).

Compared to hex-BN, the optical behavior of nat-BNNT differs considerably, especially at the near-UV (3.98 eV) region. The luminescence intensity is highly sensitive to the absorption at the B K- and O K-edges, as shown in Figure 6-7 (b) and 6-9 (b), respectively. However, little change is seen at the N K-edge, at which the luminescence intensity exhibits a positive edge jump followed by a nearly constant response (Figure 6-

9(a)). The inverted PLY spectra of the B and O K-edges indicate that the emission is quenched once the boron oxide channels open up. It should be noted here, that no luminescence is detected from B_2O_3 powders alone upon X-ray excitation. In other words, the decay of B 1s electron in a B-O environment is non-radiative. In the case of O-contained BNNT, oxide species can be considered as dopant in the B-N network, for example, substituting a N atom forming a B-O moiety with a structure similar as B-N (i.e. B-O boroxol ring) [27]. The extra valence electron in O introduces a new impurity level in B-N system that could recombine with holes in the valence band to produce an optical emission via energy transfer. Hence, the increase of absorption coefficient upon B 1s electron excitation leads to an increase in optical yield at the B K-edge in the B-N environment. However, once the B sites in the B-O environment are preferentially excited at the B K-edge, the preferred decay is not via an optical channel. Therefore, a significant decrease in luminescence intensity is observed. The energy could be transferred to the B-N system that yields an increase in the 3.08 eV emission. The 4.05 eV shoulder emission should thus be attributed to the emission from the B-O impurity level. The 3.89 eV is caused by energy dissipation due to lattice stretching in the BNNT, as the interval between this peak and the 4.05 eV peak (0.16 eV, equivalent of 1289 cm^{-1}) close to the frequency of the B-N stretching mode ($\sim 1400\text{ cm}^{-1}$). Other weak shoulders at energy between 3.89 eV and 3.3 eV can be assigned to higher order phonon replicas.

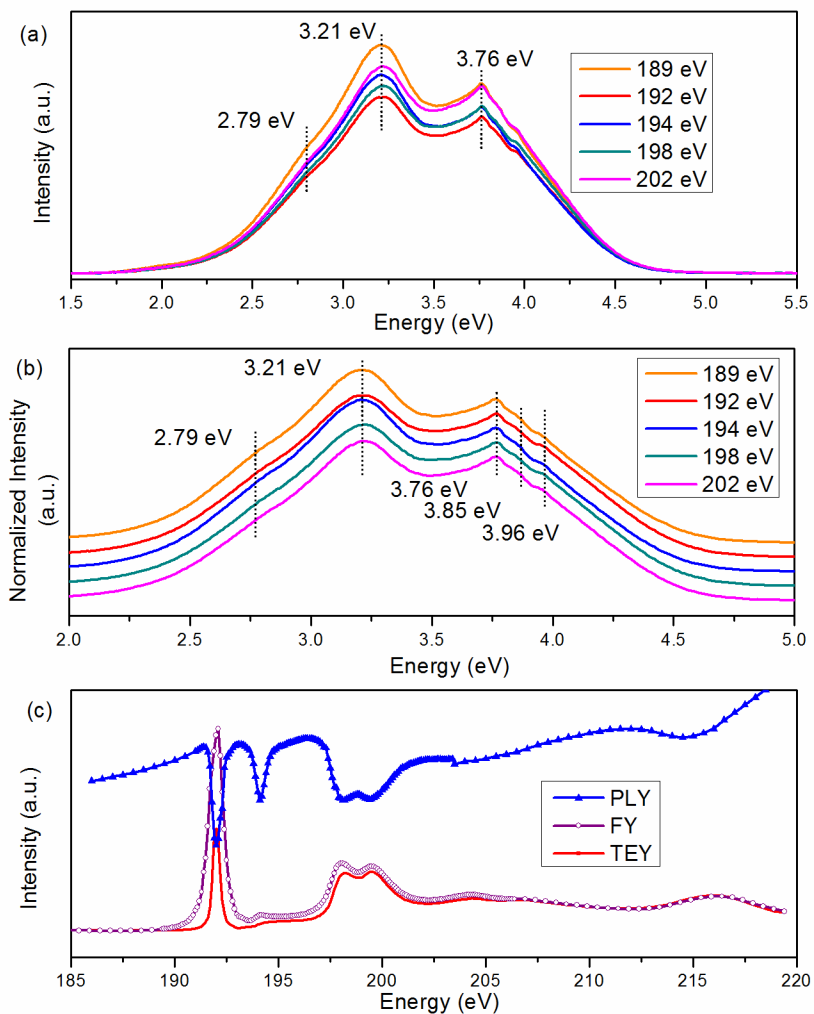


Figure 6-10 (a) XEOL of 10-BNNT with selected excitation energies across the B K-edge. (b) Enlarged view of XEOL at the 2.0 eV-5.0 eV region after normalization to the 3.76 eV peak. (c) B K-edge PLY of 10-BNNT in comparison with TEY and FY-XANES.

The XEOL of 10-BNNT is shown in Figure 6-10(a). The luminescence consists of two peaks: one violet emission at 3.21 eV (386 nm) and one near-UV emission at 3.76 eV (330 nm). The energy positions of the emission peaks are actually quite similar to what

has been observed from hex-BN (Figure 6-5(a)), with all peaks being narrower. The 3.76 eV emission is accompanied with two small oscillations at 3.85 eV and 3.96 eV, which can be seen more clearly from the enlarged view in Figure 6-10(b). This is also similar to the features in hex-BN. Meanwhile, luminescence of 10-BNNT also exhibits unique features: (1) the 3.76 eV emission is the most intense peak of the three, whereas in hex-BN, the 3.98 eV one is the strongest emission; (2) the 3.21 eV emission is the dominant emission in 10-BNNT, but in hex-BN, emission at this region is only seen as a shoulder; (3) the 3.76 eV and 3.21 eV emission bands behave differently while tuning the excitation energy. Shown in Figure 6-10(b), in which the spectra are normalized to the intensity of the 3.76 eV emission peak, the relative peak intensity varies as the excitation energies selected from below to above the B K-edge. The 3.21 eV emission weakens under excitation energy at B-N absorption maximum (192 eV), but becomes more intense at B-O absorption maximum (194 eV), showing a similar trend as what is observed from nat-BNNT (Figure 6-7). Interestingly, as can be seen in Figure 6-10 (c), the PLY of 10-BNNT at B K-edge not only has the resonances from B-N, but also shows an additional peak at 194 eV, although no such feature shows up in either TEY or FY of 10-BNNT.

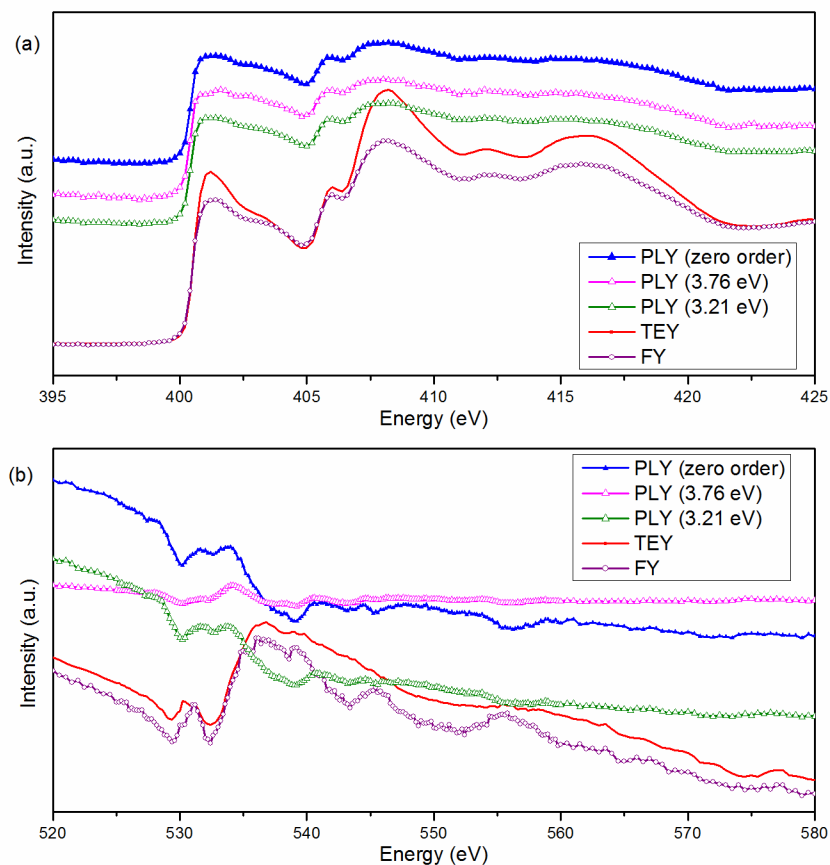


Figure 6-11 PLY-XANES of 10-BNNT at (a) the N K-edge and (b) the O K-edge.

The wavelength selected PLY-XANES of 10-BNNT at the N K- and O K-edge are shown in Figure 6-11. The zero order PLY at the N K-edge displays features similar to the absorption spectra. The PLY spectra of the 3.76 eV emission band and the 3.21 eV band are nearly identical to each other, thus both emission bands are N-related. On the other hand, the O K-edge XANES show poor and noisy features, which are due to the low oxide concentration in the sample, but we can still see weak oscillations, especially from the TEY. The zero-order PLY and the 3.21 eV PLY exhibit weak responses across the edge, but the PLY of the 3.76 eV emission is almost flat. Thus the presence of trace amount of surface oxide affects the luminescence, particularly the 3.21 eV emission

band. The oxide in the case of 10-BNNT is less likely as the dopant, but rather just surface impurities, because the 4.05 eV and the 3.89 eV emission bands are not observed. On the basis of these observations, the species could be a small BO^- molecule adsorbed on the surface, which facilitates the energy transfer from B-O to B-N, enhancing the 3.21 eV emission once the B-O channel opens up. Tang *et al.* also reported that, the adsorption of O on the BN surface after thermal oxidation could lead to the increase of the 3.2 eV emission [33].

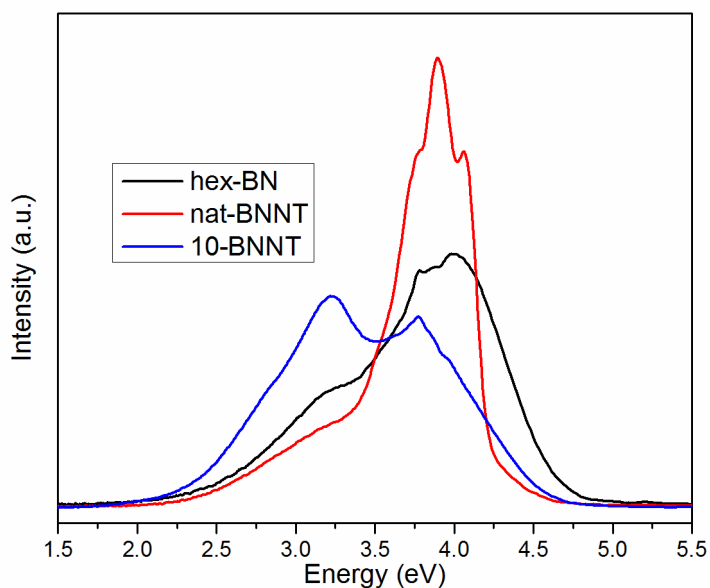


Figure 6-12 XEOL of hex-BN, nat-BNNT and 10-BNNT at excitation energy of 210 eV.

It is apparent from the above results that there are noticeable differences in both electronic structures and luminescence properties of nat-BNNT and 10-BNNT, especially in the B environment. The differences observed are caused by the amount of oxide impurities, rather than the effect of isotope substitution. As we can see from the XANES

spectra, both BNNT samples show hexagonal B-N local structures that are the same as bulk BN crystallites. The most interesting observation is that the presence of the oxide would significantly alter the luminescence properties of BN. Figure 6-12 compares the XEOL spectra of all three BN samples with excitation energy at 210 eV, which is above the B K-edge, and the peak shapes and the relative intensities vary considerably among the three samples. It should also be noted that, according to previously reported luminescence studies of BN using PL or CL, the band gap emission from hex-BN is commonly seen at 5-5.5 eV region, but we did not see it in our case. It could either be due to the fact that it is the unfavorable decay channel upon X-ray excitation of core electrons or be due to an effective energy transfer pathway to the defect emission. The visible violet emission (~ 3.2 eV) is present in all BN samples regardless of size and oxide impurities, and the peak width is relatively broad. The near-UV emission (~ 4 eV), however, varies in shape upon formation of different defect levels, and this also indicates that emission at this region has more than one origin, which is strongly dependent on the electronic structures.

6.4 Conclusion

In this chapter, the correlation between electronic structures and luminescence properties of BNNT and bulk hex-BN are examined. The role of oxygen impurities on the luminescence of BN is revealed by PLY-XANES and XEOL measurements. The results clearly demonstrate the site-sensitivity of XEOL in the case which different sites exhibit a large difference in the efficiency of the optical yield. Although BNNT shares similar electronic structure as its hexagonal bulk counterpart, it exhibits unique optical

properties, and the presence of oxide impurities alters the emission spectra significantly.

Several interesting findings are summarized below:

- (1) Bulk hex-BN has a broad luminescence at 4 eV and a shoulder at 3.2 eV. Both emission bands are attributed to the bulk defect emission of different defect levels, and the 4 eV emission is also accompanied by phonon replica.
- (2) Nat-BNNT contains oxide impurities. The O atoms act as dopant in BNNT, which introduce a new defect level, resulting in an intense 3.89 eV emission. The 3.0 eV emission is from the defect similar to the one in bulk BN, but the presence of oxide increases the intensity at this region via energy transfer once the oxide channel turns on.
- (3) 10-BNNT is relatively free of oxide. The 3.76 eV emission is mainly from the intrinsic BN defect with a trace contribution from the surface oxide component. Oxide impurities are mainly due to surface adsorption, which is responsible for the relative increase of the 3.2 eV emission due to energy transfer.

6.5 References

- [1] Rubio, A.; Corkill, J. L.; Cohen, M. L., *Phys. Rev. B* **1994**, *49*, 5081-4.
- [2] Chopra, N. G.; Luyken, R. J.; Cherrey, K.; Crespi, V. H.; Cohen, M. L.; Louie, S. G.; Zettl, A., *Science* **1995**, *269*, 966-7.
- [3] Golberg, D.; Bando, Y.; Tang, C.; Zhi, C. Y., *Adv. Mater.* **2007**, *19*, 2413-2432.

- [4] Terrones, M.; Romo-Herrera, J. M.; Cruz-Silva, E.; Lopez-Urias, F.; Munoz-Sandoval, E.; Velazquez-Salazar, J. J.; Terrones, H.; Bando, Y.; Golberg, D., *Mater. Today* **2007**, *10*, 30-38.
- [5] Golberg, D.; Bando, Y.; Huang, Y.; Terao, T.; Mitome, M.; Tang, C.; Zhi, C. Y., *ACS Nano* **2010**, *4*, 2979-2993.
- [6] Blase, X.; Rubio, A.; Louie, S. G.; Cohen, M. L., *Europhys. Lett.* **1994**, *28*, 335-340.
- [7] Watanabe, K.; Taniguchi, T.; Kanda, H., *Nature Mater.* **2004**, *3*, 404-409.
- [8] Taylor, C. A., II; Brown, S. W.; Subramaniam, V.; Kidner, S.; Rand, S. C.; Clarke, R., *Appl. Phys. Lett.* **1994**, *65*, 1251-1253.
- [9] Silly, M. G.; Jaffrennou, P.; Barjon, J.; Lauret, J. S.; Ducastelle, F.; Loiseau, A.; Obraztsova, E.; Attal-Tretout, B.; Rosencher, E., *Phys. Rev. B* **2007**, *75*, 085205.
- [10] Jaffrennou, P.; Barjon, J.; Schmid, T.; Museur, L.; Kanaev, A.; Lauret, J.-S.; Zhi, C. Y.; Tang, C.; Bando, Y.; Golberg, D.; Attal-Tretout, B.; Ducastelle, F.; Loiseau, A., *Phys. Rev. B* **2008**, *77*, 235422.
- [11] Museur, L.; Kanaev, A., *J. Appl. Phys.* **2008**, *103*, 103520.
- [12] Jaffrennou, P.; Barjon, J.; Lauret, J.-S.; Maguer, A.; Golberg, D.; Attal-Tretout, B.; Ducastelle, F.; Loiseau, A., *phys. Stat. solidi (b)* **2007**, *244*, 4147-4151.
- [13] Museur, L.; Feldbach, E.; Kanaev, A., *Phys. Rev. B* **2008**, *78*, 155204.
- [14] Berzina, B.; Trinkler, L.; Krutohvostov, R.; Williams, R. T.; Carroll, D. L.; Czerw, R.; Shishonok, E., *Phys. Stat. Solidi C* **2005**, *2*, 318-321.
- [15] Han, W.-Q.; Yu, H.-G.; Zhi, C.; Wang, J.; Liu, Z.; Sekiguchi, T.; Bando, Y., *Nano Lett.* **2008**, *8*, 491-494.

- [16] Tang, C.; Bando, Y.; Sato, T.; Kurashima, K., *Chem. Commun.* **2002**, 12, 1290-1291.
- [17] Zhi, C.; Bando, Y.; Tan, C.; Golberg, D., *Solid State Commun.* **2005**, 135, 67-70.
- [18] Hu, Y. F.; Zuin, L.; Wright, G.; Igarashi, R.; McKibben, M.; Wilson, T.; Chen, S. Y.; Johnson, T.; Maxwell, D.; Yates, B. W.; Sham, T. K.; Reininger, R., *Rev. Sci. Instrum.* **2007**, 78, 083109.
- [19] Regier, T.; Krochak, J.; Sham, T. K.; Hu, Y. F.; Thompson, J.; Blyth, R. I. R., *Nucl. Instrum. Methods Phys. Res. Sec. A* **2007**, 582, 93-95.
- [20] Zhou, X.; Sham, T.-K.; Zhang, W.; Chan, C.-Y.; Bello, I.; Lee, S.-T.; Hofsaess, H., *Anal. Chem.* **2006**, 78, 6314-6319.
- [21] Mozzi, R. L.; Warren, B. E., *J. Appl. Cryst.* **1970**, 3, 251-257.
- [22] Terauchi, M.; Tanaka, M.; Matsumoto, T.; Saito, Y., *J. Elec. Microscop.* **1998**, 47, 319-324.
- [23] Kuzuo, R.; Terauchi, M.; Tanaka, M., *Jpn. J. Appl. Phys.* **1992**, 31, L1484-L1487.
- [24] MacNaughton, J. B.; Moewes, A.; Wilks, R. G.; Zhou, X. T.; Sham, T. K.; Taniguchi, T.; Watanabe, K.; Chan, C. Y.; Zhang, W. J.; Bello, I.; Lee, S. T.; Hofsaess, H., *Phys. Rev. B* **2005**, 72, 195113.
- [25] Hemraj-Benny, T.; Banerjee, S.; Sambasivan, S.; Fischer, D. A.; Han, W.; Misewich, J. A.; Wong, S. S., *Phys. Chem. Chem Phys.* **2005**, 7, 1103-1106.
- [26] Choi, H. C.; Bae, S. Y.; Jang, W. S.; Park, J.; Song, H. J.; Shin, H.-J., *J. Phys. Chem. B* **2005**, 109, 7007-7011.
- [27] Gou, G.; Pan, B.; Shi, L., *J. Am. Chem. Soc.* **2009**, 131, 4839-4845.
- [28] Reshchikov, M. A.; Morkoc, H., *J. Appl. Phys.* **2005**, 97, 061301.

- [29] Wu, J.; Han, W.-Q.; Walukiewicz, W.; Ager, J. W., III; Shan, W.; Haller, E. E.; Zettl, A., *Nano Lett.* **2004**, *4*, 647-650.
- [30] Zhi, C.; Bando, Y.; Tang, C.; Golberg, D.; Xie, R.; Sekiguchi, T., *Appl. Phys. Lett.* **2005**, *86*, 213110.
- [31] Dong, Z.; Song, Y., *J. Phys. Chem. C* **2010**, *114*, 1782-1788.
- [32] X-ray Calculator. http://henke.lbl.gov/optical_constants
- [33] Tang, C.; Bando, Y.; Zhi, C. Y.; Golberg, D., *Chem. Commun.* **2007**, *44*, 4599-4601.

Chapter 7

7 Summary and Future Work

7.1 Conclusions

Electronic and optical properties of 1D nanomaterials are strongly affected by their morphologies, compositions and surface-bulk interaction. XANES and XEOL are powerful tools to study local electronic structures and optical luminescence with element and chemical site specificity. The thesis has been focusing on studying electronic structure and optical properties of three types of 1D nanomaterials: Si, SiC and BN.

Metal assisted electroless chemical etching is able to produce large-scale silicon nanowire (SiNW) arrays with controlled diameter, length, and surface structure. Chapter 3 presented the study of the electronic structure of Si nanowires upon Pt and Au nanoparticle deposition. The charge redistribution between metal nanoparticles and the Si substrate, and electronic structure of Pt-Au alloy were investigated. XANES was measured at the metal $L_{3,2}$ -edge and the Si K-edge, and XPS was measured at metal $4f$ and Si $2p$ binding energy level. When PtNP and AuNP are deposited separately onto Si, Pt donates its electrons to Si, resulting in a slight reduction of Si surface oxide, while no significant charge redistribution is observed between AuNP and Si. Pt-Au alloy nanoparticles are formed when PtNP and AuNP are co-deposited on SiNW. The alloy formation results in an expansion of Pt lattice and contraction of Au lattice. Charge redistribution occurs between Pt, Au and Si, during which Au loses d charge to Pt, and Pt donates its f charge to Si.

Chapter 4 focused on the luminescence properties from nanostructured Si and its thermal oxide. SiNW with smooth and porous surfaces, porous Si, and heavily oxidized SiNW were studied using XANES and XEOL at the Si $L_{3,2}$ -, K- and O K-edge. It was found that oxidized nano Si emits bright luminescence at multiple wavelengths due to the formation of a complicated Si-SiO_x ($0 < x \leq 2$) interface. The blue luminescence at 460 nm is attributed to Si in an oxygen-deficient environment, such as a defect center in SiO₂ and Si suboxide at the Si-SiO₂ interface. Luminescence at orange-red region (623 nm and 645 nm) is attributed to Si in an oxygen-rich SiO₂ environment.

In Chapter 5, crystalline SiC of 6H- and 3C-polytypes, SiC-SiO₂ core-shell nanowires and SiC nanowires were comparatively studied. Although the crystal structures are different, both 6H- and 3C-SiC exhibit similar XANES structure due to the same tetrahedral local structure. Using density functional theory calculations, XANES calculated using WIEN2k well-reproduces experimental results at the Si K-edge and the C K-edge. The as-prepared SiC nanowire sample has a SiC-SiO₂ core-shell structure. The core and shell contributions can be resolved by comparing the XANES spectrum obtained using the TEY and FY modes, due to their different sampling depths. All SiC crystalline samples are found light-emitting at ~2.0 eV, which is attributed to SiC bulk defects.

Nanosized 6H-SiC has an additional luminescence band at 1.98 eV due to the formation of a thin layer of native oxide. Higher amount of surface oxide is seen in 3C-SiC nanocrystals, resulting in a 2.75 eV emission band. The oxide emission (2.70 eV) is also observed in the core-shell SiC nanowires. The presence of a thick oxide shell around SiC nanowire also results in an additional emission band at a 3.30 eV. Quantum confined luminescence is observed from SiC nanowires, shown as an emission band at 2.44 eV.

Chapter 6 presented a study on the electronic structures and luminescence properties of BN nanotubes and hexagonal BN crystals using XANES and XEOL. Bulk BN crystals emit near-UV luminescence originated from two defect levels: a main emission band at ~ 4.0 eV accompanied by photon replicas, and a less intense 3.2 eV emission. As for BN nanotube samples, it was found the presence of oxygen in the BN system plays an important role in luminescence properties of BNNT. The use of B isotope has negligible effect on the local structure of BN. For BN nanotubes containing oxide, new defect center is formed, resulting in an intense emission at 3.89 eV.

7.2 Future Work

At nanoscale, the electronic structure and luminescence properties of a material can be considerably different from its bulk form. Various synthesis routes produce nanostructures of unique morphologies with complex surface structures and rich defect centers. It has been shown in this thesis that using XEOL in combination with XANES, the observed luminescence can be correlated with the electronic structure of the material with element and chemical site specificity. It is especially useful for studying core-shell, nano-composite and doped nanomaterials.

Nanostructured Si and its oxide have been studied for many years. However, the luminescence mechanism of nano Si is still worth investigating due to the complicated interface formed between Si and SiO₂. On one hand, the bare Si surface is almost always covered with a thin native oxide layer. On the other hand, oxide can also be produced during the synthesis process. It was found that thermally formed oxides and chemically formed oxides, amorphous and crystalline SiO₂ are different in structures which lead to their different luminescence properties. Another example is mesoporous silica, which is

an interesting Si nanostructure system due to its potential application in drug delivery systems, is found light emitting which shares some similar luminescence features as seen in thermally oxidized porous Si [1]. It would be very desirable if a solid connection can be established between the observed luminescence and the electronic structure of nanostructured Si.

The investigation of luminescence properties of SiO₂ can be further linked to SiC, since the native oxide of SiC is SiO₂. Chapter 5 has shown studies on SiC nanowires with and without the SiO₂ shell, and the difference in luminescence spectra between the two samples was seen. In the XEOL study, the core and shell contribution to the total luminescence were analyzed using Gaussian peak fitting. The origin of each luminescence component can be done in a more accurate manner by using another synchrotron spectroscopy technique called “scanning transmission X-ray microscopy” (STXM). This is a technique which combines XANES and microscopy with a spatial resolution of ~30 nm, so that chemical mapping and electronic structure can be obtained from an individual nanowire [2,3]. The contribution from SiC and SiO₂ to the total luminescence can thus be distinguished by monitoring XEOL while focusing the beam at the core region and the shell region, respectively.

As for BN nanostructures, more work can be done on studying the oxygen doping effect on the electronic structure and luminescence of BN. Aside from BN nanotubes, graphene-like BN nanosheets have also been synthesized [4]. The synthesis of BN nanostructures usually involves the use of C or oxides, so the resulted BN product could be mixed with C or O. It is desirable to find out whether the C and O atoms are doped into BN network or remains as impurities in a mixed final product, and how they affect the luminescence

of pure BN. Experimentally, this can be done by comparing the synthesized BN nanostructures with a series of reference compounds. Meanwhile, as for theory support, band structure calculation is also desirable to carry out [5], which can be done by building different structural models in order to find out how the dopant interacts with the BN network.

7.3 References

- [1] Guo, X. and Sham, T. K., unpublished
- [2] Felten, A.; Bittencourt, C.; Pireaus, J. J.; Reichelt, M.; Mayer, J.; Hernandez-Cruz, D.; Hitchcock, A. P., *Nano Lett.* 2007, 7, 2435-2440.
- [3] Zhou, J.; Wang, J.; Liu, H.; Banis, N. M.; Sun, X.; Sham, T. K., *J. Phys. Chem. Lett.* 2010, 1, 1709-1713.
- [4] Han, W. Q.; Yu, H.-G.; Liu, Z., *Appl. Phys. Lett.* 2011, 98, 203112.
- [5] Gou, G.; Pan, B.; Shi, L., *J. Am. Chem. Soc.* 2009, 131, 4839-4845.

Appendix A.

Appendix A. Silver-assisted Electroless Chemical Etching of SiNW: Synthesis and Etching Mechanism

A.1 Introduction

Chemical etching of Si has been widely used in industry for silicon wafer cleaning and micromachining. In general, etching is anisotropic in basic solution such as KOH [1,2] and isotropic in acid, typically HF-oxidant mixed solutions [3,4]. The latter has been more commonly used to produce patterned Si nanostructures on Si wafers, which is also known as the “top-down” nanofabrication technique. The surface reactivity of Si upon interaction with various etching solutions has been investigated. It has been known that the Si surface can be partially etched upon bringing it into contact with etching solution containing HF in combination with a strong oxidizing agent such as KMnO_4 , CrO_3 and HNO_3 [4-6]. Alternatively, porous Si can be produced by immersing a Si wafer in an HF-contained aqueous or organic solution while applying an external current [7,8]. The significance of porous Si is that it is a mixed structure of quantum confined Si, amorphous SiO_2 , crystalline SiO_2 , and such complicated structure was found exhibiting orange-red luminescence under X-ray or UV excitation [9-11]. Later, Peng *et al* found that a layer of silver (Ag) nanoparticles could act as catalyst during Si etching, and they developed a unique method of synthesizing uniform Si nanowire (SiNW) arrays from Si wafers by means of Ag-assisted electroless chemical etching [12,13]. The general idea is that, by immersing the Si wafer in a mixed solution of H_2O_2 and HF, Ag nanoparticles on the Si surface could catalyze and direct the etching reaction in a localized region. The Si surface without Ag coverage remains, forming nanowire array structure.

Compared to the “bottom-up” SiNW synthesis techniques such as chemical vapor deposition (CVD), electroless chemical etched SiNW has a relatively larger average diameter, but the lengths of SiNW can be easily controlled by modifying the etching conditions. More importantly, doped SiNW can be synthesized by choosing the Si wafer of desired dopant type and concentration, as opposed to CVD-prepared SiNW where uniform doping is very difficult to achieve. In addition, chemically etched SiNW has a uniform morphology and is directly attached to the Si substrate, making it a good candidate for electronic device fabrication as well as an ideal substrate for growing secondary nanostructures.

The first systematic experiment on the effect of experimental conditions on the morphology of SiNW was carried out by Zhang *et al* [13] Si wafers of different orientation and dopant concentrations were used and the affecting factors such as etching solution concentrations and etching temperatures on the morphology of SiNW were investigated. Recent studies have shown that following a similar synthesis strategy, SiNW of porous surface can be fabricated using a heavily doped Si wafer or by etching under high temperature [14-16]. Maintaining the similar array structure as regular SiNW, porous SiNW are also found to be light emitting under UV excitation.

In this appendix, the preparation of the SiNW specimens used in the studies reported in Chapters 3 and 4 is described. SiNW were synthesized using the Ag-assisted, electroless chemical etching method. Regular SiNW (i.e. SiNW with smooth surface) were synthesized using lightly doped Si wafers. Apart from studying the effect of experimental factors on the morphology of SiNW, focus is also put on examining the length of the SiNW as a function of etching duration and etchant concentration. In addition, porous

SiNW were synthesized by etching heavily doped Si wafers. The etching mechanism of Si in related to the SiNW formation is discussed.

A.2 Experimental

SiNWs were prepared by etching Si wafers following the silver-assisted electroless chemical etching strategy [13]. Si wafers of (100) orientation were investigated. The effects of etchant solution concentration and etching duration were studied on n-type phosphorous-doped Si wafers, and the dopant concentration effect were studied using a p-type boron-doped Si wafer. The detailed physical properties are shown in Table A-1. The experiments described in the following were carried out under room temperature and ambient condition.

The silicon wafer was first cut into 3cm x 1cm squares and rinsed with acetone, ethanol, deionized water, and a mixture of concentrated H_2SO_4 and 30% H_2O_2 with a volume ratio of 3:1 to remove surface organic impurities. Then the wafer was dipped into a 5% (wt.) HF aqueous solution for 3 minutes to form hydrogen terminated Si surface. A thin layer of Ag nanoparticles was deposited onto the Si wafer by dipping it into a solution containing AgNO_3 and HF for 1 minute. The etching was carried out by immersing the Si wafer in the mixture of H_2O_2 and HF for the desired duration. The concentration of AgNO_3 was varied between 0.0015 M and 0.001 M, and the concentration of H_2O_2 was varied between 0.3 M and 0.5 M. The HF concentration was kept constant as 4.8 M. After etching, the Si wafer was removed from the etching solution and the Ag nanoparticles were dissolved using diluted HNO_3 . Then the SiNWs were rinsed using 5% HF and deionized water and dried in air.

The morphologies of as-prepared and metal deposited SiNWs were characterized using scanning electron microscopy (SEM, LEO1540) and transmission electron microscopy (TEM, Philips CM10).

Table A-1 Physical parameters of Si wafers used in the experiment.

Type	Orientation	Dopant	Resistivity ($\Omega\cdot\text{cm}$)	Thickness (μm)
N	100	Phosphorus	1-5	500-550
P	100	Boron	3-10	500-550
P	100	Boron	0.005-0.0025	500-550

A.3 Results and Discussion

Figure A-1 shows the typical morphology of the as-prepared SiNW. N-type and p-type SiNW that were prepared using lightly doped Si wafers. The concentrations of etchant solutions used were 0.005 M for AgNO_3 and 0.4 M for H_2O_2 , and etching duration was 30 minutes. It can be seen from the top view SEM images that for both types of Si wafers, large scale SiNW arrays are formed on the Si substrate. The tips of the nanowires form bundles which are due to capillary force during drying. From the side view, we can see that the nanowires are perpendicular to the substrate, indicating that etching is along the (001) direction. The length of the nanowires is about 25 μm . Detailed morphology of a single wire is shown in the TEM image Figure A-1 (c) and (f). The nanowires have a smooth surface and the diameter is about 80 nm. Since both n-type and p-type Si wafers

produce SiNW of similar morphologies, in the following, the effecting factors were examined on n-type SiNW.

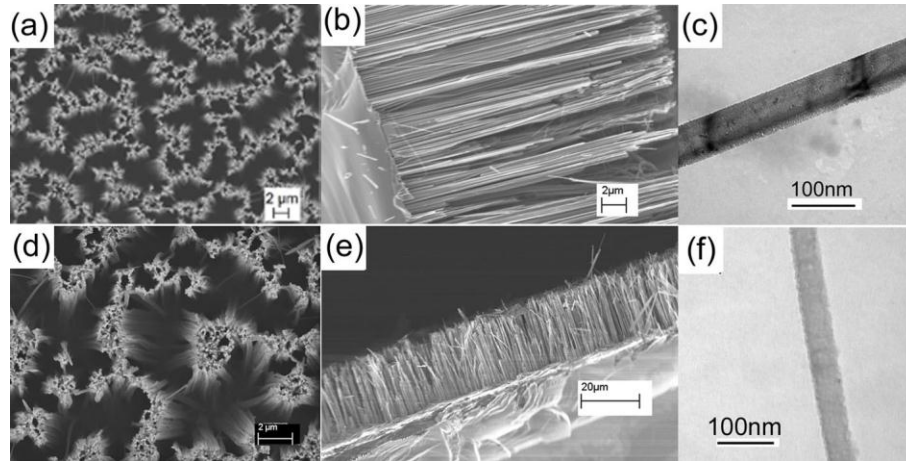


Figure A-1 Morphology of SiNW. Top row: n-type SiNW, bottom row: p-type SiNW. (a) and (d): SEM images in top view, (b) and (e): SEM images in side view, (c) and (f): TEM images of a single wire.

A.3.1 Effecting Factor 1: Etchant Concentration

Figure A-2 shows the effect of AgNO_3 concentration on the morphologies of n-type SiNW. During the etching process, AgNO_3 solution was used to provide Ag^+ ions which are reductively deposited on the Si surface. The concentrations of AgNO_3 used to produce SiNW shown in Figure A-2 are 0.0015 M, 0.005 M, 0.01 M and 0.02 M, respectively. The concentrations of HF (4.8 M) and H_2O_2 (0.4 M) were kept as constant. It can be seen from the top view of SiNW that lower concentration of AgNO_3 produces SiNW of smaller diameter. As the concentration increases, the gaps between the nanowires increases, in other words, a larger portion of Si wafer was etched away. The length of the SiNW is revealed by the side view SEM images. SiNW made using 0.0015

M AgNO₃ (Figure A-2(b)) are of 17.1 μm in length. The length of the SiNW increases to 24.6 μm using the 0.005 M AgNO₃ (Figure A-2(d)). However, using more concentrated AgNO₃ did not increase the growth rate (etching rate) of SiNW (Si wafer). As seen in Figure A-2(f) and (h), the SiNW prepared using 0.01 M and 0.02 M AgNO₃ are of length similar to each other (~26 μm) and are only slightly longer than the one prepared using 0.005 M AgNO₃.

The H₂O₂ concentration factor was also examined. SiNW were prepared using H₂O₂ of three different concentrations: 0.3 M, 0.4 M and 0.5M. The concentrations of AgNO₃ and HF were kept constant as 0.005 M and 4.8 M, respectively. Shown in Figure A-3, the top views of three as-prepared SiNW differ slightly, that higher H₂O₂ concentration leads to an increased disorder. However, the length of the nanowires is strongly affected by the H₂O₂ concentration. As can be seen from the side view SEM images in Figure 5-3, 0.3 M H₂O₂ produces SiNW of ~20 μm in length, while 0.5 M H₂O₂ produces SiNW of 28.5 μm long.

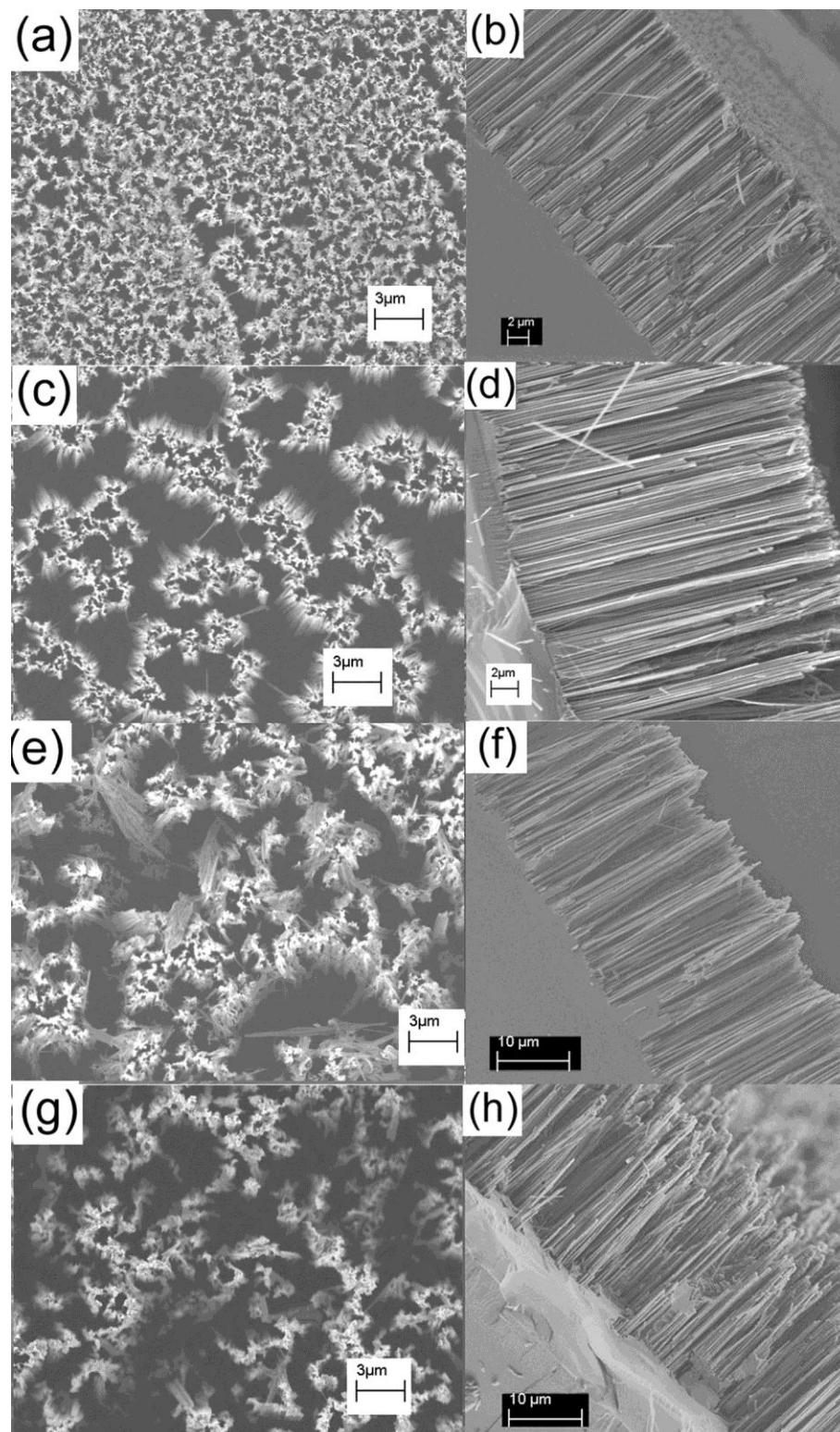


Figure A-2 SEM images of SiNWs made from varied AgNO_3 concentrations. (a) and (b) 0.0015 M, (c) and (d) 0.005 M, (e) and (f) 0.01 M, (g) and (h) 0.02 M.

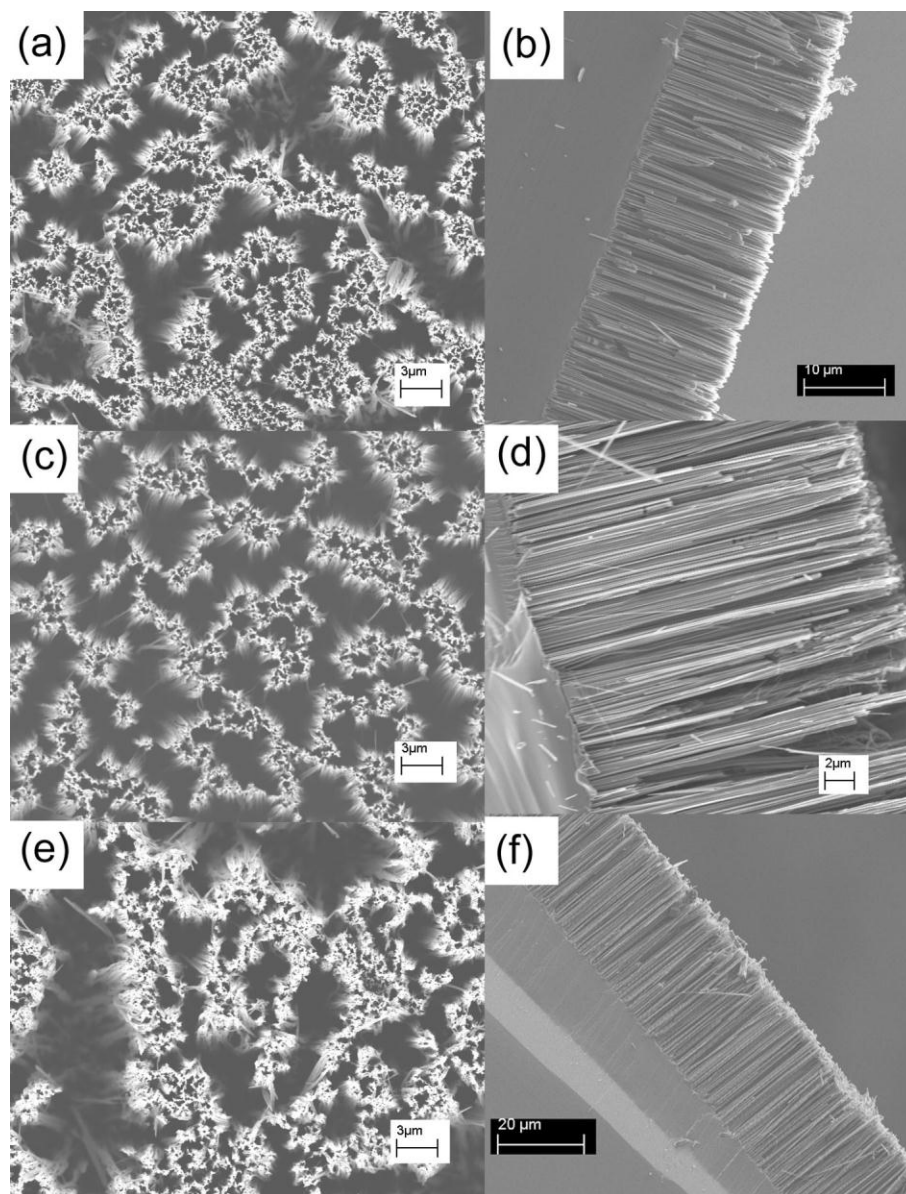


Figure A-3 SEM images of SiNW made from varied H_2O_2 concentrations. (a) and (b) 0.3 M, (c) and (d) 0.4 M, (e) and (f) 0.5 M.

The length of the SiNW as a function of etchant concentration is summarized in Figure A-4. It can be seen that changing the concentration of AgNO_3 has only limited effect on the length of SiNW. As shown in Figure A-4(a), under the same etching duration, the length of SiNW increases by using 0.005M AgNO_3 instead of the 0.0015 M one.

However, further increase the AgNO_3 concentration does not produce longer SiNW. In addition, the higher concentration of AgNO_3 results in SiNW of a highly disordered structure. The concentration of H_2O_2 , on the other hand, plays an important role on controlling the length of the SiNW. As can be seen in Figure A-4(b), the length of SiNW exhibits a linear relationship with the concentration of H_2O_2 .

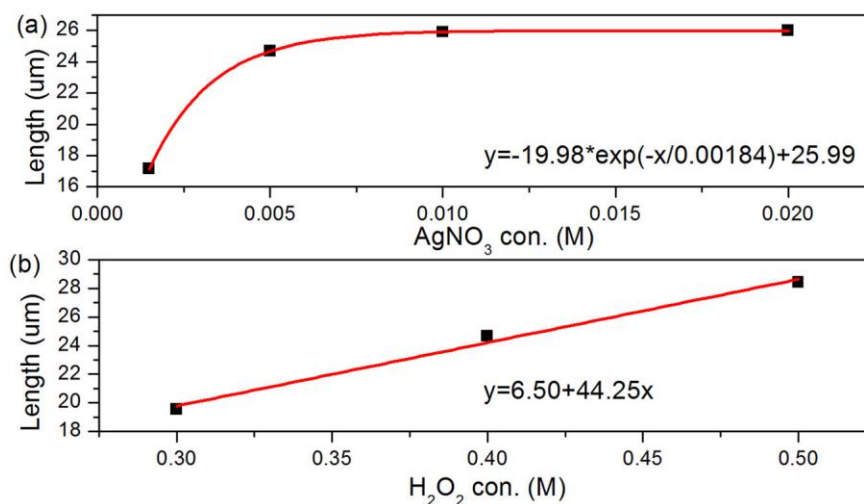


Figure A-4 The length of SiNW as a function of (a) AgNO_3 concentration and (b) H_2O_2 concentration.

A.3.2 Effecting Factor 2: Etching Duration

Another effecting factor examined is the etching duration. The time-dependent experiment was carried out using 0.005M AgNO_3 , 4.8 M HF and 0.4 M H_2O_2 , and etching duration varies from 1 min to 120 min. Figure A-5 shows selected SEM images of SiNW after etching for 1 min, 5 min and 120 min. It can be seen the formation of SiNW is highly efficient: after immersing in the etching solution for 1 min, porous structures are formed on the Si surface. The porous structures rapidly turn to nanowire structures after 5 min. After 120 min etching, SiNW still remains as an ordered array

structure. The tips of the wires form bundles due to capillary force and lack of mechanical support, but individual nanowires are clearly seen. It is also surprising that the growth of SiNW exhibit an excellent linear relationship with the etching time. As can be seen in Figure A-5(d), the SiNW length was recorded from 5 min of etching till 120 min of etching. The length of the nanowires is linearly proportional to the etching duration. The linear fit results indicates that the growth rate of the SiNW is $0.64 \mu\text{m}/\text{min}$.

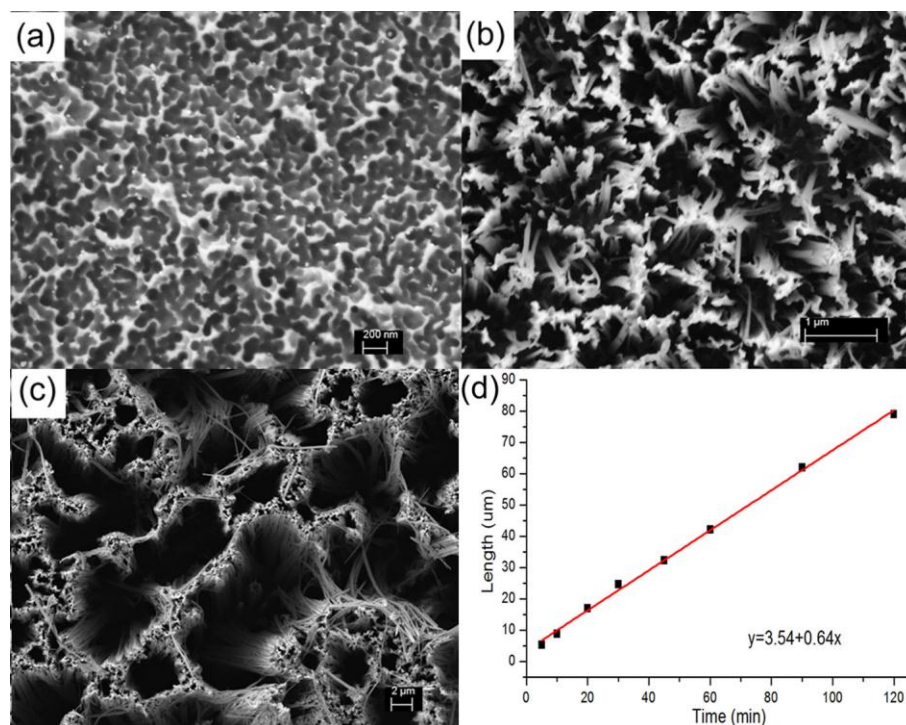


Figure A-5 SEM images in top view of SiNW etched for (a) 1 min, (b) 5 min and (c) 120 min; and (d) plot of the length of SiNW as a function of etching time.

A.3.3 Effecting Factor 3: Doping Level

Etching was also performed on the heavily doped Si wafer. Under the same etching condition for making lightly doped SiNW (i.e. 0.005 M AgNO_3 and $0.4 \text{ M H}_2\text{O}_2$ for 30 min etching), nanowires arrays are formed perpendicular to the Si substrate. The

morphology of heavily doped SiNW is shown in Figure A-6. Comparing to SiNW made using lightly doped Si (Figure A-1), heavily doped SiNW is much shorter in length, which is $\sim 16\mu\text{m}$. Interestingly, unlike the smooth surface of lightly doped SiNW, heavily doped SiNW exhibit a much higher surface roughness, which in fact, are porous SiNW.

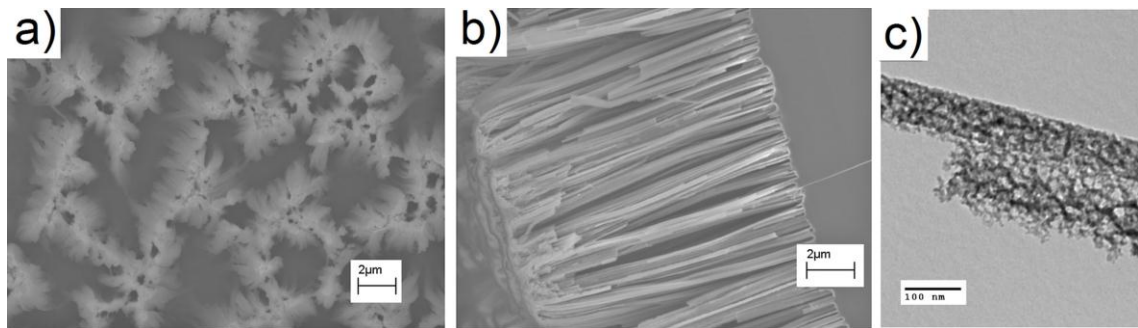


Figure A-6 Morphology of SiNW by etching of heavily doped Si wafer. (a) SEM image in top view, (b) SEM image in side view, and (c) TEM image of single wires.

A.3.4 Etching Mechanism

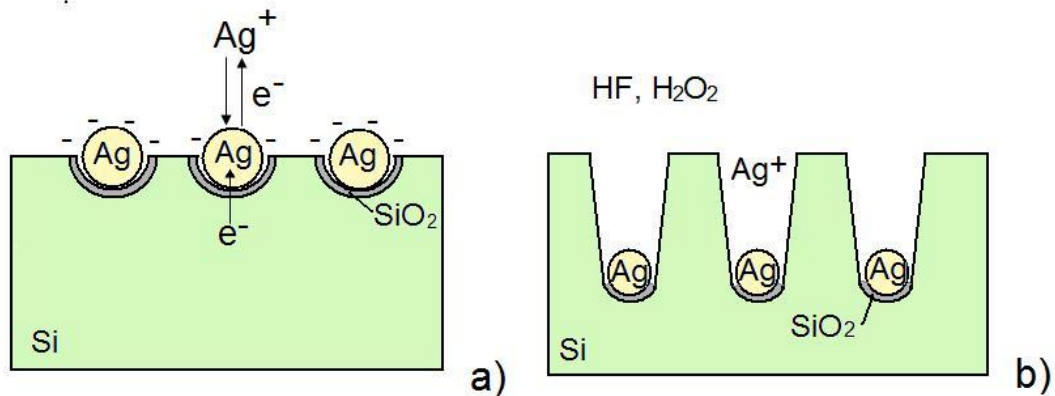
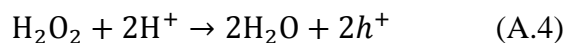
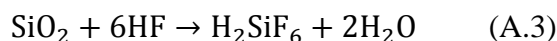
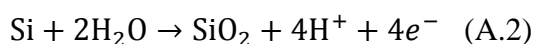
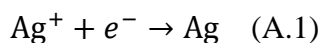


Figure A-7 Schematic diagram of the SiNW formation. (a) Ag deposition, (b) electroless Ag-assisted etching

The synthesis of SiNW involves two steps: Ag deposition and Ag-assisted chemical etching, which are described schematically in Figure A-7. The reaction mechanism of Si and its oxide in F⁻-contained solution has been extensively studied [13,17-19]. In the case of metal assisted etching, the reactions involved during the synthesis can be described using Reactions A.1-A.5 listed below [13,18,19].



In the first step, H-terminated silicon acts as a reducing agent which converts Ag⁺ from solution to metallic Ag (Reaction A.1), and the Si surface thus forms a thin layer of oxide (Reaction A.2) The oxide is readily etched away by HF (Reaction A.3). Metallic Ag first appears as nanoparticles covering the Si surface and then quickly grows into a nano-dendrite structure by nucleation [20]. Figure A-8 shows the SEM images of the Si surface after Ag deposition. It can be seen Ag produced after the reduction reaction has three types of morphologies: (1) ultra-fine particles of less than 10 nm in diameters forms a thin layer covering Si surface, (2) Ag particles of larger size (~200 nm) formed on top of the first layer, (3) a micron-scaled dendrite structure on the top.

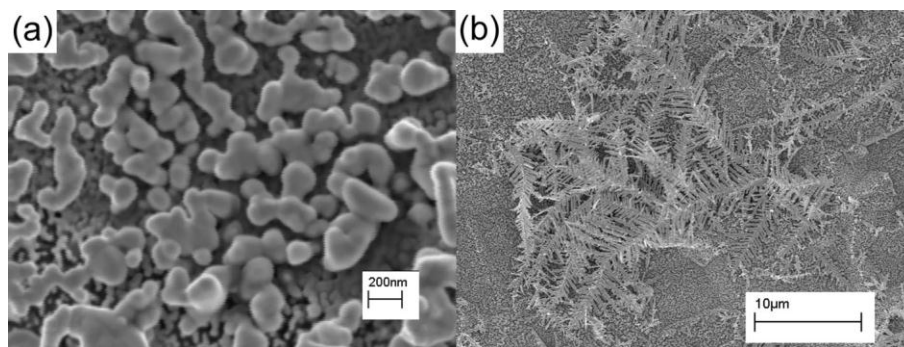


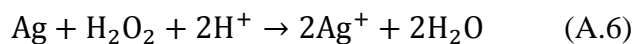
Figure A-8 SEM images of Si wafer after Ag deposition (a) Ag nanoparticles, (b) Ag dendrite

In the next step, etching is carried out by the reactions between Si, HF and H₂O₂. Unlike the electrochemical anodization during which an external power source (current or voltage) provides the driving force, in the electroless chemical etching, the reaction is initiated by H₂O₂, which acts as an oxidizing agent allowing hole (h^+) injection into Si (Reaction A.4). Si then reacts with HF and is etched away (Reaction A.5). The reduction of H₂O₂ is catalyzed by Ag particles, thus etching takes place in the region localized to where Ag particles are deposited. Initially pores are formed on the Si wafer surface. As etching proceeds, the Ag particles sink in the Si wafer, and Si nanowires form at the gap between the Ag particles where Si is not etched away by HF.

The distribution of Ag nanoparticles plays an important role on forming a uniform array of SiNW, since etching reaction occurs preferably where the particles are located. The bigger the Ag particles are formed, the lower density of nanowires is produced. This explains that a low concentration of AgNO₃ produces denser SiNW array, since the chance of Ag nanoparticle aggregation are small. However, Ag nanoparticles themselves are not directly involved in the etching reaction, so etching rate is not affected by the

further increase of the AgNO_3 concentration. Meanwhile, high AgNO_3 concentration results in the formation of Ag dendrite structures, which results in a poor organization of SiNW arrays as revealed by SEM images in Figure A-2.

On the other hand, altering the concentration of H_2O_2 plays an important part on controlling the length of the SiNW. The length of SiNW versus H_2O_2 concentration plot (Figure A-4(b)) shows a linear relationship, which supports the suggested reaction mechanism (Reactions A.4 and A.5). From the SEM images in Figure A-3 (a) and (c), we can see that increasing the concentration of H_2O_2 from 0.3 M to 0.4 M does not alter the diameters of the SiNW, only the length of SiNW increases after using H_2O_2 of higher concentration. However, when comparing the morphology of SiNW using 0.5 M H_2O_2 (Figure A-3(e)) with the other two, we can see that the surface of SiNW exhibits a disordered structure. A possible side reaction should be considered in which Ag is oxidized to Ag^+ upon reacting with H_2O_2 in the acid environment (Reaction A.6):



The Ag dendrite on the surface can be partially dissolved, but at the same time, the Ag^+ are reduced back to Ag particles and can be attached to the Si surface, leading to a secondary etching at the nanowire tips and side walls.

The secondary etching is actually more favorable when using a heavily doped Si wafer. Since heavily doped Si has a higher carrier concentration, Ag^+ gains electrons from Si more easily. At the same time, the dopants act as defect sites for Ag particles nucleation from the etchant resulting in smaller and denser Ag nanoparticles attaching to the side wall of SiNW. Hence heavily doped SiNW with porous surface are produced. The

decrease in the etchant concentration at the bottom and the reduced size of Ag particles lead to SiNW of shorter length and larger diameter.

For lightly doped Si, the growth rate of SiNW shows a linear relationship with etching time under fixed etching concentration. This is of particular interesting, since once Ag particles penetrates deeper in Si wafer, there is likely a concentration gradient generated from the wafer surface and the bottom of the holes. However, the observed linear relationship between nanowire length and etching duration suggests that the concentration gradient is not present or has little effect on the etching rate. After 120 min etching, nanowires are of 80 μm long can be produced without losing their overall structure as nanowire arrays. This could be due to an active ion exchange in the etchant solution, where H_2O_2 is constantly supplied by the environment, hence maintaining its local concentration around Ag nanoparticles.

A.4 Conclusion

SiNW were synthesized by silver-assisted electroless chemical etching method. The morphology of SiNW can be controlled by altering the concentration of AgNO_3 , H_2O_2 , dopant concentration in Si wafer, and etching time. The length of SiNW is linearly proportional to the concentration of H_2O_2 and the etching duration. However, high concentration of H_2O_2 leads to an increased disorder. Lower concentration of AgNO_3 produces denser SiNW of shorter length. Since AgNO_3 only provide Ag catalysts during etching, further increase of AgNO_3 concentration does not affect the etching rate. SiNW of smooth surfaces can be produced using lightly doped Si wafer, while etching heavily doped Si wafer results in SiNW of a porous surface.

A.5 References

- [1] Seidel, H.; Csepregi, L.; Heuberger, A.; Baumgartel, H., *J. Electrochem. Soc.* **1990**, *137*, 3612-3626.
- [2] Sato, K.; Shikida, M.; Matsushima, Y.; Yamahsiro, T.; Asaumi, K.; Iriye, Y.; Yamamoto, M., *Sens. Actuators A* **1998**, *61*, 87-93.
- [3] Sato, N.; Sakaguchi, K.; Yamagata, k.; Fujiyama, Y.; Yonehara, T., *J. Electrochem. Soc.* **1995**, *142*, 3116-3122.
- [4] Kooij, E. S.; Butter, K.; Kelly, J. J., *Electrochem. Solid State Lett.* **1999**, *2*, 178-180.
- [5] Hadjersi, T.; Gabouze, N.; Kooij, E. S.; Zinine, A.; Ababou, A.; Chergui, W.; Cheraga, H.; Belhousse, S.; Djeghri, A., *Thin Solid Films* **2004**, *459*, 271-275.
- [6] van den Meerakker, J. E. A. M.; van Vegchel, J. H. C., *J. Electrochem. Soc.* **1989**, *136*, 1949-1953.
- [7] Zhang, X. G.; Collins, S. D.; Smith, R. L., *J. Electrochem. Soc.* **1989**, *136*, 1561-1565.
- [8] Searson, P. C.; Macaulay, J. M.; Prokes, S. M., *J. Electrochem. Soc.* **1992**, *139*, 3373-3377.
- [9] Canham, L. T., *Appl. Phys. Lett.* **1990**, *57*, 1046-1048.
- [10] Cullis, A. G.; Canham, L. T.; Calcott, P. D. J., *J. Appl. Phys.* **1997**, *82*, 909.
- [11] Sham, T. K.; Jiang, D. T.; Coulthard, I.; Lorimer, J. W.; Feng, X. H.; Tan, K. H.; Frigo, S. P.; Rosenberg, R. A.; Houghton, D. C.; Bryskiewicz, B., *Nature* **1993**, *363*, 331-334.
- [12] Peng, K.; Yan, Y.; Gao, S.; Zhu, J., *Adv. Mater.* **2002**, *14*, 1164-1167.
- [13] Zhang, M.-L.; Peng, K.-Q.; Fan, X.; Jie, J.-S.; Zhang, R.-Q.; Lee, S.-T.; Wong,

- N.-B., *J. Phys. Chem. C* **2008**, *112*, 4444-4450.
- [14] Qu, Y.; Liao, L.; Li, Y.; Zhang, H.; Huang, Y.; Duan, X., *Nano Lett.* **2009**, *9*, 4539-4543.
- [15] Qu, Y.; Zhou, H.; Duan, X., *Nanoscale* **2011**, *3*, 4060-4068.
- [16] Hochbaum, A. I.; Gargas, D.; Hwang, Y. J.; Yang, P., *Nano Lett.* **2009**, *9*, 3550-3554.
- [17] Zhang, X. G., *Electrochemistry of Silicon and Its Oxide*. Kluwer Academic/Plenum Publishers: New York, 2001
- [18] Kolasinski, K. W., *Phys. Chem. Chem. Phys.* **2003**, *5*, 1270-1278.
- [19] Chartier, C.; Bastide, S.; Levy-Clement, C., *Electrochimica Acta* **2008**, *53*, 5509-5516.
- [20] Peng, K.; Fang, H.; Hu, J.; Wu, Y.; Zhu, J.; Yan, Y.; Lee, S. T., *Chem. Eur. J.* **2006**, *12*, 7942-7947.

Appendix B Copyright release from John Wiley and Sons

JOHN WILEY AND SONS LICENSE TERMS AND CONDITIONS

May 17, 2012

This is a License Agreement between Lijia Liu ("You") and John Wiley and Sons ("John Wiley and Sons") provided by Copyright Clearance Center ("CCC"). The license consists of your order details, the terms and conditions provided by John Wiley and Sons, and the payment terms and conditions.

All payments must be made in full to CCC. For payment instructions, please see information listed at the bottom of this form.

License Number	2905331308283
License date	May 10, 2012
Licensed content publisher	John Wiley and Sons
Licensed content publication	Small
Licensed content title	The Effect of Thermal Oxidation on the Luminescence Properties of Nanostructured Silicon
Licensed content author	Lijia Liu, Tsun-Kong Sham
Licensed content date	May 2, 2012
Start page	n/a
End Page	n/a
Type of use	Dissertation/Thesis
Requestor type	Author of this Wiley article
Format	Print and electronic
Portion	Full article
Will you be translating?	No
Order reference number	
Total	0.00 USD

TERMS AND CONDITIONS

This copyrighted material is owned by or exclusively licensed to John Wiley & Sons, Inc. or one of its group companies (each a "Wiley Company") or a society for whom a Wiley Company has exclusive publishing rights in relation to a particular journal (collectively WILEY). By clicking "accept" in connection with completing this licensing transaction, you agree that the following terms and conditions apply to this transaction (along with the billing and payment terms and conditions established by the Copyright Clearance Center Inc., ("CCC's Billing and Payment terms and conditions"), at the time that you opened your Rightslink account (these are available at any time at <http://myaccount.copyright.com>)

Terms and Conditions

1. The materials you have requested permission to reproduce (the "Materials") are protected by copyright.
2. You are hereby granted a personal, non-exclusive, non-sublicensable, non-transferable, worldwide, limited license to reproduce the Materials for the purpose specified in the licensing process. This license is for a one-time use only with a maximum distribution equal to the number that you identified in the licensing process. Any form of republication granted by this licence must be completed within two years of the date of the grant of this licence (although copies prepared before may be distributed thereafter). The Materials shall not be used in any other manner or for any other purpose. Permission is granted subject to an appropriate acknowledgement given to the author, title of the material/book/journal and the publisher. You shall also duplicate the copyright notice that appears in the Wiley publication in your use of the Material. Permission is also granted on the understanding that nowhere in the text is a previously published source acknowledged for all or part of this Material. Any third party material is expressly excluded from this permission.
3. With respect to the Materials, all rights are reserved. Except as expressly granted by the terms of the license, no part of the Materials may be copied, modified, adapted (except for minor reformatting required by the new Publication), translated, reproduced, transferred or distributed, in any form or by any means, and no derivative works may be made based on the Materials without the prior permission of the respective copyright owner. You may not alter, remove or suppress in any manner any copyright, trademark or other notices displayed by the Materials. You may not license, rent, sell, loan, lease, pledge, offer as security, transfer or assign the Materials, or any of the rights granted to you hereunder to any other person.
4. The Materials and all of the intellectual property rights therein shall at all times remain the exclusive property of John Wiley & Sons Inc or one of its related companies (WILEY) or their respective licensors, and your interest therein is only that of having possession of and the right to reproduce the Materials pursuant to Section 2 herein during the continuance of this Agreement. You agree that you own no right, title or interest in or to the Materials or any of the intellectual property rights therein. You shall have no rights hereunder other than the license as provided for above in Section 2. No right, license or

interest to any trademark, trade name, service mark or other branding ("Marks") of WILEY or its licensors is granted hereunder, and you agree that you shall not assert any such right, license or interest with respect thereto.

5. NEITHER WILEY NOR ITS LICENSORS MAKES ANY WARRANTY OR REPRESENTATION OF ANY KIND TO YOU OR ANY THIRD PARTY, EXPRESS, IMPLIED OR STATUTORY, WITH RESPECT TO THE MATERIALS OR THE ACCURACY OF ANY INFORMATION CONTAINED IN THE MATERIALS, INCLUDING, WITHOUT LIMITATION, ANY IMPLIED WARRANTY OF MERCHANTABILITY, ACCURACY, SATISFACTORY QUALITY, FITNESS FOR A PARTICULAR PURPOSE, USABILITY, INTEGRATION OR NON-INFRINGEMENT AND ALL SUCH WARRANTIES ARE HEREBY EXCLUDED BY WILEY AND ITS LICENSORS AND WAIVED BY YOU.

6. WILEY shall have the right to terminate this Agreement immediately upon breach of this Agreement by you.

7. You shall indemnify, defend and hold harmless WILEY, its Licensors and their respective directors, officers, agents and employees, from and against any actual or threatened claims, demands, causes of action or proceedings arising from any breach of this Agreement by you.

8. IN NO EVENT SHALL WILEY OR ITS LICENSORS BE LIABLE TO YOU OR ANY OTHER PARTY OR ANY OTHER PERSON OR ENTITY FOR ANY SPECIAL, CONSEQUENTIAL, INCIDENTAL, INDIRECT, EXEMPLARY OR PUNITIVE DAMAGES, HOWEVER CAUSED, ARISING OUT OF OR IN CONNECTION WITH THE DOWNLOADING, PROVISIONING, VIEWING OR USE OF THE MATERIALS REGARDLESS OF THE FORM OF ACTION, WHETHER FOR BREACH OF CONTRACT, BREACH OF WARRANTY, TORT, NEGLIGENCE, INFRINGEMENT OR OTHERWISE (INCLUDING, WITHOUT LIMITATION, DAMAGES BASED ON LOSS OF PROFITS, DATA, FILES, USE, BUSINESS OPPORTUNITY OR CLAIMS OF THIRD PARTIES), AND WHETHER OR NOT THE PARTY HAS BEEN ADVISED OF THE POSSIBILITY OF SUCH DAMAGES. THIS LIMITATION SHALL APPLY NOTWITHSTANDING ANY FAILURE OF ESSENTIAL PURPOSE OF ANY LIMITED REMEDY PROVIDED HEREIN.

9. Should any provision of this Agreement be held by a court of competent jurisdiction to be illegal, invalid, or unenforceable, that provision shall be deemed amended to achieve as nearly as possible the same economic effect as the original provision, and the legality, validity and enforceability of the remaining provisions of this Agreement shall not be affected or impaired thereby.

10. The failure of either party to enforce any term or condition of this Agreement shall not constitute a waiver of either party's right to enforce each and every term and condition of this Agreement. No breach under this agreement shall be deemed waived or excused by either party unless such waiver or consent is in writing signed by the party

granting such waiver or consent. The waiver by or consent of a party to a breach of any provision of this Agreement shall not operate or be construed as a waiver of or consent to any other or subsequent breach by such other party.

11. This Agreement may not be assigned (including by operation of law or otherwise) by you without WILEY's prior written consent.

12. Any fee required for this permission shall be non-refundable after thirty (30) days from receipt.

13. These terms and conditions together with CCC's Billing and Payment terms and conditions (which are incorporated herein) form the entire agreement between you and WILEY concerning this licensing transaction and (in the absence of fraud) supersedes all prior agreements and representations of the parties, oral or written. This Agreement may not be amended except in writing signed by both parties. This Agreement shall be binding upon and inure to the benefit of the parties' successors, legal representatives, and authorized assigns.

14. In the event of any conflict between your obligations established by these terms and conditions and those established by CCC's Billing and Payment terms and conditions, these terms and conditions shall prevail.

15. WILEY expressly reserves all rights not specifically granted in the combination of (i) the license details provided by you and accepted in the course of this licensing transaction, (ii) these terms and conditions and (iii) CCC's Billing and Payment terms and conditions.

16. This Agreement will be void if the Type of Use, Format, Circulation, or Requestor Type was misrepresented during the licensing process.

17. This Agreement shall be governed by and construed in accordance with the laws of the State of New York, USA, without regards to such state's conflict of law rules. Any legal action, suit or proceeding arising out of or relating to these Terms and Conditions or the breach thereof shall be instituted in a court of competent jurisdiction in New York County in the State of New York in the United States of America and each party hereby consents and submits to the personal jurisdiction of such court, waives any objection to venue in such court and consents to service of process by registered or certified mail, return receipt requested, at the last known address of such party.

Wiley Open Access Terms and Conditions

All research articles published in Wiley Open Access journals are fully open access: immediately freely available to read, download and share. Articles are published under the terms of the [Creative Commons Attribution Non Commercial License](#), which permits use, distribution and reproduction in any medium, provided the original work is properly cited and is not used for commercial purposes. The license is subject to the Wiley Open Access terms and conditions:

Wiley Open Access articles are protected by copyright and are posted to repositories and websites in accordance with the terms of the [Creative Commons Attribution Non Commercial License](#). At the time of deposit, Wiley Open Access articles include all changes made during peer review, copyediting, and publishing. Repositories and websites that host the article are responsible for incorporating any publisher-supplied amendments or retractions issued subsequently.

Wiley Open Access articles are also available without charge on Wiley's publishing platform, **Wiley Online Library** or any successor sites.

Use by non-commercial users

For non-commercial and non-promotional purposes individual users may access, download, copy, display and redistribute to colleagues Wiley Open Access articles, as well as adapt, translate, text- and data-mine the content subject to the following conditions:

- The authors' moral rights are not compromised. These rights include the right of "paternity" (also known as "attribution" - the right for the author to be identified as such) and "integrity" (the right for the author not to have the work altered in such a way that the author's reputation or integrity may be impugned).
- Where content in the article is identified as belonging to a third party, it is the obligation of the user to ensure that any reuse complies with the copyright policies of the owner of that content.
- If article content is copied, downloaded or otherwise reused for non-commercial research and education purposes, a link to the appropriate bibliographic citation (authors, journal, article title, volume, issue, page numbers, DOI and the link to the definitive published version on Wiley Online Library) should be maintained. Copyright notices and disclaimers must not be deleted.
- Any translations, for which a prior translation agreement with Wiley has not been agreed, must prominently display the statement: "This is an unofficial translation of an article that appeared in a Wiley publication. The publisher has not endorsed this translation."

Use by commercial "for-profit" organisations

Use of Wiley Open Access articles for commercial, promotional, or marketing purposes requires further explicit permission from Wiley and will be subject to a fee. Commercial purposes include:

- Copying or downloading of articles, or linking to such articles for further redistribution, sale or licensing;
- Copying, downloading or posting by a site or service that incorporates advertising with such content;

- The inclusion or incorporation of article content in other works or services (other than normal quotations with an appropriate citation) that is then available for sale or licensing, for a fee (for example, a compilation produced for marketing purposes, inclusion in a sales pack)
- Use of article content (other than normal quotations with appropriate citation) by for-profit organisations for promotional purposes
- Linking to article content in e-mails redistributed for promotional, marketing or educational purposes;
- Use for the purposes of monetary reward by means of sale, resale, licence, loan, transfer or other form of commercial exploitation such as marketing products
- Print reprints of Wiley Open Access articles can be purchased from:
corporatesales@wiley.com

Other Terms and Conditions:

BY CLICKING ON THE "I AGREE..." BOX, YOU ACKNOWLEDGE THAT YOU HAVE READ AND FULLY UNDERSTAND EACH OF THE SECTIONS OF AND PROVISIONS SET FORTH IN THIS AGREEMENT AND THAT YOU ARE IN AGREEMENT WITH AND ARE WILLING TO ACCEPT ALL OF YOUR OBLIGATIONS AS SET FORTH IN THIS AGREEMENT.

v1.7

If you would like to pay for this license now, please remit this license along with your payment made payable to "COPYRIGHT CLEARANCE CENTER" otherwise you will be invoiced within 48 hours of the license date. Payment should be in the form of a check or money order referencing your account number and this invoice number RLNK500776766.

Once you receive your invoice for this order, you may pay your invoice by credit card. Please follow instructions provided at that time.

**Make Payment To:
Copyright Clearance Center
Dept 001
P.O. Box 843006
Boston, MA 02284-3006**

For suggestions or comments regarding this order, contact RightsLink Customer Support: customercare@copyright.com or +1-877-622-5543 (toll free in the US) or +1-978-646-2777.

Gratis licenses (referencing \$0 in the Total field) are free. Please retain this printable license for your reference. No payment is required.

Appendix C Copyright release from ACS Publications



RightsLink®

Home

Account Info

Help



ACS Publications Title:
High quality. High impact.

Electronic Structures and Optical Properties of 6H- and 3C-SiC Microstructures and Nanostructures from X-ray Absorption Fine Structures, X-ray Excited Optical Luminescence, and Theoretical Studies

Logged in as:

Lijia Liu

Account #:

3000524645

LOGOUT

Author: Lijia Liu et al.

Publication: The Journal of Physical Chemistry C

Publisher: American Chemical Society

Date: Apr 1, 2010

Copyright © 2010, American Chemical Society

PERMISSION/LICENSE IS GRANTED FOR YOUR ORDER AT NO CHARGE

This type of permission/license, instead of the standard Terms & Conditions, is sent to you because no fee is being charged for your order. Please note the following:

- Permission is granted for your request in both print and electronic formats, and translations.
- If figures and/or tables were requested, they may be adapted or used in part.
- Please print this page for your records and send a copy of it to your publisher/graduate school.
- Appropriate credit for the requested material should be given as follows: "Reprinted (adapted) with permission from (COMPLETE REFERENCE CITATION). Copyright (YEAR) American Chemical Society." Insert appropriate information in place of the capitalized words.
- One-time permission is granted only for the use specified in your request. No additional uses are granted (such as derivative works or other editions). For any other uses, please submit a new request.

BACK

CLOSE WINDOW

Copyright © 2012 Copyright Clearance Center, Inc. All Rights Reserved. [Privacy statement](#).
Comments? We would like to hear from you. E-mail us at customecare@copyright.com

Appendix D Copyright release from ACS publications



RightsLink®

Home

Account
Info

Help



ACS Publications
High quality. High impact.

Title: X-ray Excited Optical
Luminescence from Hexagonal
Boron Nitride Nanotubes:
Electronic Structures and the
Role of Oxygen Impurities

Logged in as:

Lijia Liu

Account #:
3000524645

LOGOUT

Author: Lijia Liu et al.

Publication: ACS Nano

Publisher: American Chemical Society

Date: Jan 1, 2011

Copyright © 2011, American Chemical Society

PERMISSION/LICENSE IS GRANTED FOR YOUR ORDER AT NO CHARGE

This type of permission/license, instead of the standard Terms & Conditions, is sent to you because no fee is being charged for your order. Please note the following:

- Permission is granted for your request in both print and electronic formats, and translations.
- If figures and/or tables were requested, they may be adapted or used in part.
- Please print this page for your records and send a copy of it to your publisher/graduate school.
- Appropriate credit for the requested material should be given as follows: "Reprinted (adapted) with permission from (COMPLETE REFERENCE CITATION). Copyright (YEAR) American Chemical Society." Insert appropriate information in place of the capitalized words.
- One-time permission is granted only for the use specified in your request. No additional uses are granted (such as derivative works or other editions). For any other uses, please submit a new request.

BACK

CLOSE WINDOW

Copyright © 2012 Copyright Clearance Center, Inc. All Rights Reserved. [Privacy statement](#).
Comments? We would like to hear from you. E-mail us at customer@copyright.com

Curriculum Vitae

Name: Lijia Liu

Post-secondary Education and Degrees: The University of Western Ontario
London, Ontario, Canada
2007-present. Ph. D. Candidate

The University of Science and Technology of China
Hefei, Anhui, China
2003-2007 B. Sc. in Chemical Physics

Honours and Awards: Ontario Graduate Scholarship
2011-2012

Related Work Experience: Teaching Assistant and lab demonstrator
Chemistry, The University of Western Ontario
2007-2012

Publications:

1. **Lijia Liu** and Tsun-Kong Sham. The effect of thermal oxidation on the luminescence properties of nanostructured silicon. *Small*, **2012** in press.
2. **Lijia Liu**, Tsun-Kong Sham, Hisashi Hayashi, Noriko Kanai, Yuki Takehara, Naomi Kawamura, Masaichiro Mizumaki, and Robert A. Gordon. Resonant inelastic X-ray scattering of CeB₆ at the Ce L₁- and L₃-edges. *J. Chem. Phys.* **2012**, 136, 194501
3. Songlan Yang, Dongniu Wang, Guoxian Liang, Yun Mui Yiu, Jiajun Wang, **Lijia Liu**, Xueliang Sun, and Tsun-Kong Sham. Soft-X-ray XANES studies of various phases related to LiFePO₄ based cathode materials. *Energy Environ. Sci.*, **2012**, 5, 7007
4. **Lijia Liu**, Sun Kim, Jeffrey Chan and Tsun-Kong Sham. Morphology and electronic structures of calcium phosphate coated titanium dioxide nanotubes. *Mater. Res. Soc. Symp. Proc.*, **2011**, 1352, gg18-01
5. Jingyu Lv, J. Y. P. Ko, Ying Zhang, **Lijia Liu**, Xiujian Zhang, Xiaohong Zhang, Xuhui Sun and T. K. Sham. Electronic Structure and Optical properties of 2,5,8,11-tetra-butylperylene polyhedral crystals from X-ray absorption near-edge structure and X-ray excited optical luminescence studies. *Appl. Phys. Lett.* **2011**, 98 243106
6. Chihiro Yogi, Kazuo Kojima, Takeshi Hashishin, Noriyuki Wada, Yasuhiro

- Inada, Enrico D. Gaspera, Marco Bersani, Alessandro Martucci, **Lijia Liu** and Tsun-Kong Sham. Size effect of Au nanoparticles on TiO₂ crystalline phase of nanocomposite thin films and their photocatalytic properties. *J. Phys. Chem C*, **2011**, 115, 6554
7. **Lijia Liu**, Tsun-Kong Sham, Weiqiang Han, Chunyi Zhi and Yoshio Bando, X-ray excited optical luminescence from hexagonal boron nitride nanotubes: electronic structures and the role of oxygen impurities. *ACS Nano*, **2011**, 5, 631
 8. **Lijia Liu**, Yun-Mui Yiu, and Tsun-Kong Sham, Electronic structures of LaB₆ and CeB₆ single crystals: X-ray absorption spectroscopy at B K-edge and the La and Ce giant resonance. *J. Electron Spectrosc. Related Phenom.* **2011**, 184, 188
 9. **Lijia Liu**, Jeffrey Chan and Tsun-Kong Sham, Calcination-induced phase transformation and accompanying optical luminescence of TiO₂ nanotubes: an X-ray absorption near-edge structures and X-ray excited optical luminescence study. *J. Phys. Chem. C*, **2010**, 114, 21353
 10. Denis Gebauer, Philips N. Gunawidjaja, J. Y. Peter Ko, Zoltan Bacsik, Baroz Aziz, **Lijia Liu**, Yongfeng Hu, Lennart Bergstrom, Cheuk-Wai Tai, Tsun-Kong Sham, Mattias Eden and Niklas Hedin, Proto-Calcite and Proto-Vaterite in amorphous calcium carbonates, *Angew. Chem. Int. Ed.* **2010**, 49, 8889
 11. **Lijia Liu**, Y. M. Yiu, Tsun-Kong Sham, Liying Zhang and Yafei Zhang, Electronic structures and optical properties of 6H- and 3C-SiC microstructures and nanostructures from X-ray absorption fine structures, x-ray excited optical luminescence and theoretical studies. *J. Phys. Chem. C* **2010**, 114, 6966
 12. **Lijia Liu**, Y. M. Yiu, Tsun-Kong Sham, Dongfang Yang, and Lucia Zuin, Electronic structure of nanopolycrystalline pulsed laser deposited LaB₆ films and single crystals: the boron perspective. *J. Appl. Phys.* **2010**, 107, 043703
 13. **Lijia Liu**, J. Y. P. Ko, Matthew J. Ward, Y. M. Yiu, Tsun-Kong Sham, and Yafei Zhang, XANES and XEOL investigations of SiC microcystals and SiC nanowires. *J. Phys. Conference Series*, **2009**, 190, 012134
 14. **Lijia Liu**, Michael Murphy, J. Y. P. Ko, and Tsun-Kong Sham, XAFS Studies of Pt nanoparticles deposition on Si nanowires. *J. Phys. Conference Series*, **2009**, 190, 012133

Conference Presentations

1. **Lijia Liu**, TiO₂ nanotubes: Phase Transformation and Calcium Phosphate Deposition. Oral presentation at *Material Research Society (MRS) Spring Conference 2011: Titanium Dioxide Symposium*

2. **Lijia Liu**, Y. M. Yiu and T. K. Sham, X-ray Absorption Spectroscopic Studies of LaB₆ and CeB₆ Single Crystals on 4d-4f Transitions and B K-edges. Poster presented at the *37th International Conference on Vacuum Ultraviolet and X-ray Physics*, **2010** (VUVX 2010)
3. **Lijia Liu**, T. K. Sham and R. A. Gordon, Resonant Inelastic X-ray Scattering Studies of CeB₆ at the Ce L₃-edge, Poster presented at *New Science with Resonant Elastic and Inelastic X-ray Scattering, Satellite Meeting of VUVX 2010*
4. **Lijia Liu**, Effects of Temperature on Phase Transformation and Luminescence of TiO₂ Nanotubes: XANES and XEOL Studies, Invited talk at *Canadian Light Source 13th Annual Users' Meeting*, **2010**
5. **Lijia Liu**, Isotope Substitution and Oxidation Effect on the Electronic Structure and Optical Properties of Boron Nitride Nanotubes. Oral Presentation at the *93rd Canadian Chemistry Conference and Exhibition (CSC)*, **2010**
6. **Lijia Liu**, Y. M. Yiu, T. K. Sham and Y. Zhang, XANES and XEOL Investigation of SiC Microcrystals and SiC Nanowires, Poster presented at the *14th International Conference on X-ray Absorption Fine Structures (XAFS14)*, **2009**
7. **Lijia Liu**, M. Murphy, J. Y. P. Ko and T. K. Sham, XAFS Studies of Pt Nanoparticles Deposition of Si Nanowires, Poster presented at the *14th International Conference on X-ray Absorption Fine Structures (XAFS14)*, **2009**
8. **Lijia Liu**, J. Y. P. Ko, T. K. Sham and Y. F. Zhang, X-ray Spectroscopy Studies of One-dimensional Nanostructures: Si, SiC nanowires and Carbon Nanotubes. Poster presented at the *Canadian Light Source 11th Annual Users' Meeting*, **2008**